Faculty of Sciences

Institute of Astrophysics and Geophysics

Long-term study of methane and two of its derivatives from solar observations recorded at the Jungfraujoch station

A dissertation presented by Whitney Bader in fulfillment of the thesis requirement for the degree of Doctor of Philosophy in Sciences

2015

It's been a long day
without you my friend
and I'll tell you all about it
when I see you again.

À François.

Abstract

A long-term study of methane and two of its derivatives, i.e. ethane and methanol from ground-based FTIR solar observations recorded at the high alpine International Scientific Station of the Jungfraujoch (3580 m a.s.l.) is reported. Those three gases act as tropospheric ozone precursors through their removal pathway and therefore have an impact on air quality. In the stratosphere, methane influences the content of ozone and in the production of water vapor. Moreover, both methane and ethane impact the greenhouse radiative forcing. While the latter is an indirect greenhouse gas because of its sinks, the former is the second most important anthropogenic greenhouse gas after CO_2.

The primary challenge of this work is the development and optimization of retrieval strategies for the three studied gases from FTIR spectra recorded at the Jungfraujoch station, in the framework of the Network for Detection of Atmospheric Composition Change (NDACC), in order to assess their concentrations in the atmosphere and to study their long-term trend and recent changes as well as their seasonal variations. The development and optimization of a retrieval strategy, based on the selection of the best combination of parameters, aims to limit interferences, minimize residuals, and maximize information content. To this end, the best retrieval strategy has been selected from a great number of available combinations thanks to a method for error analysis developed through this work.

A 17-year time series of methanol is presented thanks to the combination of spectral windows for the first time for ground-based observations resulting in the improvement of the information content. We therefore present the first long-term time series of methanol total, lower tropospheric and upper tropospheric–lower stratospheric partial columns. We found no significant long-term trend of methanol but its seasonal cycle shows a high peak-to-peak amplitude of ~103 % for total columns characterized by minimum values in winter and maximum values during summertime. The presented time series provides a valuable tool for model and satellite validation and complement the few NDACC measurements at northern mid-latitudes.

Regarding ethane, we have for the first time included a combination of improved spectroscopic parameters as well as an improved a priori state that substantially reduce fitting residuals and enhance information content. Analysis of the long-term trend of ethane covering 20 years of observations revealed a strong positive trend of ethane from 2009 onwards of ~5 %/year. We hypothesize that this recent ethane upturn may be the result of a large increase in fugitive emissions from the massive exploitation of shale gas and tight oil reservoirs on the North American continent.

Finally, we quantified the changes of methane since 2005 from 10 ground-based NDACC sites, with a mean global increase of 0.30 %/year. Investigations into the source(s) responsible for this re-increase are performed with a GEOS-Chem tagged simulation that provides the contribution of each emission source and one sink to the total methane simulated. From the analysis of the GEOS-Chem tracers on both the local and global scales, we determined that the increasing anthropogenic emissions such as coal mining, gas and oil transport and exploitation, have played a major role in the increase of atmospheric methane observed since 2005 while they are secondary contributors to the total methane budget.

Résumé

Une étude à long terme du méthane et de deux de ses dérivés, à savoir l'éthane et le méthanol utilisant des observations solaires enregistrées à la station scientifique internationale du Jungfraujoch (3580 m d'altitude) est présentée. Ces trois gaz, précurseurs d'ozone troposphérique, ont un impact sur la qualité de l'air. Dans la stratosphère, le méthane influence le contenu en ozone et est source de vapeur d'eau. En outre, le méthane et l'éthane ont un impact sur le forçage radiatif global. En effet, alors que ce dernier est un gaz à effet de serre indirect en raison de ses puits, le méthane est le deuxième gaz à effet de serre anthropique le plus abondant après le CO_2.

Le principal objectif de ce travail est le développement et l'optimisation de la stratégie d'inversion des trois gaz étudiés à partir de spectres FTIR enregistrés au Jungfraujoch, dans le cadre du réseau NDACC (*Network for Detection of Atmospheric Composition Change*); et ce, afin d'évaluer leurs concentrations atmosphériques et d'étudier leurs tendances à long et court terme ainsi que leur variation saisonnière. Il s'agit de limiter les interférences, minimiser les résidus, et maximiser le contenu en information sur base de la meilleure combinaison de paramètres disponibles. La sélection de la meilleure stratégie d'inversion s'effectue notamment grâce à la méthode d'analyse d'erreur développée ici.

Une stratégie d'inversion du méthanol offrant une nette amélioration du contenu en information est obtenue grâce à la combinaison de deux fenêtres spectrales. Nous déduisons des séries temporelles longues de 17 ans de colonnes totales et partielles, pour la basse troposphère et haute troposphère-basse stratosphère. Alors que l'analyse des séries temporelles ne montre aucune tendance significative à long-terme, le cycle saisonnier des colonnes totales de méthanol caractérisé par des valeurs minimales en hiver et maximales en été, montre une forte amplitude de ~103%. Les séries temporelles produites fournissent un outil précieux pour la validation de modèles et satellites et complètent les mesures NDACC aux latitudes moyennes de l'hémisphère nord.

En ce qui concerne l'éthane, nous avons pour la première fois combiné de meilleurs paramètres spectroscopiques et amélioré l'état a priori, réduisant sensiblement les résidus et améliorant le contenu en information. L'analyse de tendances pour la période 1994-2014 a révélé une forte augmentation de l'éthane à partir de 2009 qui équivaut à ~5 %/an. Nous émettons l'hypothèse que cette récente reprise de l'éthane peut être le résultat d'une forte augmentation des émissions liées à l'exploitation massive de gaz de schiste et des réservoirs de pétrole sur le continent nord-américain.

Enfin, nous avons quantifié l'augmentation moyenne globale du méthane depuis 2005 à 0.30 %/an à partir d'observations au sol de 10 stations NDACC. Une simulation taguée du modèle GEOS-Chem qui fournit la contribution de chaque source d'émission (et un puit) au méthane total simulé nous permet d'investiguer la(les) source(s) responsable(s) de cette ré-augmentation. A partir d'une analyse locale et globale des traceurs GEOS-Chem, nous avons déterminé que l'augmentation des émissions anthropiques telles que l'exploitation des mines de charbon, du gaz naturel et du pétrole ainsi que leur transport, ont joué un rôle déterminant dans l'augmentation du méthane atmosphérique après 2005 alors qu'ils ne sont que des contributeurs secondaires au budget total du méthane.

Acknowledgments

First of all, I would like to thank my supervisor Dr. Emmanuel Mahieu for his boundless support. His crucial guidance through those four years helped set my research career on the right track. I am grateful for his time spent on continuous training, constructive discussions, and proofreading. He provided me the best working conditions and helped me find my way.

I am also very thankful to Dr. Agnès Perrin (Laboratoire Interuniversitaire des Systèmes Atmosphériques, Paris, France), Dr. Jean-François Müller (Belgian Institute for Space Aeronomy), Prof. Louis François and Prof. Michel Erpicum (University of Liège) who have agreed to join my thesis committee. Prof. Pierre Magain (University of Liège) is further acknowledged for accepting to be the chairman of my jury.

Many thanks further go to my colleagues of the GIRPAS team, contributors to collecting FTIR data at Jungfraujoch over the years, for their constant support during this research: Benoit Bovy, Bernard Lejeune, Bruno Franco, Olivier Flock, Diane Zander, Christian Servais, and Ginette Roland. I also would like to thank Rodolphe Zander who started it all. He will be deeply missed.

This work has been supported by the AGACC-II project of the Science for Sustainable Development (SSD) program and ACCC project of the PRODEX program. Both SSD and PRODEX programs are funded by the Belgian Science Policy Office (BELSPO, Brussels). Support is also brought by the NORS project from the European Community's Seventh Framework Programme. We thank the International Foundation High Altitude Research Stations Jungfraujoch and Gornergrat (HFSJG, Bern) for supporting the facilities needed to perform the observations. The Swiss GAW-CH program is further acknowledged.

I personally would like to thank my parents who always taught me to be the best version of myself. I would like to tell my mother that love is what makes us grow together against all odds, no matter the differences that set us apart more often than we may have wished. To my father, I know that you are a proud father and that you are there when needed. I would like to dedicate this work to my wonderful little sister and three little brothers who let me enjoy the amazing opportunity of being their big sister. Now it is your turn to find what makes you feel alive and to give everything in your power to make it real no matter what it may be. I would like to thank my dearest friend Pauline who always found the bright side of every situation even when I thought there was none. I also would like to thank my friends and my #friends who showed so #muchlove and endured every good and bad day I had for four years now. You guys are all amazing!

Finally, I would like to thank my dearest, loveliest and charming Juan who showed support even when I did not expect him to (and those days were rare…), who showed confidence when I had none left and who showed patience when I was in over my head. I couldn't have dreamed of a better partner for this adventure that is a doctorate and for the greatest adventure of all that is life.

Table of contents

Introduction

Doing research in geophysics, more specifically in atmospheric chemistry and composition, is the obvious choice when having a bachelor's degree in chemistry and a master's degree in climatology. While the background in chemistry I acquired provides a knowledge on the composition, structure and properties of matter, two years studying climatology taught me the phenomena of climatic conditions. This multidisciplinary formation enables me to study topics applied to environmental and societal questions.

Since the composition of the Earth's atmosphere continuously evolves, notably due to the accumulation of an increasing number of gaseous constituents – very often chemically and radiatively active – emitted from the surface by human activities, the state of the Earth's atmosphere has been in the midst of preoccupations since the 1980s. More specifically, in 1985, with the discovery of the ozone hole [*Farman et al.*, 1985], and during the Vienna Convention for the Protection of the Ozone Layer where the United Nations raised awareness on the impact of anthropogenic activities on the atmospheric composition change and its consequences. The Vienna Convention outlined the responsibilities of the signatory states for protecting human health and environment against the effects of ozone depletion. In 1987, on the basis of the Vienna Convention, the Montreal protocol on substances that deplete the ozone layer was negotiated and signed. After two substantial amendments in 1990 and 1992, the Montreal Protocol was ratified by 197 states who were legally bound to phase out the production and consumption of compounds that deplete ozone in the stratosphere such as chlorofluorocarbons, halons, carbon tetrachloride, and methyl chloroform. Nowadays, the Montreal Protocol proved to be the "the single most successful international agreement to date" [K. *Annan*, Former Secretary General of the United Nations, 2003].

In 1992, consequently to the development of concerns about climate change, an international environmental treaty was negotiated and adopted at the Earth Summit, in Rio de Janeiro, the United Nations Framework Convention on Climate Change (UNFCCC). The governing body of the international convention is called a conference of the parties (COP) and takes place every year since 1995. In 1997, based on the principle that some anthropogenic emitted atmospheric gases, called greenhouse gases, interact with incoming and outgoing radiation and thus play a role in controlling the temperature of the Earth, the Kyoto Protocol was adopted outlining the reduction of their emissions to limit their concentrations in the atmosphere to "a level that would prevent dangerous anthropogenic interference with the climate system" [*Article 2 of the United Nations Framework Convention on Climate Change*, 1997]. The Kyoto Protocol is based on the principle that developed countries are historically responsible for the current levels of greenhouse gases in the atmosphere differentiating the common responsibilities of the 191 ratifying countries. In 2010, at the COP 16, parties to the UNFCCC agreed on the need to take urgent action to reduce global greenhouse gas emissions to limit future global warming and therefore limit the global average temperature below 2°C relative to the pre-industrial temperature level [*Report of the Conference of the Parties on its sixteenth session, United Nations*, 2011].

In order to help governments and policymakers develop informed decisions about ozone depletion and climate change, the Chemical Science Division (CSD) of the National Oceanic and Atmospheric Administration (NOAA, www.noaa.org), ensured to provide clear scientific information for decisions. Since its inception in 1987, the Scientific Assessment of Ozone Depletion sponsored by the World Meteorological Organization (WMO) and the United Nations Environment Programme (UNEP) contributed and still contributes to our understanding of the processes controlling the ozone distribution and changes in the framework of the Montreal Protocol [Latest Ozone Assessment Report; *World Meteorological Organization*, 2014a]. Regarding climate change, the leading body for its assessment is the Intergovernmental Panel on Climate Change (IPCC, www.ipcc.ch). Established in 1988 by the UNEP and the WMO, it provides a clear scientific view on the current state of knowledge in climate change and its potential environmental and socio-economic impacts. The role of the IPCC is to review and assess the most recent scientific information produced worldwide [Latest assessment report; *Intergovernmental Panel on Climate Change (IPCC)*, 2014].

As atmospheric components interacting with incoming and outgoing radiation affect the Earth's energy budget thanks to their physical properties (described in Chapter 1), it is possible to determine their concentrations in the atmosphere from infrared solar observations through a process called inversion. In such context, the "Groupe InfraRouge de Physique Atmosphérique et Solaire" (GIRPAS, Institute of Astrophysics and Geophysics, University of Liège) observes solar radiation in the infrared since the mid-fifties at the International Scientific Station of the Jungfraujoch (ISSJ, Swiss Alps, 46.5°N, 8.0°E, 3580 m a.s.l.), in the framework of the Network for Detection of Atmospheric Change (NDACC, www.ndacc.org). Systematic monitoring of the chemical composition of the Earth's atmosphere started in 1984 by using two state-of-the-art Fourier Transform InfraRed (FTIR) instruments, while grating spectrometers were used previously in the early 1950s, and from the mid-1970s onwards.

Through this work, we focused our interest into three atmospheric compounds, i.e. methane, ethane and methanol (see Chapter 2). The three of them have an impact on air quality since their removal pathway affects the production of ozone in the atmosphere whereas methane and ethane act as direct and indirect greenhouse gases, respectively.

The primary challenge of this work is to develop and optimize strategies for inversion of methane, ethane and methanol concentrations from FTIR spectra recorded at the Jungfraujoch station. The development of those strategies, described in Chapter 3, consists in: systematic search for and evaluation of absorption lines of the target species and determination of the best combination of spectral windows, spectroscopic linelist (for the target and interfering species), a priori vertical distribution profile, among others in order to limit uncertainties and maximize the altitude sensitivity range. The choice of the best retrieval strategy is further determined by analysis of uncertainties associated to the inversion by a method developed in the framework of this thesis.

In the second part of this work, dedicated to the results obtained, we address the long-term time series of methanol above Jungfraujoch (see Chapter 4) whose inversion is very challenging due to high ozone interferences. In addition to long-term trend, analysis of the seasonal cycle of methanol in the atmosphere above Jungfraujoch is presented along with analysis of the diurnal variation. Those analysis are supported and compared with in situ surface measurements, satellite observations and Chemical Transport Model simulations.

Regarding ethane, improved spectroscopic parameters are combined to optimize the retrieval strategy of ethane from ground-based FTIR solar observations recorded at the Jungfraujoch station. A time series of ethane above Jungfraujoch going from 1994 onwards along with analysis of long-term trend are presented in Chapter 5 in addition to comparisons between ethane seasonal cycle as observed at Jungfraujoch and as simulated by the Chemical Transport Model GEOS-Chem.

As of methane, the source(s) responsible for its recent global increase since the mid-2000s remain unidentified [*Kirschke et al.*, 2013]. Therefore, we investigate on its concentration changes since 2005 using FTIR solar observations performed at 10 ground-based sites, all members of the NDACC. As support, we used the GEOS-Chem model tagged simulation that allows us to quantify the contribution of each emission source (or one sink) to the global methane change based on emissions inventories and transport. Analysis of methane changes since 2005 as simulated by GEOS-Chem is given along with analysis of the contribution of each tracer to this recently observed increase.

The long-term study of methanol is subject to an article published in Atmospheric Measurement and Techniques [*Bader et al.*, 2014] while the recent ethane upturn has been reported in the Journal of Quantitative Spectroscopy and Radiative Transfer [*Franco et al.*, 2015]. As of our research on methane changes since 2005, a manuscript is in preparation for submission in Atmospheric Chemistry and Physics in the framework of the special issue "*Twenty-five years of operations of the Network for the Detection of Atmospheric Composition Change (NDACC) (AMT/ACP/ESSD Inter-Journal SI)*". The complete investigations and results mentioned above are presented in the following chapters.

Chapter 1 – The greenhouse gases in the Earth's atmosphere

In this chapter, the physical properties that characterize the incoming and outgoing radiation are presented. The interactions between atmospheric constituents and the latter are explained as well as the impact they have on the Earth's energy budget. We further describe those atmospheric constituents in terms of concentration, concentration change since pre-industrial times and radiative impact on the Earth's energy budget.

1.1. Radiation

1.1.1. Electromagnetic spectrum

Electromagnetic radiation may be viewed as an ensemble of waves propagating at the speed of light ($c = 2.998 \times 10^8$ m.s^{-1} through vacuum). As for any wave with a known speed of propagation, frequency, wavelength, and wavenumber are interdependent. Wavenumber is the reciprocal of wavelength λ:

$$\tilde{\nu} = 1/\lambda \qquad (1.1)$$

and the frequency, ν, can be expressed as:

$$\nu = c \times \tilde{\nu} = c/\lambda \qquad (1.2)$$

Radiative transfer in planetary atmospheres involves an ensemble of waves with a continuum of wavelengths and frequencies, called the electromagnetic spectrum. It is partitioned into two categories named shortwave (λ < 4 μm) and longwave (λ > 4 μm) referring to the wavelength band encompassing most of the radiation respectively coming from the sun and emitted from the Earth (see next section). The spectrum is typically subdivided into regions as illustrated in Figure 1.1. The high frequency x-ray region, which extends from wavelengths of 10^{-5} μm to 0.01 μm, is an ionizing radiation used in many applications including medical imaging and crystallography. The ultraviolet region extending from 0.01 μm to 0.04 μm will play a role in the production of ozone (see section 1.4.3). The visible region, ranging between 0.39 and 0.76 μm, is defined by the range of wavelength that the human eye is sensitive to. The near infrared region which extends from the boundary of the visible up to ~4 μm, is dominated by solar radiation and thus included in the shortwave radiation while the remainder of the infrared region is dominated by terrestrial radiation. Finally, while microwave radiation, with wavelengths ranging from 1 mm to 1m, does not contribute to the Earth's energy balance, it is widely used in remote sensing due to its ability to penetrate through clouds [*Wallace and Hobbs*, 2006].

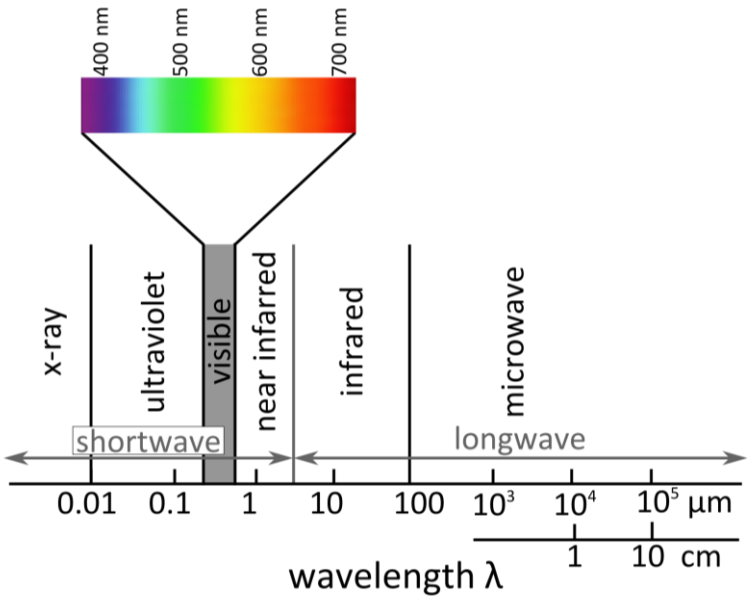

Figure 1.1. The Electromagnetic spectrum [*Wallace and Hobbs*, 2006].

1.1.2. Solar and terrestrial emission spectra

A blackbody is defined as a surface that completely absorbs all incident radiation. The intensity of radiation emitted by a blackbody, i.e. its emission spectrum is given by the Planck's function:

$$I(\lambda, T) = \frac{2hc^2}{\lambda^5} \frac{1}{e^{\frac{hc}{\lambda k_B T}} - 1} \quad (W.sr^{-1}.m^{-3}) \qquad (1.3)$$

where h is the Planck's constant (6.626 x 10^{-34} J.s), c is the speed of light in vacuum, k_B is the Boltzmann constant, λ is the wavelength of the electromagnetic radiation, and T is the absolute temperature of the blackbody. The Boltzmann constant equals 1.381 x 10^{-23} $J.K^{-1}$ and is defined as the ratio between the gas constant (R = 8.314 J.K-1.mol-1) and the number of Avogadro (N_A = 6.022 x 10^{23} mol^{-1}). The plot of the emission spectra of black bodies as a function of wavelength in Figure 1.2 exhibits a sharp wavelength cut-off, a steep rise to a maximum at wavelength λ_m, and a slow drop off toward longer wavelengths.

From this, the Wien's displacement law can be translated by the fact that there is a shift of the wavelength at which the blackbody emission spectrum is maximum, i.e. λ_m, in function of the temperature:

$$\lambda_m(\mu m) = \frac{2.898 \times 10^2 (\mu m.K)}{T\ (K)} \qquad (1.4)$$

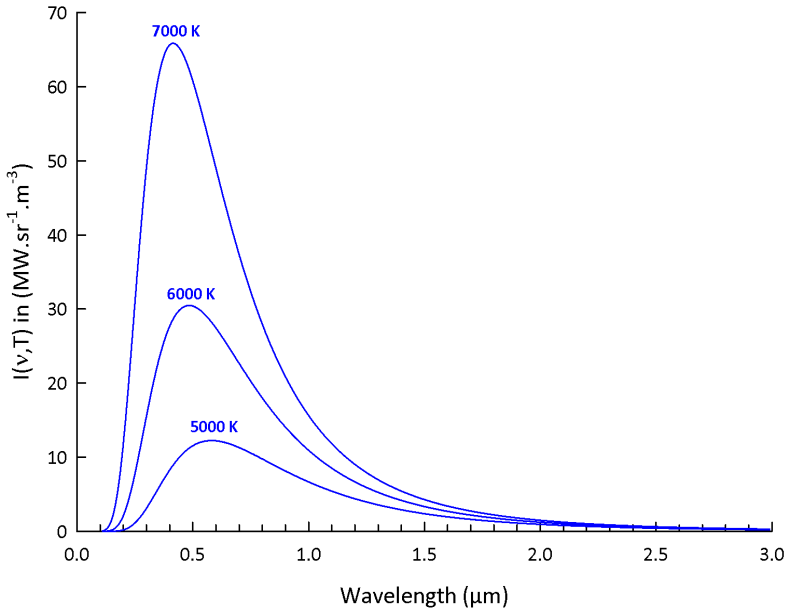

Figure 1.2. Emission spectra of blackbodies with absolute temperature as indicated. Based on [*Wallace and Hobbs*, 2006].

The equation (1.4) is obtained by differentiating I(λ,T) with respect to λ and setting the derivative to zero. In fact, the respective emission spectra of the sun with an absolute temperature of 5780 K and of the Earth whose absolute temperature amounts at 255 K implies that solar radiation is concentrated in the visible region and near infrared (shortwave, λ < 4 μm) while radiation emitted from the Earth is confined to the infrared (longwave, λ > 4 μm), as shown in Figure 1.3.

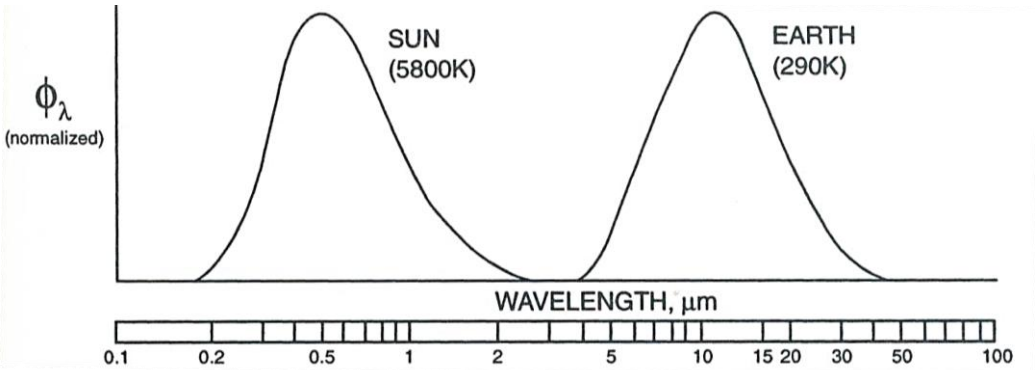

Figure 1.3. Solar and terrestrial emission spectra. [*Jacob*, 1999].

Since solar and terrestrial radiation occupy different ranges of the electromagnetic spectrum, the Earth's atmosphere is relatively transparent to incoming solar radiation and opaque to outgoing infrared radiation emitted by the Earth's surface.

1.2. Interaction mater radiation

1.2.1. Absorption lines

The internal energy (E) of a molecule can be divided into kinetic (E_k) due to thermal agitation, electronic (E_e), rotational (E_r) and vibrational (E_v) energies:

$$E = E_k + E_e + E_r + E_v \tag{1.5}$$

The last three kind of energy are quantized, meaning that the energy stored by the molecule can only correspond to specific levels that depend on the molecule characteristics (energy levels illustrated in Figure 1.4). A molecule may undergo a transition of its internal energy level to a higher level by absorbing electromagnetic radiation or to a lower level by emitting radiation with discrete changes in energy level ΔE. In theory, an absorption corresponding to the transition from a lower level of energy E'' to a higher level E', as a result of incident radiation, equals:

$$\Delta E = E'' - E' = h\nu_0 \tag{1.6}$$

where ν_0 is the frequency of the absorption line center and h is the Planck's constant. As illustrated in Figure 1.4, electronic transitions, i.e. transitions to a higher electronic state, generally require UV radiation while rotational transitions require far-infrared or microwave radiation (> 20 μm). Finally, vibrational transitions require infrared radiation (0.7-20 μm), corresponding to the wavelength range of peak terrestrial radiation (see Figure 1.3).

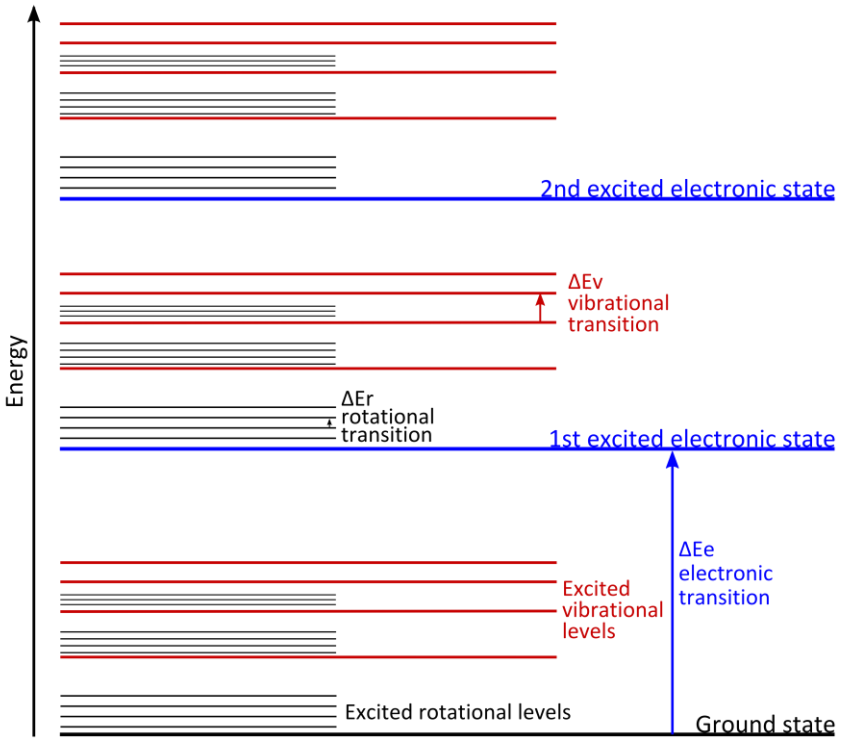

Figure 1.4. Molecule energy levels.

The probability for a particular spectroscopic transition to take place is expressed through quantum selection rules that are used to determine whether a transition is allowed or not. For vibrational transitions, the selection rule for a transition between two vibrational levels v is:

$$\Delta v = \pm 1, \pm 2, \pm 3, \ldots \quad (1.7)$$

The transition from v = 0 to v = 1 is called the fundamental vibration, while transitions with larger Δv are called overtones. Moreover, while |Δv| > 1 are allowed, the intensity of the peaks become weaker as |Δv| increases.

Regarding the rotational selection rule, it requires that transitions between rotational levels, associated to the quantum number J, with:

$$\Delta J = \pm 1 \quad (1.8)$$

are allowed. Transitions with ΔJ = 1 are defined as R branch transitions, while those with ΔJ = -1 are defined as P branch transitions. Transitions corresponding to ΔJ = 0, defined as Q branch transitions are allowed only when there is an additional electronic or vibrational transition involved. A transition of energy levels combining both a rotational and vibrational transition are called ro-vibrational transition. The ro-vibrational transitions allowed and associated with the fundamental vibration are illustrated in Figure 1.5.

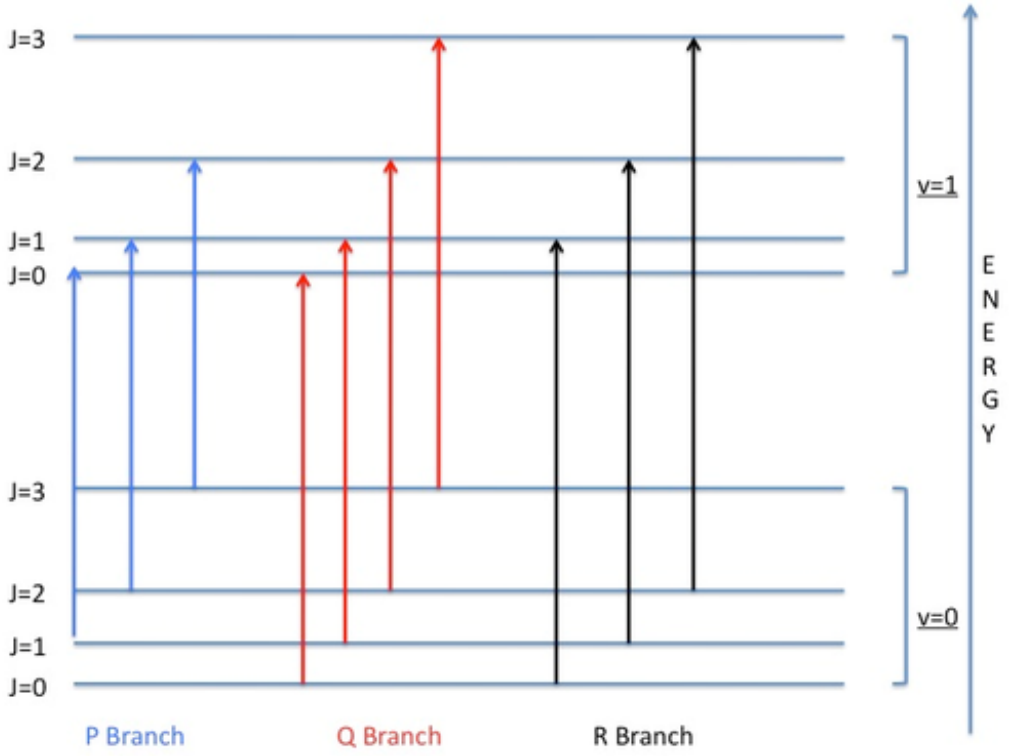

Figure 1.5. Schematic diagram of P, Q, and R branch transitions. [*UC Davis ChemWiki*, 2015]

1.2.2. Vibrational modes

In infrared spectroscopy, an additional selection rule from quantum mechanics is that vibrational transitions are allowed only if there is a change in the dipole moment. A molecule presents a dipole moment when it holds a non-uniform distribution of positive and negative charges on the various atoms it is made of. The combinations of the atomic displacements that give the simplest description of molecular vibrations are called the normal modes of vibration (NMV). The NMVs depend on the symmetry of the molecule and on the number of atoms it bears. To each NMV is associated a frequency of vibration. The vibrational state of a molecule with N atoms is defined by a combination of (3N-6) normal modes of vibrations (except for linear molecules that have 3N-5 NMVs). From this, the frequency of overtones is a linear combination of the frequencies associated with the NMVs.

For example, a molecule of carbon dioxide (CO_2) has four normal modes of vibration as illustrated in Figure 1.6 and bears an increment of positive charge on the atom of carbon and an increment of negative charge on each oxygen atom. CO_2 is not infrared active when it stretches symmetrically (v_1 mode), since it has no dipole moment in this mode due to a perfectly symmetric distribution of charges. Oppositely, the bending (v_2) or the asymmetric stretching (v_3) of CO_2 changes the dipole moment of the molecule. Therefore, the v_2 and v_3 modes are infrared active. In addition, CO_2 has another bending mode in a different plane that has the same energy. Two NMVs with the same frequency, i.e. energy, are called degenerated levels.

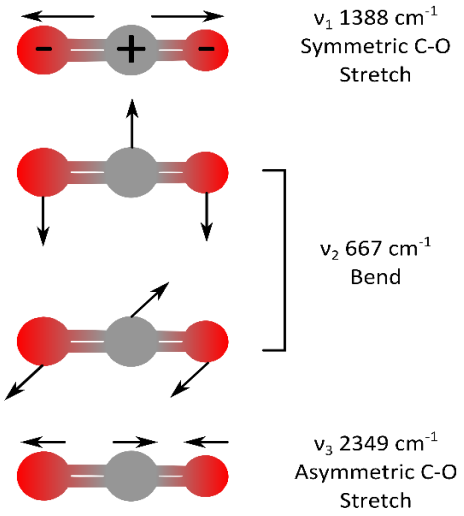

Figure 1.6. Normal modes of vibration of CO_2. Wavenumber values associated to each NMV is given on the right hand side [*NASA Astrobiology Institute's Virtual Planetary Laboratory*, 2015].

In brief, thanks to the molecules physical properties, we may identify key signatures of atmospheric components. Indeed, from a spectrum of transmitted light, spectroscopists may distinguish frequencies for which there is absorption of infrared radiation, assign them to a molecule and determine the corresponding quantum numbers of the transition.

1.2.3. Broadening of absorption lines

In practice, the absorption of radiation is not purely monochromatic. Indeed, the absorption lines of molecules are widened due to the uncertainty on the frequency of the absorption. This natural broadening allows for an interval (ν_0-$\Delta\nu$, ν_0+$\Delta\nu$) within which the absorption is significant. However, this broadening is considered to be negligible compared to the broadening due to the motions and collisions of the gas molecules. The integrated intensity of the line, S(T) is written:

$$S(T) = \int_{\nu_0-\Delta\nu}^{\nu_0+\Delta\nu} \varepsilon \, d\nu \qquad (1.9)$$

where ε is the absorption coefficient defined as

$$\varepsilon = S(T).f(\nu - \nu_0, T, p) \qquad (1.10)$$

The function f is the line profile; it reflects the distribution of the absorption around the frequency ν_0. It depends on the temperature and the pressure and is normalized:

$$\int_{\nu_0-\Delta\nu}^{\nu_0+\Delta\nu} f \, d\nu = 1 \qquad (1.11)$$

The relative motion of the absorbing molecule with respect to the absorbed photon results in what is called the Doppler effect, causing the broadening of the absorption line. The Doppler line shape is a Gaussian distribution expressed by the following equation:

$$f_D(\nu - \nu_0) = \frac{1}{\alpha_D\sqrt{\pi}} \, exp\left[-\left(\frac{\nu-\nu_0}{\alpha_D}\right)^2\right] \qquad (1.12)$$

where ν_0 is the position of the center of the line. The half-width, i.e. the distance between the center of the line and the points at which the amplitude is equal to half the peak amplitude equals:

$$\alpha_D\sqrt{ln\,2} \qquad (1.13)$$

where

$$\alpha_D = \frac{\nu_0}{c}\left(\frac{2kT}{m}\right)^{1/2} \qquad (1.14)$$

and where m is the mass of the molecule, c the speed of light, k is the Boltzmann constant, and T is the temperature.

Inelastic collisions between two molecules also contributes to the broadening of the line shape. It is called the pressure broadening. Its corresponding line shape is a Lorentzian profile characterized by the following function:

$$f_L(\nu - \nu_0) = \frac{\alpha_L}{\pi[(\nu-\nu_0)^2 + \alpha_L^2]} \qquad (1.15)$$

In this expression, the half-width is proportional to the frequency of molecular collisions. Thus, it varies depending on the pressure and the temperature:

$$\alpha_L \propto \frac{p}{T^N} \qquad (1.16)$$

where T and p are the temperature and pressure of the environment surrounding the molecule, N is a coefficient reflecting the temperature dependence of α_L and ranges between 0.3 and 1 depending on the molecule.

If physical conditions are such that both the Doppler effect and the pressure broadening contribute simultaneously and independently to the broadening of the spectral lines, their theoretical profiles are then the result of the convolution of the Lorentz profile and the Doppler one which is called the Voigt line shape:

$$f_V = f_L * f_D \qquad (1.17)$$

Those three profiles are illustrated in the Figure 1.7.

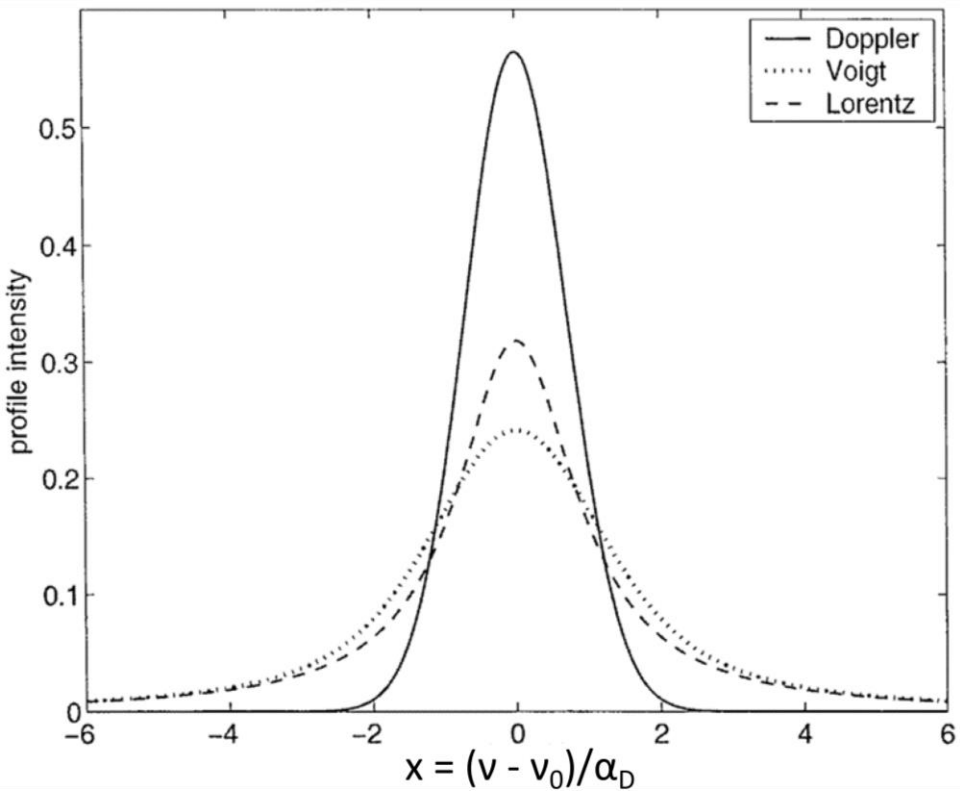

Figure 1.7. Lorentz (solid line), Doppler (dashed line) and Voigt profiles (dotted line) with $\alpha_D = \alpha_L = 1\ cm^{-1}$. [*Huang and Yung*, 2004]

1.2.3. Infrared spectroscopy

In the case of pure absorption spectra, the Beer-Lambert law may be applied. It expresses that for each frequency, the attenuation of the luminance, i.e. the absorbance, is proportional to this luminance and to the number of molecules, located on the path of the light:

$$dL(\nu) = -\varepsilon(\nu, p, T).L(\nu).C.dl \qquad (1.18)$$

where C is the number of molecules absorbing the radiation per volume unit, dl is the length of the path of the radiation and ε is the absorption coefficient which depends on the frequency ν, the temperature T and the pressure p. Considering an initial radiation, L_0, the transmittance will be defined as:

$$T = \frac{L}{L_0} \qquad (1.19)$$

Therefore, knowing L_0, from the measurement of the transmittance, we can quantify the amount of molecules responsible for the absorbance.

Hence, we can determine the atmospheric composition and quantify it with infrared spectroscopy thanks to physical properties such as:

- vibrational transitions of a molecule emitting infrared radiation;
- vibrational transitions of a molecule occurring at a specific energy, frequency and wavenumber;
- the amount of energy absorbed being directly proportional to the number of molecules absorbing.

1.3. The greenhouse effect

As detailed in *Stocker et al.* [2013], solar radiation powers the climate system. Indeed, the main source of heat is solar energy. While some solar radiation is reflected by the Earth and the atmosphere, about half the solar radiation is absorbed by the Earth's surface and warms it. On the other side, some of the infrared radiation emitted from the Earth's surface and that passes through the atmosphere is trapped by clouds and some atmospheric components called greenhouse gases. Indeed, the efficiency of absorption of radiation by the atmosphere is illustrated in Figure 1.8 in parallel with the solar and terrestrial emission spectra of Figure 1.3. On Figure 1.8, major absorbers are illustrated and they will be described in the next section. The region where the absorption is minimum is called the atmospheric window and it covers the 8-14 µm wavelength range.

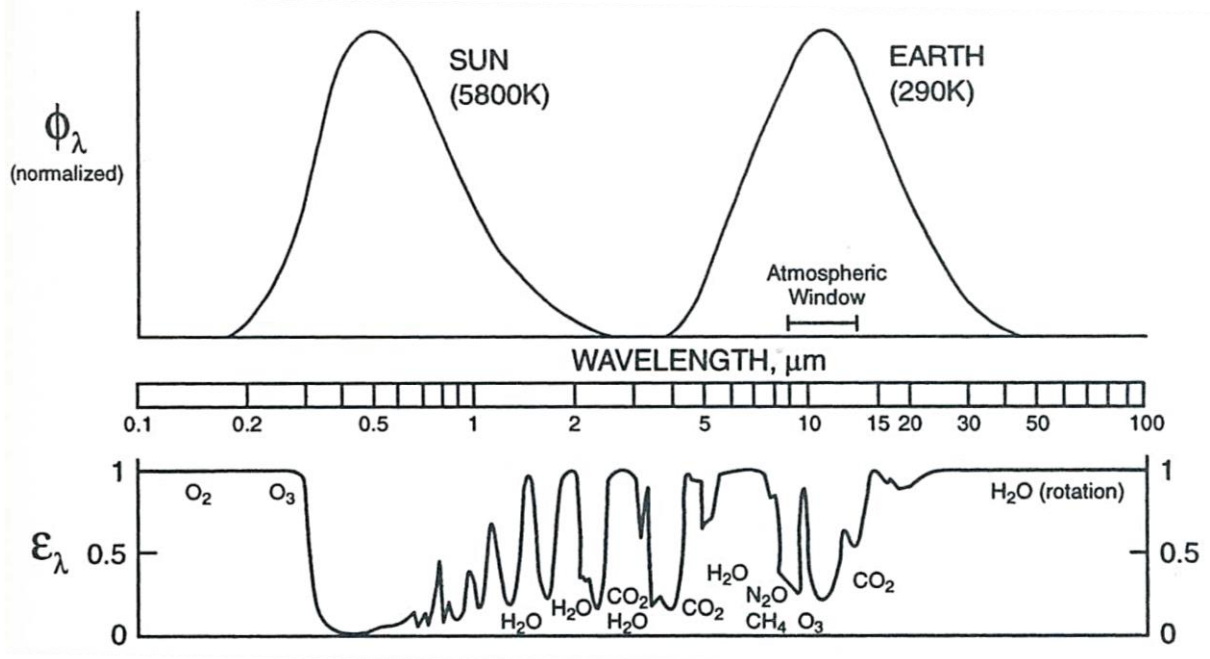

Figure 1.8. Efficiency of absorption of radiation by the atmosphere as a function of wavelength. Major absorbers are identified. [Jacob, 1999]

The greenhouse effect (Figure 1.9) is therefore the re-emission of infrared radiation in all directions by the atmosphere leading to the warming of the surface. It has been established by *Stocker et al.* [2013] that without the natural greenhouse effect, the average temperature at Earth's surface would be around -18 °C. However, human activities have greatly intensified this natural greenhouse effect [*Stocker et al.*, 2013].

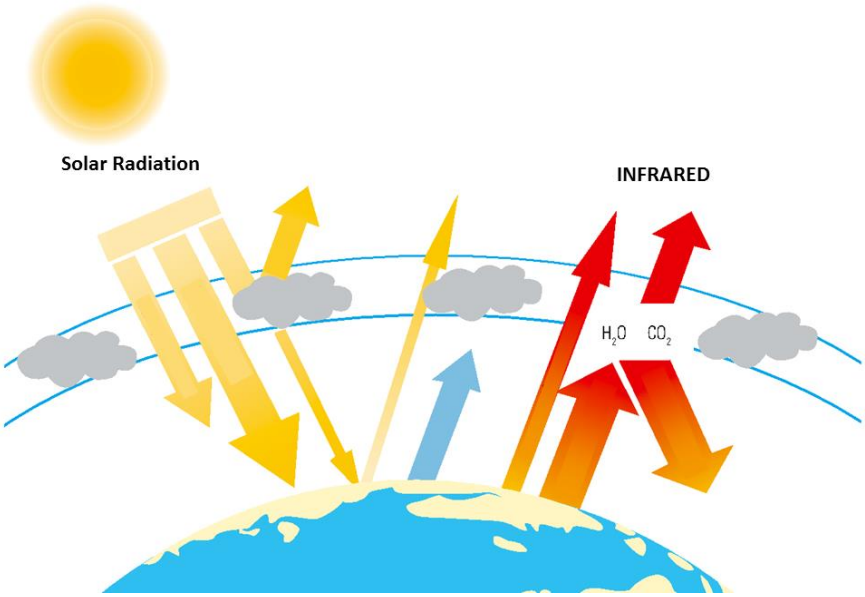

Figure 1.9. The greenhouse effect. [http://etat.environnement.wallonie.be/]

To measure the influence of atmospheric components on the balance of incoming and outgoing energy in the Earth-atmosphere system, the radiative forcing (RF) is defined and expressed in watts per square meter ($W.m^{-2}$). It is an index of the importance of the considered atmospheric component to the climate change mechanism since a positive RF leads to surface warming, negative RF leads to surface cooling. In the latest report of the International Panel for Climate Change [IPCC, *Stocker et al.*, 2013], the radiative forcing is calculated at the tropopause or at the top of the atmosphere.

In order to compare the relative impact of the greenhouse gases on the climate change, the IPCC defines a Global Warming Potential index (GWP) which is based on the time-integrated global mean radiative forcing of a 1 kg pulse emission of an atmospheric gas relative to the emission of the same amount of the reference gas: CO_2 [*Shine et al.*, 1990]. The time period on which the global mean radiative forcing is integrated is commonly fixed at a hundred years ("100-year horizon"). This notion is therefore not absolute. In brief, the GWP expresses the amount of heat "trapped" over a hundred years by a certain mass of the considered gas in comparison to a similar mass of carbon dioxide.

1.4. The Earth's atmosphere

1.4.1. The atmosphere's temperature profile

The atmosphere is defined by layers delimited by a reversal of the temperature gradient (i.e. the variation of temperature with altitude). The layers are named, from space to the surface: the exosphere, the thermosphere, the mesosphere, the stratosphere and the troposphere (see Figure 1.10). The exosphere, starting around 500 km, is the layer where collisions are sparse enough for particles to follow quasi-ballistic trajectories so that lighter ones such as atomic and molecular Hydrogen or Helium atoms can escape the gravity field (if their speed is higher than the escape velocity, 11km/s) during the long intervals between molecular collisions.

Starting at around 140 km, the thermosphere, with a positive temperature gradient due to absorption of highly energetic solar radiation, is where the heat is propagated by conduction. Below the altitude of around 100 km, at the turbopause, the turbulent mixing dominates. This region is known as the homosphere and extends down to the surface. The homosphere is the region of the atmosphere where the chemical composition is uniform for inert chemical species. For example, the ratio O_2:N_2 remains constant at 21:78 whereas highly reactive chemicals tend to exhibit great concentration variability throughout the homosphere. By opposition, the region above the turbopause is the heterosphere, where molecular diffusion dominates and the chemical composition of the atmosphere varies according to chemical species.

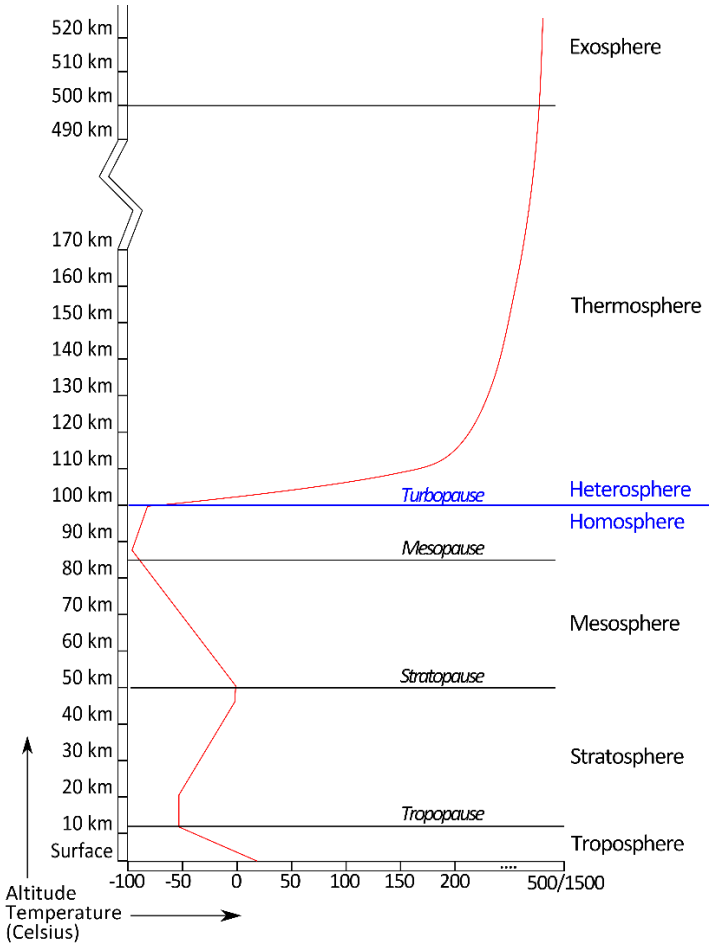

Figure 1.10. Atmospheric temperature profile regions.

Below the thermosphere lies the mesosphere where vertical heat exchanges take place between a minimum of temperature of -73 °C at the mesopause (85 km) where infrared radiation is emitted through space by components such as carbon dioxide (CO_2) or nitrogen monoxide (NO) and a maximum of 0 °C at the stratopause (50 km) where ozone (O_3) absorbs solar radiation with a wavelength of less than 300 nm. This results in a negative temperature gradient.

The stratosphere, a stratified and vertically stable domain due to a positive temperature gradient extends below the stratopause. This stratification inhibits vertical movement and therefore favors rapid horizontal movements. Within the layer, heat is mostly propagated by radiation. The stratosphere is extremely dry and contains around 90 % of the atmospheric ozone which constitutes the ozone layer. The stratosphere has the potential to significantly affect the conditions at the surface. In fact, since the ozone layer absorbs around 98 % of the ultraviolet radiation, changes in stratospheric ozone imply changes in surface ultraviolet irradiance and therefore changes in the supply of tropospheric ozone (see section 1.4.3).

The stratosphere ends at the tropopause, a transition zone, defined by the modification of temperature gradient causing it to be stable. The tropopause acts as dynamic barrier thus limiting the income of constituents from the troposphere to the stratosphere. The altitude of the tropopause varies with season and latitude (See Figure 1.11) and ranges between ~8 km at the Poles and ~18 km at the Equator.

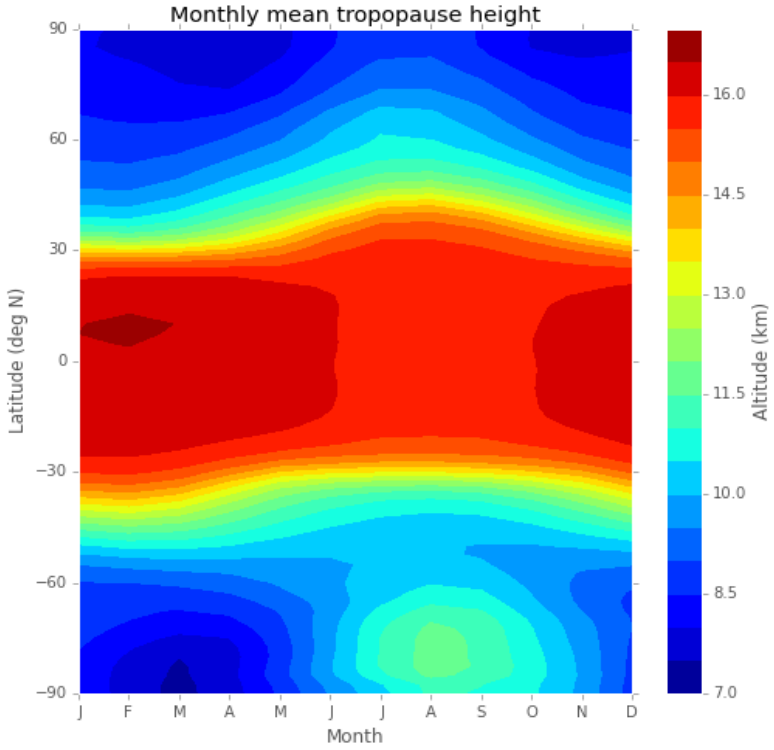

Figure 1.11. Monthly mean tropopause height from NCEP reanalysis [*NOAA/ESRL*, 2015].

Finally, the lowest layer of the atmosphere is named troposphere and contains more than 80 % of the atmospheric mass. The troposphere is the layer where occur the most significant weather events as well as horizontal and vertical atmospheric motions. The temperature decreases with increasing altitude at a rate typically between 5 °C (saturated adiabatic lapse rate) and 10 °C (dry adiabatic lapse rate) per kilometer to reach around -55 °C at the tropopause. Since convection ensures vertical energy and matter exchanges at time scales of a few weeks, the troposphere is dynamically unstable. It is divided into two layers: the atmospheric boundary layer with an average thickness of 1 km that is directly influenced by the surface (i.e. changes in temperature and humidity) and the free troposphere that lies above the latter.

1.4.2. Global atmospheric circulation

Global circulation in the atmosphere plays a major role in the vertical and latitudinal distribution of trace gases. Indeed, the distribution of atmospheric components with relatively long atmospheric lifetime is not only governed by chemical processes but also by transport through the atmosphere. In the global circulation, we distinguish the zonal circulation (along a latitude circle) and the meridional circulation (along a meridian).

The zonal circulation is illustrated in Figure 1.12 and can be divided into five zones. The direction of zonal winds is governed by the Coriolis effect. Indeed, due to the Earth's rotation, the Coriolis forces induce the deviation of a horizontally moving object on Earth. Therefore, the Coriolis forces deviate air masses of the Northern Hemisphere towards the East, while air masses of the Southern Hemisphere are deviated towards the West. The first zone is the intertropical zone (between the latitudes 30°N and 30°S) that is dominated by North-East trade winds in the Northern hemisphere and by South-Eastern trade winds in the Southern Hemisphere. Trade winds converge on the InterTropical Convergence Zone (ITCZ). The ITCZ is a highly convective band of about hundreds kilometers characterized by heavy rainfalls. The temperate zones characterized by western winds called westerlies extend from 30° to 60° of latitude in both hemispheres. Finally, the polar zones beyond 60° of latitude, are characterized by easterlies, i.e. eastern winds.

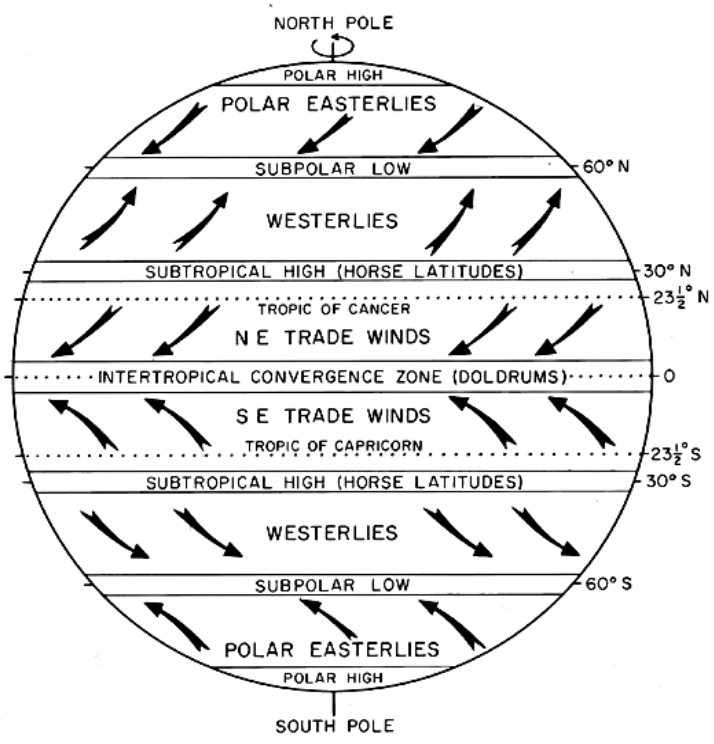

Figure 1.12. Atmospheric zonal transport [Baker et al., 1986].

The meridional circulation is illustrated in Figure 1.13. In the troposphere, the meridional circulation is associated with convection and can be resumed into three types of convective cells. The Hadley cells are

characterized by convection at the ITCZ and extend to around 30° at subtropical latitudes with subsidence of airmasses. The polar cells starting from 60° where warm and moist air masses rise due to convection and move through the pole. When the airmasses reach the polar area, it has cooled considerably and descends to a cold, dry high-pressure area, the polar high. At the polar highs, cold low-pressure areas strengthened in the winter spanning less than 1 000 kilometers in diameter are formed. Polar stratospheric clouds that support heterogeneous chemical reactions may form inside polar vortices at very low temperatures [- 78 °C; *World Meteorological Organization*, 2014b]. Within each polar vortex, due to the Coriolis effect, the air circulates respectively in the counter-clockwise and clockwise direction in the Northern and Southern Hemisphere. Finally, due to the subsidence at the subtropical high associated with the Hadley cell and the convection at the subpolar low associated with the polar cell, a circulation cell between 30° and 60° of latitude is formed, the Ferrel cell.

In the stratosphere, the meridional circulation is governed by the Brewer-Dobson circulation. This basic physical model had been proposed by Dobson and Brewer to explain observations of high concentration of ozone in the Arctic in spring and low concentrations in the Tropics [*Dobson et al.*, 1929; *Dobson*, 1956] and the stratospheric distribution of water vapor [H_2O; *Brewer*, 1949]. While numerous models described the Brewer-Dobson circulation, it can be resumed into two circulation cells. First, the single-cell time-averaged model referred as the Brewer-Dobson circulation in *Butchart* [2014] describes how air circulates by a slow mean motion into the stratosphere at the equator, moves poleward in the stratosphere and sinks into the troposphere in temperate and polar regions [*Brewer*, 1949]. In addition, *Plumb* [2002] described how air circulates at higher altitude in the stratosphere from the tropics to the winter hemisphere.

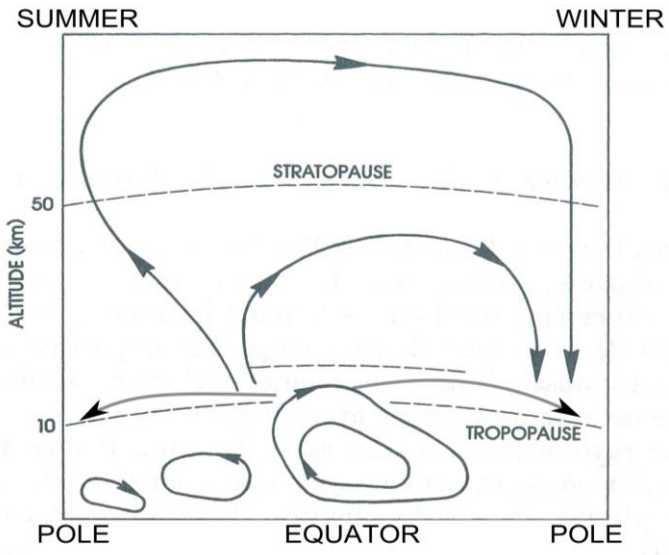

Figure 1.13. Atmospheric meridional transport. Figure from [*Mégie*, 1989] *edited on the basis of* [*Plumb*, 2002].

In contrast to the stratospheric Brewer-Dobson circulation, the mesospheric mass transport is only from the summer to winter pole. At higher levels there is ascent over the summer pole and descent over the winter pole with a well-defined flow towards the winter pole above 50 km [*Murgatroyd and Singleton*,

1961; *Dunkerton*, 1978]. This mechanism is strong enough to pump significant descent of mesospheric air deep into the stratosphere, as shown in Figure 1.13.

Finally, stratospheric-tropospheric exchange (STE) will have an important role on the vertical distribution of some atmospheric components. The upward exchange happen slower due to the stratification of the stratosphere. Indeed, it takes 5 to 10 years for exchanges from the troposphere to the stratosphere while components are removed from the stratosphere to reach the troposphere after only 1 to 2 years. The STE will impact the stratospheric ozone depletion (by upward and downward transport through the tropopause of species involved in the removal mechanism of ozone) as well as the radiative forcing (by downward transport from the stratosphere of greenhouse gases such as ozone) [*Holton et al.*, 1995].

1.4.3. Atmospheric composition

The Earth's atmosphere, among other planets of the solar system, has a specific composition which can be depicted in terms of major, minor and trace constituents (Table 1.1). The Earth's atmosphere is composed mainly of nitrogen (N_2), oxygen (O_2), and argon (Ar). These gases do not interact with the infrared radiation emitted by the Earth and have limited interaction with incoming solar radiation. Regarding minor constituents such as carbon dioxide (CO_2), methane (CH_4), nitrous oxide (N_2O) and ozone (O_3), while they contribute to less than 0.1 % of the total atmospheric content, they play a crucial role in the Earth's energy budget as greenhouse gases since they absorb and emit infrared radiation. Moreover, the atmosphere contains water vapor, which is a natural greenhouse gas. Its mixing ratio is highly variable, but is typically in the order of 1%.

Gas Name	***Chemical Formula***	***Percent Volume***
Major Constituents		
Nitrogen	N_2	78.08 %
Oxygen	O_2	20.95 %
Argon	Ar	0.93 %
Minor Constituents		
Carbon Dioxide	CO_2	0.039 %
Stratospheric Ozone	O_3	0.0005 %
Methane	CH_4	0.00018 %
Nitrous Oxide	N_2O	0.0000326 %
Water vapor	H_2O	variable
Trace gases		
CFC-12	CCl_2F_2	$5.28\ 10^{-8}$ %
CFC-11	CCl_3F	$2.37\ 10^{-8}$ %
HCFC-22	$CHClF_2$	$2.13\ 10^{-8}$ %
HFC-23	CHF_3	$2.4\ 10^{-9}$ %
Sulphur hexafluoride	SF_6	$7.3\ 10^{-10}$ %

Table 1.1. Dry atmosphere average composition from [*World Meteorological Organization*, 2014b] *and* [*Stocker et al.*, 2013].

More than 40 greenhouse gases have been reported by the IPCC including hydrocarbons and halocarbons [*Forster et al.*, 2007]. The main contributors to the increase in radiative forcing since pre-industrial times are detailed in the following paragraph (except for CH_4 that will be further described in chapter 2 and 6) and in Table 1.2 along with their respective concentrations [*World Meteorological Organization*, 2014b], GWP, radiative forcing and lifetime [*Stocker et al.*, 2013]. Their concentrations are expressed in mixing ratio unit. The mixing ratio or mole fraction is the ratio of the number of moles of a constituent in a given volume to the total number of moles of all constituents in that volume. It is usually reported for dry air. Units frequently used are part per million (ppm, 10^{-6}), part per billion (ppb, 10^{-9}) and part per trillion (ppt, 10^{-12}).

Greenhouse Gas	Formula	Concentration	GWP	Radiative Forcing (W m^{-2})	Atmospheric lifetime (years)
Carbon dioxide	CO_2	396 ppm[(a)]	1	1.68 ± 0.35	
Methane	CH_4	1824 ppm[(a)]	28	0.97 ± 0.23	8-10
Nitrous oxide	N_2O	325.9 ppb[(a)]	265	0.17 ± 0.04	131
CFC-12	CCl_2F_2	528.5 ppt[(b)]	10 200		100
CFC-11	CCl_3F	237.7 ppt[(b)]	4 660	halocarbons	45
HCFC-22	$CHClF_2$	213.3 ppt[(b)]	1760	0.18 ± 0.17	11.9
HFC-23	CHF_3	24 ppt[(b)]	12 400		222
Sulfur hexafluoride	SF_6	7.29 ppt[(b)]	23 500		3200

Table 1.2. Global surface concentrations (a) in 2013 from World Meteorological Organization, [2014b] *or (b) in 2011 from Stocker et al.*, [2013]*, Global Warming Potential, Radiative Forcing relative to 1750 (in W.m^{-2}) and atmospheric lifetime (in years) for the main greenhouse gases. [Stocker et al., 2013].*

Carbon dioxide, the main anthropogenic greenhouse gas, contributed to 65 % of the anthropogenic radiative forcing since 1750 (RF of 1.68 ± 0.35 W.m^{-2}). Atmospheric CO_2 never ceases to increase. In fact, it reached 142% of the pre-industrial level in 2013, which is mainly due to emissions from combustion of fossil fuels and cement production. Over the last 10 years its concentration has increased by 20.7 ppm to reach a global concentration of 396.0±0.1 ppm [*World Meteorological Organization*, 2014b]. The main natural sources of CO_2 are the animal and plant respiration and exchanges between the ocean and the atmosphere. Emissions of CO_2 in the atmosphere from human activities in the atmosphere accounts for emissions through fossil fuel burning (transport, heating, air conditioning, cement production, electricity production,…) and land use change. CO_2 main sinks are oceans uptakes (leading to ocean acidification through dissolution), soil uptakes, peatlands, forests and vegetation. In addition, the permanent increase of CO_2 enhances the ocean-atmosphere exchanges by 10 % thus increasing both the source and sink it represents for atmospheric CO_2 [*World Meteorological Organization*, 2014b].

Water vapor concentrations exhibit a very large variability in the troposphere both with space and time depending on meteorological conditions. Human activities have a weak direct impact on water vapor abundance in the atmosphere as they are connected only through climate feedbacks. Therefore, water vapor is not among the Kyoto Protocol target species [*Stocker et al.*, 2013]. In the stratosphere, the water

vapor content is controlled by transport through the tropopause region and subsequent oxidation of methane, its stratospheric source. In fact, increases in stratospheric water vapor act to cool the stratosphere but to warm the troposphere and conversely. Since 2000, stratospheric water vapor contents decreased by about 10 % which acted to slow the rate of increase in global surface temperature over 2000–2009 by about 25% compared to what would have occurred due only to carbon dioxide and other greenhouse gases [*Solomon et al.*, 2010].

Nitrous oxide is the fourth most important contributor to the anthropogenic radiative forcing and acts as an emission source of ozone-depleting substance in the stratosphere [*World Meteorological Organization*, 1985; *Prather and Hsu*, 2010] as the source of stratospheric nitrogen oxides [NO_x; *Crutzen*, 1970b]. With a radiative forcing of 0.17 ± 0.04 $W.m^{-2}$, it contributed to ~6% of the radiative forcing since 1750 [*World Meteorological Organization*, 2014b]. The pre-industrial atmospheric N_2O burden reflected a balance between emissions from soils and the ocean, and chemical losses in the stratosphere. Nowadays, additional anthropogenic emissions are mainly from synthetic nitrogen fertilizers (direct emissions from agricultural fields and indirect emissions from waterways affected by agricultural runoff), fossil fuel combustion, and biomass burning and accounts for 40 % of total N_2O emissions [*World Meteorological Organization*, 2014b]. N_2O increased by 21 % since pre-industrial level (270 ppb in 1750) to reach a mean global concentration of 325.9 ± 0.1 ppb in 2013 mainly due to synthetic nitrogen fertilizers. Between 2012 and 2013, the globally averaged N_2O concentration increased by 0.8 ppb which is comparable to the mean growth rate over the past 10 years (0.82 ppb yr^{-1}).

Halocarbons are molecules in which one or more carbon atoms are linked by covalent bonds with one or more halogen atoms (i.e. fluorine, chlorine, bromine or iodine atoms). Halocarbons are mainly known for their destructive effect on stratospheric ozone towards the release of free atoms of chlorine or bromine first described by [*Molina and Rowland*, 1974]. In addition, halocarbons are generally very strong greenhouse gases. Due to their interesting chemical and physical properties (highly stable, inert, non-flammable), halocarbons like chlorofluorocarbons (CFC) have been widely produced and used by industrial and domestic applications resulting in a rapid accumulation in the atmosphere thanks to their long lifetime (Table 1.2), in addition to natural species such as methyl bromide and methyl chloride. Since their transport and photodissociation in the stratosphere lead to the release of chlorine atoms responsible for the ozone depletion, the production of CFCs has been tightly controlled, then banned, since the Montreal Protocol in 1987. As a decisive result, concentrations of many ozone depleting and halogenated GHGs are now declining. Due to the somewhat contrasted lifetimes of halocarbons in our atmosphere, the impact of the Montreal Protocol has been more rapid for some gases than others. As the Montreal Protocol imposed a phase out of the CFCs, they have been gradually replaced by other types of halocarbons: hydrochlorofluorocarbons (HCFCs) and hydrofluorocarbons (HFCs). These two later categories of halocarbons are strong greenhouse gases by contributing to 12% of the anthropogenic radiative forcing since 1750. The anthropogenic emissions of HCFCs and HFCs are respectively regulated by the Montreal Protocol of 1987 and by the Kyoto Protocol of 1997. While CFCs and most halocarbons are decreasing, HCFCs and HFCs, are increasing at rapid rates, although they are still low in abundance [see Figure 1.14; *Stocker et al.*, 2013; *World Meteorological Organization*, 2014b]. Overall, the chlorine loadings are decreasing in both the troposphere and the stratosphere [*Carpenter et al.*, 2014].

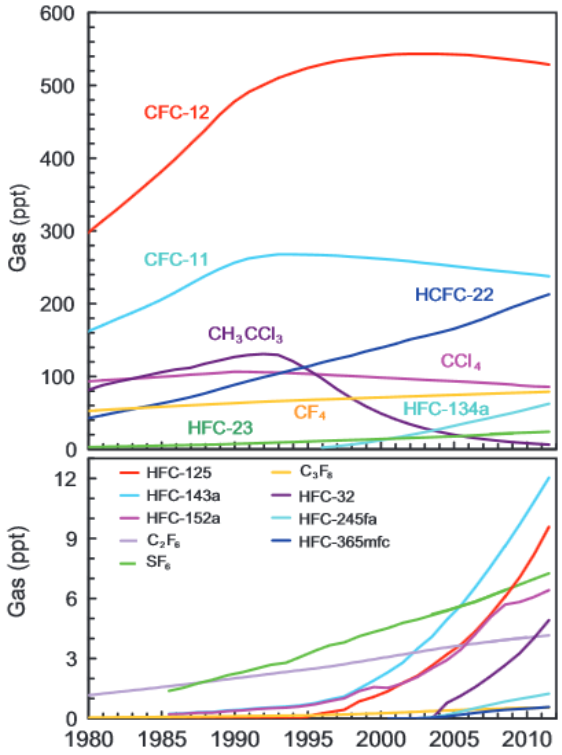

Figure 1.14. Globally averaged dry-air mixing ratios at the Earth's surface of the major halogen-containing greenhouse gases [*Stocker et al.*, 2013].

Finally, sulphur hexafluoride emissions are almost entirely anthropogenic. It is nonflammable, nontoxic, noncorrosive, relatively inert and inexpensive. It is therefore used in many technical applications, such as electrical equipment, double glazing or in shoes soles. Its current concentration is about twice the level observed in the mid-1990s. SF_6 accumulates in the atmosphere due to its very long atmospheric lifetime of 3 200 years [*Stocker et al.*, 2013].

Many pollutants, such as carbon monoxide (CO), nitrogen oxides or volatile organic compounds (VOCs), although not referred to as greenhouse gases, have small direct or indirect effects on radiative forcing. Moreover, O_3, acts as a tropospheric greenhouse gas and as a stratospheric filter for UV radiation while the hydroxyl radical (OH) is the detergent of the atmosphere by being the main sink of most tropospheric gases. Therefore, volatile organic compounds such as ethane (C_2H_6) or methanol (CH_3OH) through reaction with hydroxyl radical have an impact on radiative forcing since they limit the availability of OH to deplete most greenhouse gases. In fact, *Collins et al.* [2002] even estimated a GWP for ethane of 5.1. We therefore need to better understand the mechanisms of formation and destruction of O_3 and OH in order to apprehend the atmospheric chemistry of tropospheric components such as the gases studied through this work, i.e. methane, ethane or methanol.

1.4.4. Ozone

In the atmosphere, ozone plays crucial but different roles in the troposphere and in the stratosphere. In the stratosphere, ozone acts as a filter for ultraviolet radiation since it absorbs around 98 % of the ultraviolet radiation in the 240-300 nm range [*Delmas et al.*, 2005]. With a maximum abundance of ozone at around 25 km, ozone heats the stratosphere from inside up until 50 km which explains that the lower stratosphere is quasi isothermal until an altitude of 30 km. On the other hand, tropospheric ozone is the third most important greenhouse gas [*World Meteorological Organization*, 2014b].

a- Stratospheric ozone

In 1930, S. Chapman [1930] proposed the first theory for ozone formation in the stratosphere as part of the Chapman cycle that describes the equilibrium between the production and depletion of ozone. Stratospheric ozone is formed by photodissociation of molecular oxygen, as follows:

$$O_2 + h\nu \rightarrow O + O \qquad \lambda < 242\ nm \qquad (1.20)$$

$$O_2 + O + M \rightarrow O_3 + M + heat \qquad (1.21)$$

where M can either be O_2 or N_2. The formation of O_3 from O_2 requires the formation of a O-O bond which is an exothermic process (1.21). The energy related to this reaction is released in the stratosphere and induces its warming impacting the stratospheric temperature profile (Figure 1.9). In addition, atomic oxygen can also recombine as follows:

$$O + O + M \rightarrow O_2 + M \qquad (1.22)$$

Regarding the depletion of ozone, *Chapman* [1930] showed:

$$O_3 + O \rightarrow 2\ O_2 \qquad (1.23)$$

$$O_3 + h\nu \rightarrow O_2 + O \qquad (1.24)$$

Chapman's cycle is active only during the day where photodissociation reactions (1.20 and 1.24) are active. During the night only the 1.19, 1.20 and 1.21 reactions are active depleting all atomic oxygen.

Stratospheric ozone can also be depleted through further photodissociation reactions (1.25 and 1.26) and through catalytic cycles. The photodissociation of ozone consists of two pathways depending on the wavelength:

$$O_3 + h\nu \rightarrow O_2 + O(^1D) \qquad \lambda < 310\ nm \qquad (1.25)$$

$$O_3 + h\nu \rightarrow O_2 + O(^3P) \qquad \lambda > 310\ nm \qquad (1.26)$$

The formation of active oxygen, O^1D, returns to its fundamental state, $O(^3P)$ by collision with main components of the atmosphere, N_2 and O_2. However, in the meantime, O^1D acts as an oxidant in the stratosphere for species such as CH_4 or N_2O.

The catalytic cycle responsible for the depletion of ozone can be synthesized by:

$$X + O_3 \rightarrow XO + O_2 \quad (1.27)$$

$$\underline{XO + O \rightarrow X + O_2} \quad (1.28)$$

$$\textit{Balance :} \quad O_3 + O \rightarrow 2\,O_2 \quad (1.29)$$

where X can either be an atom of hydrogen, an hydroxyl radical [*Bates and Nicolet*, 1950], nitric oxide [*Crutzen*, 1970; *Johnston*, 1971], an atom of chlorine [*Stolarski and Cicerone*, 1974], or an atom of bromine [*Wofsy et al.*, 1975].

At a global scale, ozone concentrations reach a maximum at high latitudes and a minimum in the tropics mainly due to meridional transport. The polar vortex associated with high meridional temperature gradient in the winter hemisphere are therefore characterized by a maximum of subsidence at their edge. Therefore, high concentrations of ozone are located at the edges of the polar vortex whereas O_3 is missing from inside the vortex creating what is called the ozone hole. Inside the ozone hole occurs heterogeneous chemistry favored by polar stratospheric clouds leading to the strong depletion of ozone. The polar vortices are not symmetrical and while the southern polar vortex is very cold and very stable, the northern vortex is less stable and cold due to the more complex distribution of continents at mid- and high-northern latitudes.

b- Tropospheric ozone

Tropospheric ozone is the third most important contributor to greenhouse radiative forcing with a radiative forcing of 0.40 ± 0.20 $W.m^{-2}$ [*Stocker et al.*, 2013]. In addition, it acts as a surface air pollutant and as a precursor of the hydroxyl radical, the detergent of the atmosphere (see next section). Ozone is produced in the troposphere by photochemical oxidation of CO, CH_4 and non-methane VOCs (NMVOCs) in the presence of NO_x [*Chameides and Walker*, 1973; *Crutzen*, 1973]. In fact, the oxidation of those compounds will lead to the formation of reactive radicals that will convert NO to nitrogen dioxide or NO_2. The NO_2 formed will in turn produce ozone through the following reactions:

$$NO_2 + h\nu \rightarrow NO + O \quad (1.30)$$

$$O + O_2 \rightarrow O_3 \quad (1.31)$$

Another source of tropospheric ozone is the stratosphere-troposphere exchange (STE). Although STE is only a minor term in the global ozone budget, it carries ozone to the upper troposphere where it impacts the most the radiative forcing [*Forster et al.*, 2007]. Sinks of tropospheric ozone include photochemical and chemical reactions and dry deposition.

1.4.5. The hydroxyl radical

Because of its high reactivity with both inorganic and organic compounds, OH acts as the main detergent of the atmosphere. Indeed, oxidation by OH is the major sink for most atmospheric trace gases. Since it rapidly reacts with CO and hydrocarbons, the tropospheric lifetime of OH is very short, of about a few seconds [*Lelieveld*, 2002].

The formation of OH is governed by ozone. A small fraction of stratospheric O_3 is transported to the troposphere, which constitutes a baseline OH source. Additionally and most importantly, OH is formed from O_3 that is depleted according to (1.25) leading to the formation of $O(^1D)$:

$$O(^1D) + M \rightarrow O(^3P) + M \qquad (97\ \%) \qquad (1.32)$$

$$O(^3P) + O_2 + M \rightarrow O_3 + M \qquad (1.33)$$

$$O(^1D) + H_2O \rightarrow 2\ OH \qquad (3\ \%) \qquad (1.34)$$

Primary OH formation is thus controlled by ozone (1.25), UV radiation and water vapor (1.34). Therefore OH levels are highest in the tropics where the stratospheric ozone layer is thinnest and the absolute humidity is highest [*Lelieveld*, 2002].

Although oxidation of CH_4 and CO constitutes an efficient sink of OH, these reactions do not necessarily deplete OH due to its recycling by two pathways depending on the presence of NO_x. In the presence of NO_x, recycling of OH will lead to ozone production.

$$CO + OH \rightarrow CO_2 + H \qquad (1.35)$$

$$H + O_2 + M \rightarrow HO_2 + M \qquad (1.36)$$

$$NO + HO_2 \rightarrow NO_2 + OH \qquad (1.37)$$

$$NO_2 + h\nu \rightarrow NO + O(^3P) \qquad \lambda < 420\ nm \qquad (1.38)$$

$$\underline{O(^3P) + O_2 + M \rightarrow O_3 + M} \qquad (1.39)$$

$$\text{Balance:} \quad CO + 2\ O_2 \rightarrow CO_2 + O_3 \qquad (1.40)$$

In the absence of sufficient NO_x for example far from pollution sources (1.37) is insignificant and the alternative cycle prevails:

$$CO + OH \rightarrow CO_2 + H \qquad (1.41)$$

$$H + O_2 + M \rightarrow HO_2 + M \qquad (1.42)$$

$$\underline{O_3 + HO_2 \rightarrow 2\ O_2 + OH} \qquad (1.43)$$

$$\text{Balance} \quad CO + O_3 \rightarrow CO_2 + O_2 \qquad (1.44)$$

In the latter case O_3 is destroyed and the hydrogen oxide radicals (HO_x) can recombine into hydrogen peroxide (H_2O_2). This can terminate the radical reaction chain because a large part of the H_2O_2 is removed by dry and wet deposition. While some of the HO_x can be regained from H_2O_2 through photolysis, deposition is a definitive sink for about half the HO_x radicals that form H_2O_2 [*Lelieveld*, 2002]. In those two mechanisms, while CO is the main driver, it can be replaced by any VOC that will in turn lead to the formation of CO when oxidized.

Chapter 2 – Methane and two of its derivatives

In this work, we study methane and two of its derivatives, i.e. namely ethane and methanol. Methane, with the chemical formula CH_4, is a tetrahedral molecule made of one atom of carbon and four atoms of hydrogens, and is the simplest alkane. Ethane is a hydrocarbon with the chemical formula C_2H_6 while methanol, with the chemical formula CH_3OH, is the simplest alcohol.

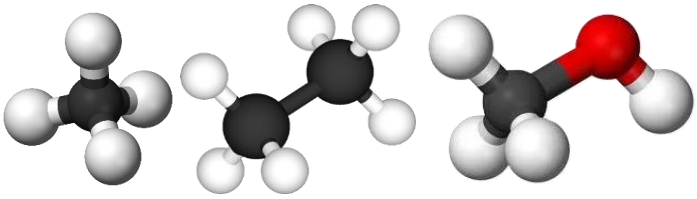

Figure 2.1. Methane, ethane and methanol.

In the atmosphere, methane is the second most abundant anthropogenic greenhouse gas with an abundance of 1824 pbb in 2013 [*World Meteorological Organization*, 2014b], ethane shows an hemispheric averaged abundance of 1 049 ppt in the Northern Hemisphere over the 1984−2010 time period [*Simpson et al.*, 2012] and methanol's abundance ranges between 1 [*Singh et al.*, 2001] and 20 ppbv [*Heikes et al.*, 2002]. Their lifetime have been estimated at around 8−10 years for methane [*Kirschke et al.*, 2013], approximately 2 months for ethane [*Rudolph*, 1995] and between 4.7 days [*Millet et al.*, 2008] and 12 days [*Atkinson et al.*, 2006] for methanol.

In the troposphere, those three gases have an impact on air quality through their removal pathway. In fact, their oxidation impacts the atmospheric content of carbon monoxide, an ozone precursor [CO; *Aikin et al.*, 1982; *Rinsland*, 2002; *Jiménez et al.*, 2003; *Duncan et al.*, 2007] and of nitrogen oxide radicals (NOx), a driver of the production and loss of tropospheric ozone. Through their tropospheric chemistry, they therefore act as ozone precursors [*Rudolph*, 1995; *Rinsland*, 2002; *Montzka et al.*, 2011; *Fischer et al.*, 2014].

In the stratosphere, while ethane and methanol's abundances remain low or even negligible, stratospheric methane influences the content of ozone and the production of water vapour an important driver of decadal global surface climate change [*Solomon et al.*, 2010].

Moreover, both methane and ethane impact the greenhouse radiative forcing. Indeed, with a radiative forcing (RF) of 0.97 ± 0.23 $W.m^{-2}$, methane is the second anthropogenic greenhouse gas after CO_2 [RF of CO_2 in 2011: 1.68 ± 0.35 $W.m^{-2}$; *Stocker et al.*, 2013]. Moreover, although CH_4 is 200 times less abundant than CO_2 [abundance of CO_2 at 396.0±0.1 ppm, *Bates et al.*, 2014], it has a global warming potential of 28 [on a 100-year time horizon, *Stocker et al.*, 2013]. As of ethane, because of its sinks, it is an indirect greenhouse gas with a global warming potential of 5.5 [on a 100-year time horizon, *Collins et al.*, 2002].

The following sections will detail how these three atmospheric compounds share common sources and sinks and how their chemistry is closely connected. In addition, vertical distribution as well as trends and seasonal cycles are described.

2.1. Budget: sources and sinks

The methane budget [*Kirschke et al.*, 2013] includes anthropogenic contributions such as domestic ruminant animals (17 %), oil and gas exploitation (12 %), waste management (11 %), coal mining (7 %), rice cultivation (7 %), biomass burning (4 %), and natural contributions such as wetlands (34 %), termites (4 %), methane hydrates and ocean (3 %). While there still remain uncertainties on its budget, above-mentioned estimated contributions to the atmospheric content of methane are based on *Fung et al.* [1991], *Chen and Prinn* [2006], *Kirschke et al.* [2013] and on emission inventories used for the GEOS-Chem v9-02 CH_4 simulation, *Turner et al.* [2015].

Processes leading to the emission of methane in the atmosphere can alternatively be regrouped into three other categories, i.e. biogenic, thermogenic and pyrogenic emissions [*Kirschke et al.*, 2013]. The biogenic sources involve microbes generating methane. They comprise anaerobic environments such as natural wetlands and rice paddies, oxygen-poor freshwater reservoirs (such as dams), digestive systems of ruminants and termites, and organic waste deposits (such as manure, sewage and landfills). The formation of CH_4 over millions of years through geological processes pertains to thermogenic source. It is vented from the ground into the atmosphere through natural features (such as terrestrial seeps, marine seeps and mud volcanoes), or through the exploitation of coal, oil and natural gas. Indeed, coal mine venting, associated gas from oil wells, and leaks from natural gas wells, storage, pipelines and end use lead to emissions of methane in the atmosphere. Finally, pyrogenic CH_4 is produced by the incomplete combustion of biomass and soil carbon during wildfires, and of biofuels and fossil fuels. Anthropogenic emission sources such as the exploitation of coal, gas and oil are mainly located in the Northern Hemisphere [*Chen and Prinn*, 2006]. On the other hand, natural sources such as biomass burning [*Hao and Ward*, 1993; *Duncan*, 2003], forested and non-forested swamps [*Fung et al.*, 1991] as well as termites, lakes and other fresh waters [*Sanderson*, 1996] show maximum values in the tropics and especially in Africa and tropical South America for the latter.

In the same way than methane, ethane is emitted from leakage from the production, transport of natural gas loss (62%) from biofuel consumption (20%) and from biomass burning (18%), mainly in the Northern Hemisphere [*Logan et al.*, 1981; *Rudolph*, 1995; *Xiao et al.*, 2008]. In contrast, biogenic and oceanic sources show really small contributions to the ethane budget [*Rudolph*, 1995].

For methanol, large uncertainties remain on its atmospheric budget and many studies are dedicated to the quantification of each emission contribution [*Galbally and Kirstine*, 2002; *Tie et al.*, 2003; *von Kuhlmann*, 2003; *Jacob*, 2005; *Millet et al.*, 2008]. Overall, plant growth is the largest source of methanol with a contribution to its emissions from 60 to 85 % [*Galbally and Kirstine*, 2002; *Jacob*, 2005]. Methanol atmospheric production represents up to 15–23% of its sources [*Madronich and Calvert*, 1990; *Tyndall et*

al., 2001]. Indeed, CH_3OH is formed from methylperoxy radicals (CH_3O_2) in the atmosphere according to the following equations:

$$CH_3O_2 + CH_3O_2 \rightarrow CH_3OH + CH_2O + O_2 \quad (2.1)$$

$$CH_3O_2 + RO_2 \rightarrow CH_3OH + R'CHO + O_2 \quad (2.2)$$

The latter reactions occur at a rate of 85/15 % respectively for (2.1)/(2.2). RO_2 is produced from biogenic isoprene (C_5H_8) confined to the continental boundary layer while in the remote atmosphere CH_3O_2 is coming from the oxidation of methane and to a lesser extent of ethane [*Jacob*, 2005]. Other sources of methanol are plant matter decaying [9 %; *Warneke et al.*, 1999; *Millet et al.*, 2008], biomass burning and biofuels combustion [6 %; *Jacob*, 2005; *Dufour et al.*, 2006; *Paton-Walsh et al.*, 2008], fossil fuel combustion, vehicular emissions, solvents and industrial activities [3 %; *Galbally and Kirstine*, 2002].

In the troposphere, where they are the most abundant, the main sink of those three gases is the oxidation by hydroxyl radicals [see next section for chemistry; *Aikin et al.*, 1982; *Jiménez et al.*, 2003; *Chen*, 2005]. In addition, in the stratosphere, reaction with chlorine atoms dominates for both methane and ethane [*Aikin et al.*, 1982; *Chen*, 2005]. For methane, other sinks include consumption by soil bacteria at the surface, by reaction with chlorine atoms in the marine boundary layer, and by reaction with $O(^1D)$, OH, and by photodissociation in the stratosphere [*Chen*, 2005]. Finally, other sinks for methanol are deposition to land through uptake microbial and foliar by vegetation [26 %, *Jacob*, 2005], wet deposition through scavenging of water-soluble methanol by convective updrafts, convective anvils or large scale precipitation [6 %, *Liu et al.*, 2001], uptake within the ocean mixed layer [5 %, from 0 to 50 m, *Millet et al.*, 2008], and heterogeneous oxidation by OH in aerosols and clouds [1 %, *Jacob*, 2005].

2.2. Chemistry

In the troposphere, methane, ethane and methanol's respective chemistry are closely connected and play an important role in the overall tropospheric chemistry since the three of them influence the oxidizing capacity of the atmosphere through reaction with the hydroxyl radical. Figure 2.2 illustrates the main reactional pathway of the oxidation of those three compounds in the troposphere by OH.

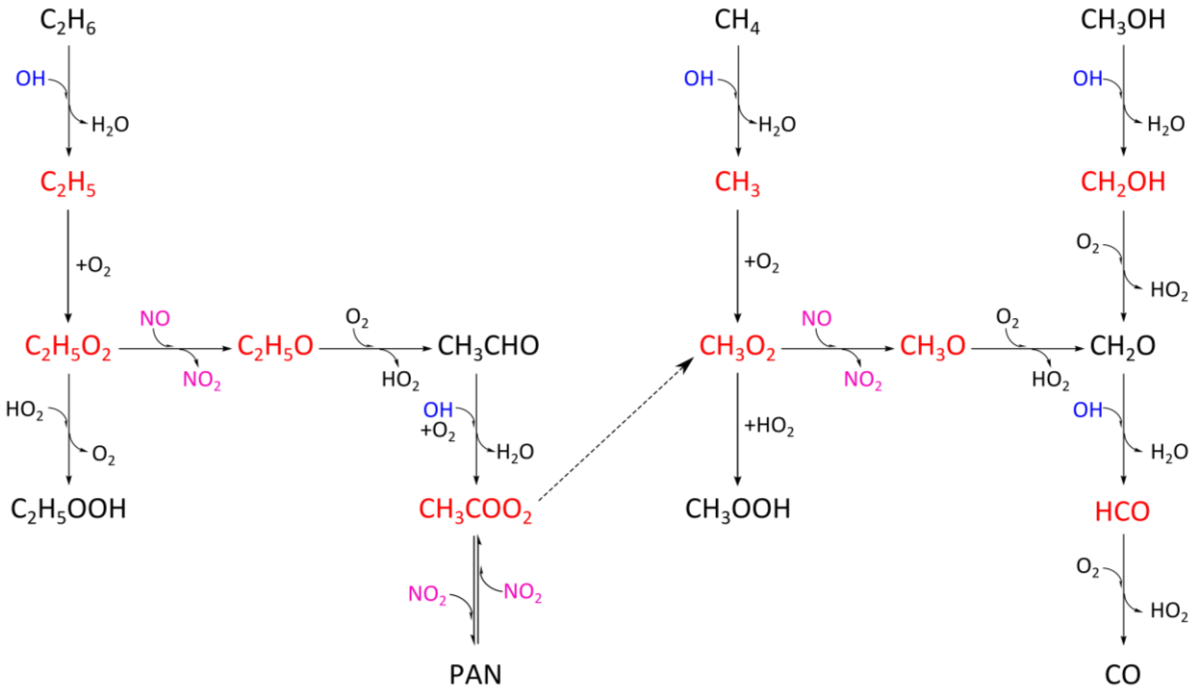

Figure 2.2: Tropospheric chemistry of methane, ethane and methanol. Radicals are shown in red while stable molecules are in black.

While methane, ethane and methanol are chemically quite inert in the atmosphere, they do react with atomic species and molecular radicals which in the troposphere consists mainly of OH. Oxidation of ethane by OH leads to the formation of unstable ethyl radical (C_2H_5) that in turn will react with dioxygen to form ethylperoxy radicals ($C_2H_5O_2$). The reaction between ethyl radicals and dioxygen may also lead to the formation of ethylene (C_2H_4). However, it has been measured that for atmospheric conditions, the interaction of C_2H_5 with O_2 to form $C_2H_5O_2$ radicals is by far the dominant pathway [99 %, *Kaiser et al.*, 1990; *Miller et al.*, 2000; Equation II.A4.88 in *Atkinson et al.*, 2006].

The fate of $C_2H_5O_2$ radicals depends on the local availability of nitrogen monoxide (NO) as illustrated in Figure 2.2. If insufficient NO is available then $C_2H_5O_2$ will react with hydroperoxyl radicals (HO_2) to form the relatively unreactive ethyl hydroperoxide (C_2H_5OOH). On the contrary, if sufficient NO is available (displayed in pink in Figure 2.2), then a rapid reaction sequence follows leading to the recycling of the OH radicals and contributing to the formation of tropospheric ozone by recycling the NO to NO_2 (see Chapter 1, section 1.4.3):

$$C_2H_5O_2 + NO \rightarrow NO_2 + C_2H_5O \qquad (2.3)$$

$$C_2H_5O + O_2 \rightarrow HO_2 + CH_3CHO \qquad (2.4)$$

$$HO_2 + NO \rightarrow NO_2 + OH \qquad (2.5)$$

During this recycling of OH, acetaldehyde (CH_3CHO) is formed. Acetaldehyde can either be photodissociated (see Figure 2.3) to form methane or methyl radicals (CH_3) depending on the wavelength of the photodissociation or be oxidized by hydroxyl radicals to form peroxyacetyl radicals (CH_3COO_2).

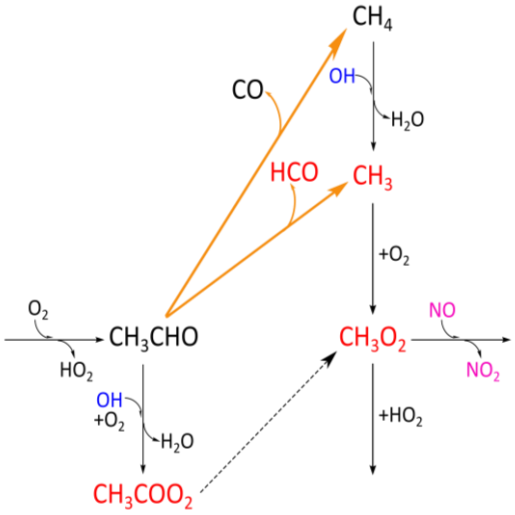

Figure 2.3: Photodissociation of acetaldehyde.

Peroxyacetyl radicals have many pathways of depletion. Its first pathway leads to the formation of peroxyacetic nitric anhydride ($CHCOO_2NO_2$), also called, peroxyacetyl nitrate (PAN, see Figure 2.4) which is produced reversibly by reaction of CH_3COO_2 with NO_2:

$$CH_3COO_2 + NO_2 + M \rightarrow PAN + M \qquad (2.6)$$

where M is a third body (typically N_2 or O_2). It is worth mentioning that PAN's dominant role in the atmosphere is that it acts as an organic reservoir for NO_x [*Roberts et al.*, 1995; *Bertram et al.*, 2013] and thus impacts the production of tropospheric ozone and the hydroxyl radical [*Singh and Hanst*, 1981].

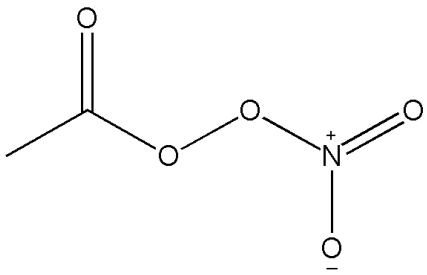

Figure 2.4. PAN or peroxyacetyl nitrate or peroxyacetic nitric anhydride.

As detailed in *Tyndall et al.* [2001], CH_3COO_2 can also form the methylperoxy radical (CH_3O_2) involving a complex series of reactions via many pathways and through the $CH_3C(O)O$ intermediate. The main pathways for the formation of this intermediate are:

$$CH_3COO_2 + NO \rightarrow CH_3C(O)O + NO_2 \quad (2.7)$$

$$CH_3COO_2 + CH_3COO_2 \rightarrow 2\ CH_3C(O)O + O_2 \quad (2.8)$$

This intermediate will then decompose into CH_3 and CO_2 according to the following equation:

$$CH_3C(O)O + M \rightarrow CH_3 + CO_2 + M \quad (2.9)$$

The methyl radical, CH_3, either formed in the atmosphere by OH oxidation of methane (see Figure 2.2), by the photodissociation of acetaldehyde (see Figure 2.3) or by decomposition of peroxyacetyl radicals through a complex series of reactions (2.7, 2.8 and 2.9), will react with O_2 to form methylperoxy radicals, CH_3O_2. The decomposition of CH_3O_2 will lead to the formation of methyl hydroperoxyde (CH_3OOH) if no sufficient NO is available while under "high NO" conditions, it will lead to the formation of the radical CH_3O and contribute to the recycling of NO_2 and thus to the formation of tropospheric ozone. It should also be mentioned that the recycling of methanol through atmospheric production (see 2.1 and 2.2) consumes less than 10 % of the CH_3O_2 atmospheric reservoir sink [*Jacob*, 2005].

The oxidation of methanol by OH leads to the formation of either CH_3O or hydroxymethyl radicals (CH_2OH) in addition to water vapour (see Figure 2.5). However, it has been reported by *Atkinson et al.* [2006] based on the thermochemistry, that the formation of the latter is prevailing in the atmosphere.

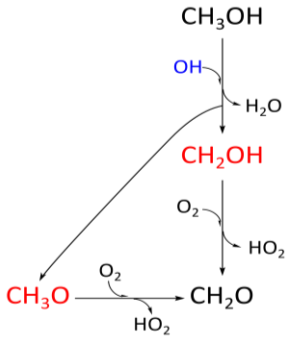

Figure 2.5: Oxidation of methanol by OH.

The CH_3O either formed by oxidation of methanol or from methylperoxy radicals, will react with dioxygen to form formaldehyde (CH_2O). Formaldehyde is the most abundant organic carbonyl compound in the remote troposphere and is directly emitted in a small fraction from biogenic (e.g., vegetation), pyrogenic (mainly biomass burning) and anthropogenic (e.g., industrial emissions) sources [*Franco et al.*, 2015 and references therein]. However, background levels of formaldehyde are built up by oxidation of long-lived VOCs such as methane according to the pathways described in this section.

Finally, formaldehyde is also oxidized by OH to form formyl radicals that will in turn react with dioxygen to form carbon monoxide (CO). Carbon monoxide, with a moderately long tropospheric lifetime of 52 days [*Hough*, 1991], is an important indicator of tropospheric pollution and transport since it is emitted primarily by anthropogenic sources [*Logan et al.*, 1981; *Rudolph*, 1995]. It has been reported by *Duncan et al.* [2007] that as a consequence, CH_3OH is considered as a source of CO with a yield close to 1.

In the same way methane, ethane and methanol are oxidized by OH in the troposphere, they react with chlorine atoms in the stratosphere and then proceed through the same reaction pathway [*Atkinson et al.*, 2006]. In addition, methane reacts with chlorine atoms in the marine boundary layer, and by reaction with $O(^1D)$, OH, and by photodissociation in the stratosphere [*Chen*, 2005]. The oxidation of methane by OH leads to the formation of water vapour, making it a great contributor to the stratospheric water vapour budget, an important driver of decadal global surface climate change [*Solomon et al.*, 2010].

In brief, methane, ethane and methanol share a common tropospheric sink: the oxidation by the radical OH. The chemical pathways described in Figure 2.1 illustrates how their oxidation leads to the formation of PAN, a thermally unstable reservoir for nitrogen oxide radicals, to the recycling of NO_2 thus contributing to the ozone production and by the formation of carbon monoxide through formaldehyde, impacting the air quality of the atmosphere.

2.3. Methane and two of its derivative in the atmosphere

2.3.1. Vertical distribution

All three compounds vertical distribution for the Northern mid-latitudes are illustrated in Figure 2.6. Since methane, ethane and methanol main sources are located at the surface, we find quite good mixing in the first layers of their respective profiles especially for methanol and methane. The longer their atmospheric lifetime, the higher they move to upper levels such as the upper-troposphere lower-stratosphere (UTLS) to reach the stratosphere. Indeed, methanol, with a lifetime of 4.7 to 12 days, is well-mixed until around 10 km of altitude and then rapidly drops to a tenth of its mixing ratio value. On the other side, the vertical distribution of ethane with a lifetime of around 2 months, shows a slower drop of its mixing ratio to reach a negligible value close to zero up until 20 km. Finally, methane, with a lifetime of around 8-10 years, shows a mixing ratio profile that remains constant below the tropopause. Indeed, due to its relatively long atmospheric lifetime in addition to its main sources located at the surface, it is well-mixed in the troposphere before reaching the stratosphere where it will react with $O(^1D)$ or OH or be photodissociated (see previous section).

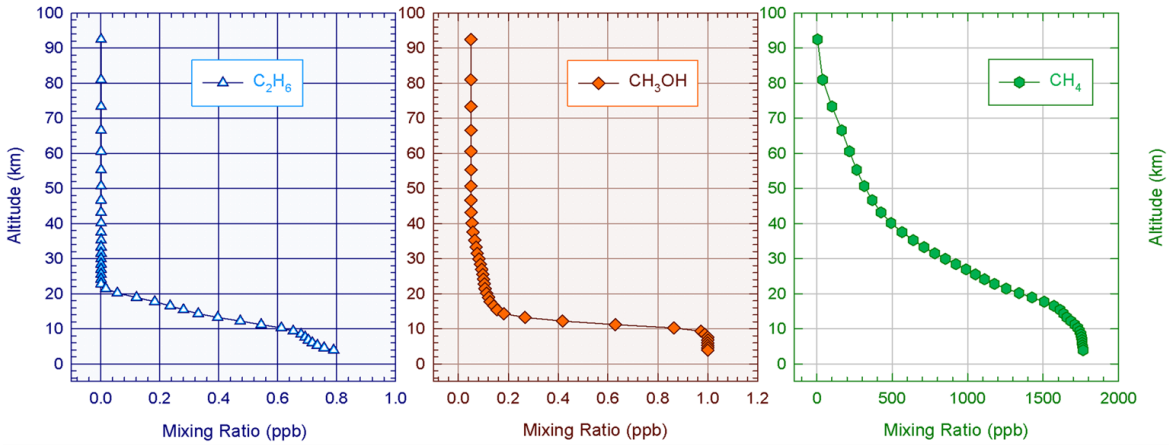

Figure 2.6. Vertical distribution of ethane, methanol and methane expressed in mixing ratio for the Northern mid-latitude.

2.3.2. Seasonal cycles

Methane, ethane and methanol show specific seasonal variations. In the Northern hemisphere, minimum concentrations of methane occur during summer (June-August), rapidly rising to maximum values during fall [September-November, *Khalil and Rasmussen*, 1983] while in the Southern hemisphere, the contrary is observed with minimum concentrations in fall. The methane seasonal cycle is in agreement with the seasonal cycle of atmospheric OH concentrations which is enhanced during summer [*Khalil and Rasmussen*, 1983].

Regarding ethane, its ethane seasonal cycle is characterized by a maximum in March–April and a minimum in August–September. Since fossil fuel production is the main source of C_2H_6 emissions [*Xiao et al.*, 2008] and does not present a particular seasonal cycle during the year [*Pozzer et al.*, 2010], the strong seasonal cycle of C_2H_6 burden is primarily driven by the photo chemical oxidation rate by OH radicals [*Schmidt et al.*, 1991; *Simpson et al.*, 2012].

Finally, in the Northern Hemisphere the strong seasonal modulation of methanol is characterised by minimum values and variability in December to February and maximum columns in June–July [*Bader et al.*, 2014] which can be explained by the primordial role that plant growth plays in the methanol budget. Indeed, plant growth and the production of methanol associated to it is more active during summer than during winter [*Galbally and Kirstine*, 2002; *Jacob*, 2005].

2.3.3. Trends

Figure 2.7 shows the times series of daily mean methanol total columns above Jungfraujoch. We evaluated the trend of methanol total columns over the 1995–2012 time period and found a yearly negative trend of (-1.34 ± 2.71) x 10^{13} molecules.cm^{-2}.year^{-1} or -0.18 ± 0.36 %.year^{-1} (2-σ), i.e. a non-significant trend at this level of confidence, which is consistent with the trend computed by [*Rinsland et al.*, 2009]. Since no significant trend of methanol total columns over the 1995–2012 time period has been identified, the chapter 4 of this work will be dedicated to the analysis of the strong seasonal modulation of methanol and

to its diurnal variation, involving comparisons with other measurements. The optimized retrieval strategy described by *Bader et al.* [2014] in chapter 4 allows us to derive two partial columns, i.e. a lower-tropospheric (LT, 3.58–7.18 km) and an upper tropospheric–lower stratospheric one (UTLS, 7.18−14.84 km). Since these partial column time series do not show any significant trend either, the Chapter 4 is also focused on the seasonal cycle analysis of both partial columns.

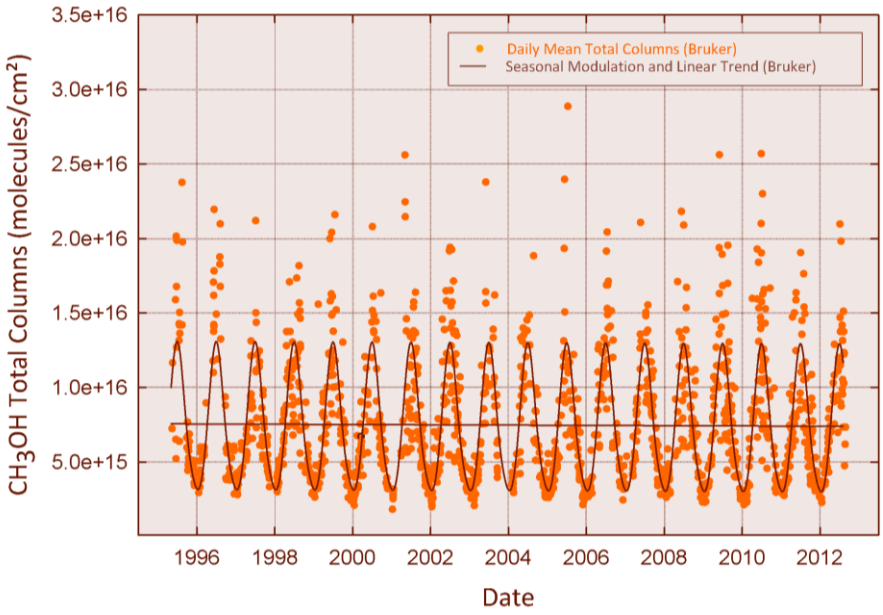

Figure 2.7. Methanol total column above Jungfraujoch time series. Orange circles are daily mean total columns and brown lines show the seasonal modulation and linear trend associated to it.

As to ethane, analysis of the 1994–2008 timespan reveals a regular decrease of the C_2H_6 amounts above the Jungfraujoch station by - 0.92 ± 0.18 %.year^{-1} relative to 1995.0 [*Franco et al.*, 2015a]. This negative trend is consistent with measurements and corresponding trends of atmospheric C_2H_6 burden presented in [*Aydin et al.*, 2011; *Simpson et al.*, 2012], both studies attributed the decline of global C_2H_6 emissions from the mid-1980s to reduced fugitive emissions from fossil fuel sources in Northern Hemisphere rather than a decrease in biomass burning and biofuel use (the other major sources of C_2H_6). However, our study reported in chapter 5 reports recent and unexpected ethane increase since 2009 above the Swiss Alps.

Finally, methane concentrations have increased by 260% since the beginning of the industrialization to reach 1824 pbb in 2013 [*World Meteorological Organization*, 2014]. From the 1980s until the beginning of the 1990s, atmospheric methane was significantly on the rise by about 13 parts ppb per year [*Nisbet et al.*, 2014], then stabilized during 1999-2006 [*Dlugokencky*, 2003] to rise again afterwards [*Nisbet et al.*, 2014]. The source (or sink) attribution of this latter increase is still questioned [*Rigby et al.*, 2008; *Dlugokencky et al.*, 2009; *Bousquet et al.*, 2011; *Sussmann et al.*, 2012]. In the last chapter of this work, we provide analysis of the GEOS-Chem Chemical Transport Model tagged simulation that accounts for the contribution of each emission source and one sink in the total CH_4 simulated based on emissions inventories and transport in parallel with methane changes analysis since 2005 from FTIR observations recorded at ten NDACC stations in order to address what source(s) or sink is responsible for this renewed increase.

Chapter 3 – Atmospheric composition monitoring

Now that the first chapter has established the physical principles allowing us to identify and quantify infrared active atmospheric constituents from infrared solar observations, a description of the instrumentation employed for the recording of observations as presented in the second part of this work is given. This chapter is therefore dedicated to the description of how from FTIR solar observations we retrieve amounts of atmospheric constituents and how those concentrations are characterized.

First, the operating principle of a ground-based Fourier Transform InfraRed spectrometer is illustrated in Figure 3.1. Once the radiation has passed through the atmosphere, it is collected by a coelostat and is sent to a Michelson Interferometer via a series of mirrors. This interferometer consists essentially of a mobile and a fixed mirror, as well as of a beamsplitter. The two beams recombine after their respective path and the signal is recorded at the detector in several discrete positions of the continuously moving mirror to form an interferogram. The spectrum is then built from the interferogram with a Fourier Transform and expresses an intensity of transmitted light, i.e. a transmittance, depending on the wavelength in wavenumber unit, cm^{-1}. Therefore with this technique, we do not measure directly the abundance of atmospheric constituents. In order to retrieve the number of molecules which have absorbed infrared radiation along the path of the light i.e. a total column, we therefore have to perform what is called an "inversion".

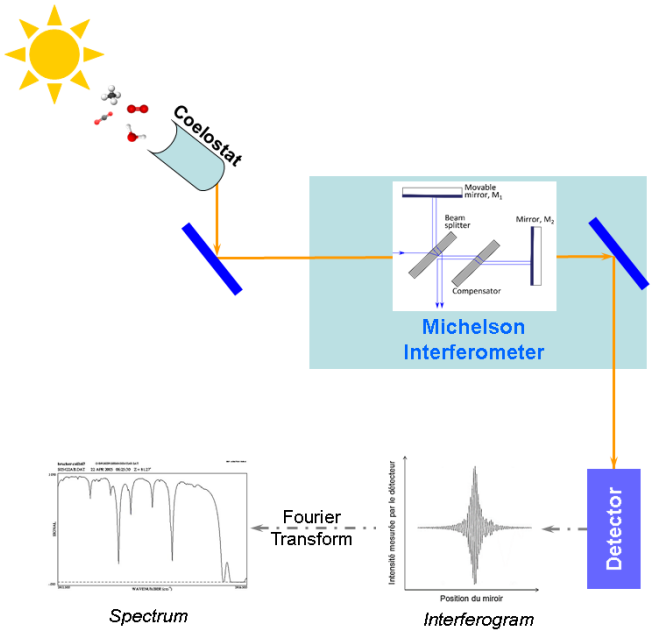

Figure 3.1. Operating principle of a Fourier Transform Spectrometer

The first section of this chapter will depict a typical Michelson interferometer along with the description of the filters and detectors routinely used. The second section will describe how an inversion is performed thanks to the SFIT-2 algorithm, what the necessary input parameters are and how the inversion can be constrained. The third section will describe the method employed for the characterization of the results retrieved from the observations in terms of uncertainties. The fourth section is dedicated to the

description of the Jungfraujoch station, affiliated to the Network for Detection of Atmospheric Composition Change (NDACC, www.ndacc.org, see section 3.5.1), its history, what kind of information this exceptional site provides us on the atmosphere state and its objectives for the atmospheric composition monitoring. Finally, the fifth section provides a description of other datasets dedicated to the atmospheric composition monitoring and exploited in the second part of this work such as satellite observations, in situ measurements and model simulation.

3.1. Fourier Transform Spectrometer

A Fourier Transform spectrometer (FTS) is based on a Michelson type interferometer, illustrated in Figure 3.2. It essentially consists of two mirrors, a movable one (M_1) and a fixed one (M_2), and a beam-splitter. The incoming light hits the beam-splitter where it is divided into two beams of equal intensities by partial reflection and transmission. The compensator ensures both beams pass through the same thickness of material. At the Jungfraujoch, the correction is realized thanks to a low resolution measurement around the zero path difference in order to evaluate the shift induced by the thickness of the beam-splitter. Both beams recombine after having covered their respective path to form an interferogram. The recorded signal is therefore measured at many discrete positions of the moving mirror. This recorded signal is maximum for the zero optical path difference (ZPD) leading to a maximum constructive interference, i.e. when the position of the moving mirror corresponds to equal optical path lengths for both the transmitted and reflected beams. The spectrum is reconstructed using a Fourier transform of the interferogram.

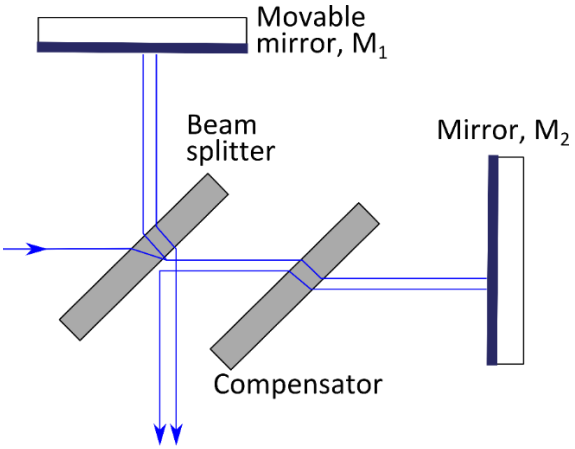

Figure 3.2. Michelson Interferometer.

The FTS installed at the Jungfraujoch station (see section 3.4) is equipped with a potassium bromide (KBr) beam-splitter and two cooled detectors, i.e. a Mercury-Cadmium-Tellurium (HgCdTe or MCT) and an Indium-Antimonide (InSb) covering the 650 to 4500 cm^{-1} region of the electromagnetic spectrum. They achieve resolution, defined as the reciprocal of twice the maximum Optical Path Difference (OPD), which ranges between 0.00285 and 0.006cm^{-1} respectively corresponding to an OPD of 175.6 and 82 cm. Five optical filters are routinely and consecutively used in order to maximize the signal-to-noise ratio (see color codes in Figure 3.3).

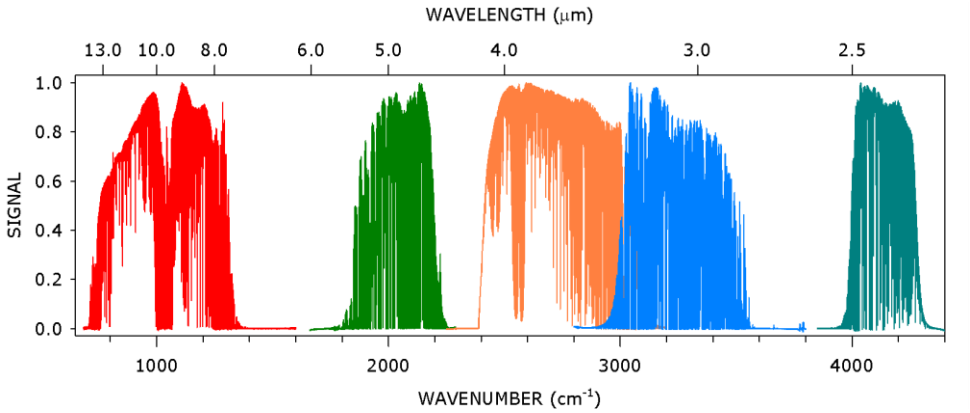

Figure 3.3. Optical filters. The regions covered by the filters are respectively covering the 350-1600 cm^{-1} (in red), 1660-2250 cm^{-1} (in green), 2200-3300 cm^{-1} (in orange), 2800-3800 cm^{-1} (in blue), 3850-4400 cm^{-1} (in cyan) ranges. Mahieu et al., 2015.

3.2. Inversion

3.2.1 The SFIT algorithm

The algorithm has been specifically developed by C. P. Rinsland (National Aeronautics and Space Administration, NASA, Langley Research Center, Hampton, Virginia, USA), with support from B. J. Connor (National Institute of Water and Atmospheric Research, NIWA, Lauder, New Zealand), for the inversion of the vertical mixing ratio profiles of atmospheric gases from high resolution ground-based infrared solar absorption spectra recorded with FTIR instruments. The forward model in SFIT-2 has been previously described by *Pougatchev et al.*, 1995 and *Rinsland et al.*, 1998.

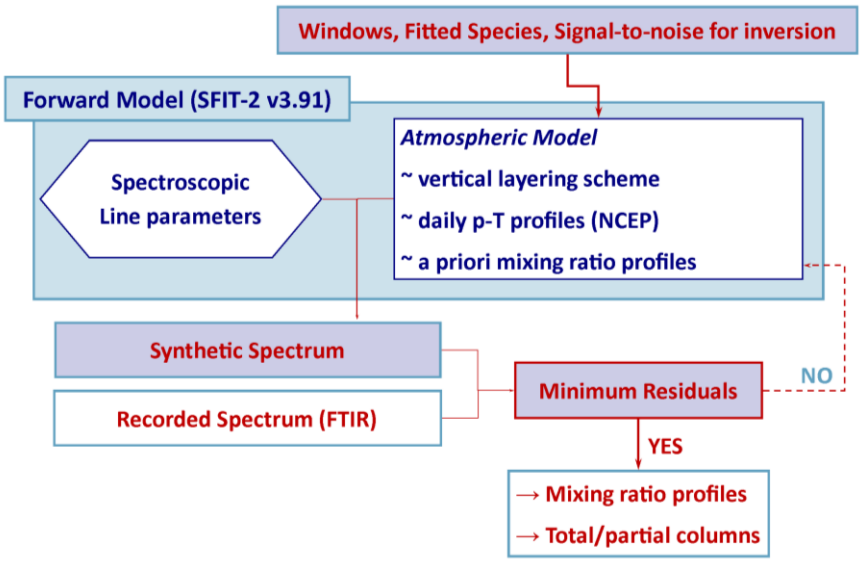

Figure 3.4. Operating principle of the SFIT-2 algorithm.

In this work, SFIT-2 v3.91 is used to retrieve total vertical columns of methane, its operating principle is described in Figure 3.4. SFIT consists in a forward model that comprises (i) a spectroscopic database characterizing the position and intensity of the targeted lines and (ii) an atmospheric model associated with a vertical layering scheme accounting for the daily pressure-temperature profiles and with a priori mixing ratio profiles to be adjusted. This model will compute a synthetic spectrum on a domain of wavelength of up to several tenth of wavenumber that contains specific absorption lines of the target gas. This domain is named a window. Through an iterative process the mixing ratio profiles will be adjusted (as well as adjustment of other parameters associated with the forward model) until the convergence to a minimum of the residuals, i.e. the difference between the synthetic and the recorded spectra.

3.2.1.1. Input parameters

All input parameters necessary for the retrieval of total columns from FTIR solar observations are described in the following paragraphs.

a- Spectroscopic line parameters

In order for SFIT-2 to compute the transmittance associated to a specific spectral line in the atmosphere, the algorithm needs information on the absorption coefficient as a function of wavenumber for each line. The four essential parameters for each line, are the frequency on which the absorption is centered, the intensity per absorbing molecule, the line width parameter and the lower energy state [*McClatchey et al.*, 1973]. Those line-by-line spectroscopic data are read from a compilation of spectrometric parameters, such as HITRAN (HIgh-resolution TRANsmission molecular absorption database, https://www.cfa.harvard.edu/hitran/). The HITRAN compilation includes the official HITRAN line parameters [*Rothman et al.*, 2013 and references therein], infrared cross-sections, UV line-by-line parameters and cross-sections, aerosol refractive indices, and documentation. The spectroscopic parameters available in the HITRAN linelist are essentially coming from laboratory works. New versions of HITRAN are published every four years while updates or corrections are made available for specific gases on a more frequent basis. Currently, the latest version, HITRAN-2012 [*Rothman et al.*, 2013], contains 7,400,447 spectral lines for 47 different molecules, incorporating 120 isotopologues.

Nevertheless, as outlined in *Rothman et al.* [1987], no line parameters are available for several atmospheric molecules with significant infrared features. This category includes more complicated molecules, for which line-by-line parameters are available only in specific spectral region. In this case, the HITRAN database provides a separate file of high resolution cross-sections. Until further information becomes available, the cross sections can either be incorporated directly into a line-by-line calculation as additive spectral values or be built from a simulation of the spectra by generating artificial line parameters. It has been emphasized by *Rothman et al.* [1987] that, while the accuracy of the cross-sectional method is limited (especially for strong absorptions), omitting them in spectral regions where no line parameters are available leads to much larger errors in the interpretation of line-by-line simulations of atmospheric spectra.

Since SFIT-2 does not allow direct use of cross-section parameters, they need to be converted into pseudolines. To this end, laboratory cross-section spectra are interpolated (or extrapolated) in temperature and pressure [*Toon et al.*, 2015] by performing spectral fits to laboratory transmittance spectra. The lab transmittance spectra are re-created using the temperature- and pressure-dependent cross-sections available. Its objective is not to supplant proper quantum-mechanically-based linelists but to provide spectroscopic information on spectral bands that still remain unresolved or unidentified, to this day.

In addition, as mentioned in *Hase et al.* [2006], since the solar spectrum in the mid-infrared spectral region is far from a smooth blackbody spectrum we need to include a model of the solar absorption features in SFIT-2. To this end, the solar line compilation provided by F. Hase [Karlsruhe Institute of Technology, Institute of Meteorology and Climate Research, Karlsruhe, Germany; *Hase et al.*, 2006] has been assumed for the solar absorptions.

b- Pressure-Temperature profiles

For our retrievals, we have adopted pressure (p) and temperature (T) profiles as provided by the National Centers for Environmental Prediction (NCEP; Washington, D.C.; http://www.ncep.noaa.gov) from the National Oceanic and Atmospheric Administration (NOAA) and made available to the NDACC principal investigators. The p-T profiles are specifically computed for each NDACC station on a daily basis noon time. NCEP meteorological data analyses are based upon a rawinsonde onboard the NOAA polar orbiting operational satellites that collect atmospheric parameters and measures wind speed and direction to transmit them by radio to a ground receiver. Each satellite contains three multichannel instruments, namely the High-resolution Infrared Sounder (HIRS), the Microwave Sounding Unit (MSU) and the Stratospheric Sounding Unit (SSU), which altogether form the Television infrared observation satellite (TIROS) Operational Vertical Sounder (TOVS).

In practice, pressure and temperature profiles provided by NCEP are interpolated on the altitude levels defined in the vertical layering scheme adopted in our retrievals. The vertical layering consists in layers of increasing depths with increasing altitude and adapted to the altitude of each station up to ~100 km. In the retrieval process, each layer is considered homogenous in terms of atmospheric pressure, temperature and volume mixing ratio of the target and interfering gases. For the Jungfraujoch station, we use a 39-levels altitude grid. Since the NCEP datasets also include the uncertainties on the temperature profiles, the impact of temperature profile uncertainties on our retrieved total columns has been included in our error budget (see section 3.3).

c- A priori profiles, covariance matrix and inter-layer correlation

In order to produce a synthetic spectrum, we need to define an a priori state that will account for the vertical distribution of the target and interfering gases considered for the retrieval and that will be adjusted by SFIT-2 to minimize residuals. To this end, we select profiles that represent at best the mean atmospheric situations prevailing above the considered station. Ideally, these vertical profiles represent a climatology of the considered gas which is built from actual observations such as satellite observations

and are expressed in mixing ratio units (as defined in Chapter 1) in function of the altitude, the vertical reference in SFIT-2. However, while satellite observations may provide better vertical resolution on the vertical distribution depending on their respective line of sight (e.g. ACE-FTS' limb viewing provides better vertical resolution than FTIR and the nadir-viewing Infrared Atmospheric Sounding Interferometer, IASI), they have their limitations in the altitude range they are covering. In addition, their temporal coverage might not provide enough information in order for us to build a representative climatology.

In order to compensate the lack of vertical and/or temporal information provided by satellite measurements, simulations from Chemical Transport Model (CTM) are used. In addition to a better vertical resolution, they present better availability of data since they only depend on best estimates of the vertical distribution of the studied gas from best emission inventories.

In practice, we adopt a priori profiles generated within the NDACC from simulation of the Whole Atmosphere Community Climate Model, [WACCM, *Chang et al.*, 2008]. However, when developing an optimized retrieval strategy for a specific species and/or station, in order to avoid that SFIT-2 produces oscillating profiles responsible for ungeophysical negative mixing ratio profiles, it may be required to combine information from satellite observations as well as from CTM simulation depending on the case studied. This way, we optimize the representativeness of the selected a priori vertical distribution. For example, as illustrated in Figure 3.5, in order to build a priori vertical distribution of ethane (C_2H_6), we first combined and tested a number of datasets available including satellite observations from the Atmospheric Chemistry Experiment-Fourier Transform Spectrometer (ACE-FTS), CTMs simulations and in situ measurements, for the purpose of the optimization of a retrieval strategy for C_2H_6 for the Jungfraujoch station (see Chapter 5).

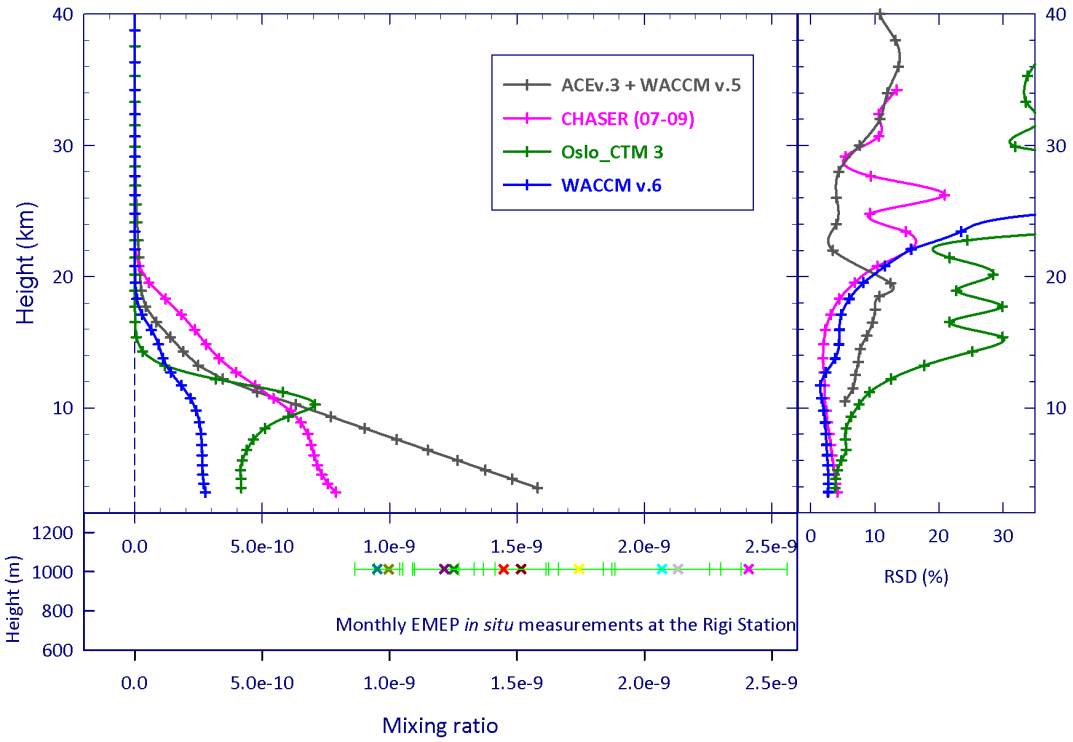

Figure 3.5. Vertical distribution of ethane above the Jungfraujoch station (left panel) and their associated relative standard deviation (right panel). The bottom panel shows EMEP [European Monitoring and Evaluation Programme, http://www.emep.int/] in situ gas chromatography surface measurements at the Rigi station (47.07 °N, 8.45 °E, 1031 m a.s.l., at a distance of 68 km from the Jungfraujoch station). Pink crosses is the a priori profile issued from the CHASER 3D Chemical Transport Model [Sudo, 2002] developed at the Center for Climate System Research, University of Tokyo/National Institute for Environmental Studies (NIES). Chemical Transport Model v.2 and v.3 from the Center for International Climate and Environmental Research Oslo (CICERO, Oslo, Norway) and the university of Oslo [Berntsen and Isaksen, 1997] are plotted in dark and light green crosses, respectively. The grey crosses are a zonal mean (for the 41-51°N latitude band) of 771 occultations recorded by the ACE-FTS instrument between the 2nd of November in 2004 and the 8th of February in 2011 extending from 8.5 to 20 km. The profile extension down to the Jungfraujoch altitude, 3.58 km, is based on EMEP in situ measurements while the upper extension to 100 km is based on the WACCM model climatology.

From Figure 3.5, we see that all dataset available provide a wide range of mixing ratio vertical distribution for ethane. Indeed, the version 6 of the WACCM model provides the lowest mixing ratio with 277 ppt while with 1590 ppt the version 5 of the same model is the highest mixing ratio value for ethane at the altitude of Jungfraujoch. Moreover, the variability of ethane associated to all model-based vertical profiles show a wide range of values more specifically around the tropopause altitude. The challenge is therefore to choose the vertical a priori distribution that will prevent SFIT to produce oscillating retrieved profiles while maximizing the vertical sensitivity and information content.

In addition to the a priori vertical distribution of the interfering gases considered in the retrieval, a covariance matrix, accounting for the relative standard deviation associated to the a priori profile needs to be specified. This covariance matrix will then establish a statistical value range within which the SFTI-2 algorithm is allowed to adjust the vertical distribution of the target gases. Ideally, the a priori full

covariance matrix, $\boldsymbol{S}_a$, should express the natural variability of the target gas. However, because of a lack of data, a full matrix is often not available and simplest matrices, such as pure diagonal or ad hoc matrices, are used. Extra-diagonal elements of the $\boldsymbol{S}_a$ matrix expresses the fact that an inter-layer correlation (ILC) exists between the concentrations of the target gas at different altitudes. For example, the SFIT-2 algorithm allows us to introduce such extra-diagonal elements by defining a Gaussian or an exponential inter-correlation with selected length. The first case is the most commonly used. However, while a covariance matrix built from climatological data is more realistic, we may need to palliate a lack of data to construct a reasonable a priori through a retrieval constraint.

d- Forward model parameters

It may be required for an optimized retrieval to adjust additional parameters that are not necessarily perfectly known by the user. For example, parameters such as the wavenumber shift or background curve parameters (e.g. slope and curvature) are comprised in the forward model parameters. In addition, SFIT-2 allows for the use of an effective apodisation function that expresses the stability of the mirror while it moves assessing for the good alignment of the instrument through a recording. The effective apodisation function can either be defined as a polynomial function of degree N, as a Fourier series of order N or as any other tabulated function. The effective apodisation parameter (EAP) gives the value of the effective apodisation function at the maximum OPD. Consequently, an EAP value close to 1.0 indicates a well-aligned instrument. Therefore, the retrieval of the EAP, as allowed by SFIT-2, ads to the list of adjusted model parameters. As an example, for the retrieval of methanol in chapter 4, the EAP has been adjusted.

3.2.1.2. Retrieval and constraints

As described in *Rodgers*, 2000 and summarized in *Sussmann et al.*, 2007, the inverse problem consists in finding the best estimator of the true target profile, through the forward model F that maps from the true state into the measurement and knowing the a priori information and the measurement vector $\boldsymbol{y}$. The forward model is defined as:

$$F(\boldsymbol{x}, \boldsymbol{b}) = \boldsymbol{y} + \boldsymbol{\varepsilon} - \Delta \boldsymbol{f} \qquad (3.1)$$

where $\boldsymbol{b}$ is the forward model parameters, $\boldsymbol{\varepsilon}$ is the measurement noise and $\Delta\boldsymbol{f}$ the error in the forward model relative to physics. On the other hand, the true physical relation between the measurement vector $\boldsymbol{y}$ and the true target profile, $\boldsymbol{x}$ is described by the forward function f:

$$\boldsymbol{y} = f(\boldsymbol{x}, \boldsymbol{b}, \boldsymbol{b}') + \boldsymbol{\varepsilon} \qquad (3.2)$$

where $\boldsymbol{b}'$represents all forward function parameters which are ignored in the construction of F. For FTIR measurements, the measurement vector $\boldsymbol{y}$ corresponds to an intensity measured in function of the wavelength within the window(s) limits. In addition, the forward model parameters are not always perfectly known by the user, like spectroscopic parameters or parameters related to the instrument.

Since the forward model $\boldsymbol{F}$ is nonlinear, the optimal solution is iteratively reached by use of the Gauss-Newton method starting from the a priori state and until the difference between the measurement and

the calculated state, i.e. the residuals, is minimized. The contribution of the a priori state is then balanced by a regularization term. This regularization term, $\boldsymbol{R} \in \Re^{n \times n}$, a square matrix of dimension n (being the number of layers of the atmospheric model, see 3.2.1.1.) allows us to add information about the shape of the retrieved profile. In the following, we present 3 types of $\boldsymbol{R}$, the simple scaling operation, the optimal estimation [*Rodgers*, 1976] and the Tikhonov regularization [*Tikhonov*, 1963].

a- Simple scaling

When the regularization term is the identity matrix $\boldsymbol{I}$, the retrieved profile is obtained by applying a simple scaling operation to the a priori profile $\boldsymbol{x_a}$. This scaling operation is often applied for lower-resolution spectra or for minor interfering retrieved species.

b- Optimal Estimation Method (OEM)

The OEM is a climatological constraint where $\boldsymbol{R}$ is setup using the relation:

$$\boldsymbol{R} = \boldsymbol{S}_a^{-1} \tag{3.3}$$

where $\boldsymbol{S}_a \in \Re^{n \times n}$ is the a priori covariance matrix. In the ideal case, $\boldsymbol{S}_a$ is a climatological covariance constructed from an ensemble of true profiles covering the full range of possible atmospheric states (see previous section). The optimal estimation method has been used in this work for the retrieval of both methanol and ethane (see the second part of this work).

c- Tikhonov regularization

In the case of the Tikhonov regularization, a smoothing constraint, $\boldsymbol{R}$ is setup using the relation:

$$\boldsymbol{R} = \alpha\, \boldsymbol{L}^T\, \boldsymbol{L} \tag{3.4}$$

where α is the strength of the constraint and $\boldsymbol{L}$ is the constraint operator. For example, the first-order operator $\boldsymbol{L}_1$

$$\boldsymbol{L}_1 = \begin{pmatrix} -1 & 1 & 0 & \cdots & 0 \\ 0 & -1 & 1 & \ddots & \vdots \\ \vdots & \ddots & \ddots & \ddots & 0 \\ 0 & \cdots & 0 & -1 & 1 \end{pmatrix} \in \Re^{n \times (n-1)} \tag{3.5}$$

constrains the shape of the retrieved profile but not its absolute values which are determined by the measurement. The following discussion is restricted to two limiting cases of α values:

- $\alpha \to \infty$ represents an infinitely strong constraint to the profile shape and a zero constraint to the absolute value of the profile scaling factor which is equivalent to a simple profile scaling,

- $\alpha \to 0$ describes a retrieval without any regularization. The retrieval will then provide a perfect fit without any residuals but will show strong ungeophysical profile oscillations.

In between, when using the Tikhonov regularization, the α values can be tuned to target a given Degree of Freedom for Signal (DOFS). For example, it has been established within the NDACC network that the regularization strength of the methane retrieval strategy would be optimized so that the DOFS reaches a mean value of approximately 2 [Sussmann et al., 2011].

The difference between the climatological OEM constraint and the smoothing Tikhonov regularization is that the determination of the absolute values is done through the information that is, for the latter, located in the measurement and not in the constraint. While the climatological constraint is more realistic, since it is based on actual measurements, the smoothing regularization can palliate a lack of data to construct reasonable a priori and help us avoid the appearance of non-geophysical oscillations in the retrieved profiles.

3.2.2. Information content

An effective way to express the ability of the observations to constrain the true values to be retrieved is with the averaging kernel matrix $\boldsymbol{A} = \partial\hat{\boldsymbol{x}}/\partial\boldsymbol{x}$, representing the sensitivity of the retrieved profile $\hat{x}$ to the true profile x. $\boldsymbol{A}$ is the product of the gain matrix $\boldsymbol{G_y} = \partial\hat{\boldsymbol{x}}/\partial\boldsymbol{y}$ and the Jacobian matrix $\boldsymbol{K_x} = \nabla_x F = \partial\boldsymbol{y}/\partial\boldsymbol{x}$ which respectively expresses the sensitivity of the retrieved profile to the measurement and the sensitivity of the observation variables $\boldsymbol{y}$ to the true state $\boldsymbol{x}$:

$$\boldsymbol{A} = \boldsymbol{G_y}\,\boldsymbol{K_x} \qquad (3.6)$$

A simplified way to define the retrieved profile would then, according to [*Jacob*, 2007], be:

$$\hat{\boldsymbol{x}} = \boldsymbol{A}\,\boldsymbol{x} + (\boldsymbol{I_n} - \boldsymbol{A})\boldsymbol{x_a} \qquad (3.7)$$

where I_n is the identity matrix of dimension n. A is a weighting factor for the relative contributions to the retrieval from the true profile versus the a priori profile. The first term of (3.7) represents the contribution of the true state to the solution while the second term illustrates the contribution from the a priori. A perfect observational system would have $\boldsymbol{A} = \boldsymbol{I_n}$ while where $\boldsymbol{A} = 0$, the retrieved profile merges with the a priori profile. Since our observational system is not ideal, the rows and columns of the averaging kernel matrix will represent peaked functions (see Figure 3.6), with the width of the peak being a qualitative measure of the vertical resolution of the observing system [*Rodgers*, 1990]. In the process of optimizing the retrieval strategy, a careful and systematic inspection of the averaging kernels is performed to assess the quality of the retrieval and determine the best strategy.

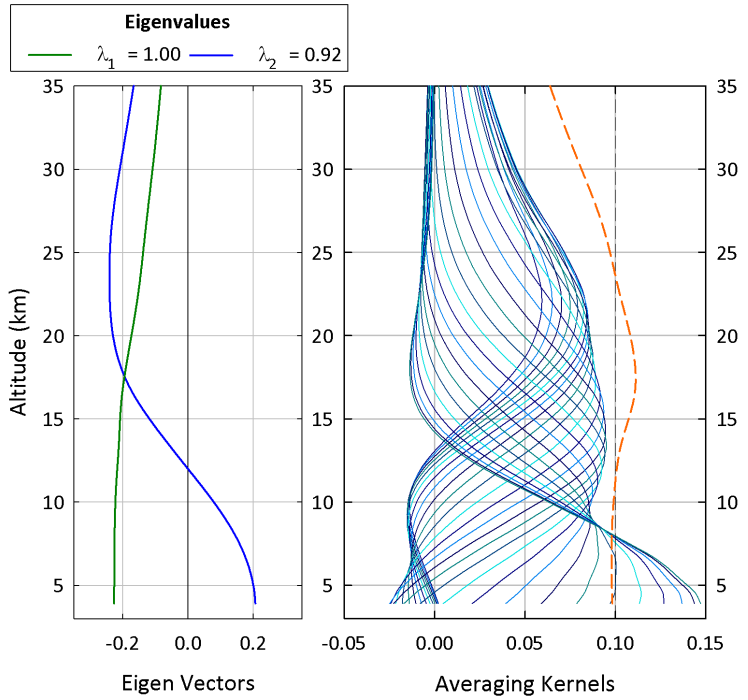

Figure 3.6. Right panel shows first eigenvectors and associated eigenvalues while individual averaging kernels for each layer between the 3.58 and 35.3 km altitude range and total column averaging kernel (orange dashed line; divided by 10 for visibility purpose) characterizing the FTIR retrievals of CH_4 at the Jungfraujoch station. The information content has been established on the basis of all the individual retrieved profiles from fall measurements throughout the 2000–2013 time span.

The trace of the $\boldsymbol{A}$ matrix provides the Degree Of Freedom for Signal (DOFS), i.e. the number of independent pieces of information that can be retrieved from the retrieval also called the information content of a retrieval. On the other side, eigenvectors of $\boldsymbol{A}$ and their associated eigenvalues (see Figure 3.6) allow us to quantify the contribution of the a priori to these independent pieces of information. It implies that eigenvalues equal or close to 1 characterizes a piece of information completely coming from the measurement and thus independent of the a priori. Oppositely, eigenvalues close to zero mainly reproduce the a priori state.

Since it gives information about the observational system, the averaging kernel matrix is also essential to compare two different datasets collected by different observation system used to determine $\boldsymbol{x}$. The difference in sensitivity between two observational systems has to be accounted for before performing any comparison. According to [*Connor et al.*, 1994], one way to proceed is to "degrade" the resolution of the vertical profile $\boldsymbol{x_h}$ characterized by the higher resolution for it to match the lower-resolution vertical profile's resolution in order to obtain a smoothed version $\boldsymbol{x_s}$ of it:

$$\boldsymbol{x_s} = \boldsymbol{x_a} + \boldsymbol{A}\,(\boldsymbol{x_h} - \boldsymbol{x_a}) \qquad (3.8)$$

in which the $\boldsymbol{A}$ matrix is the averaging kernels of the lower resolution observational system. This smoothing allows us to represent the retrieved vertical profile that would be observed by the observational system with the higher resolution if this instrument was set in the same observational

conditions as the lower observational system. This smoothing is mandatory for comparisons between observations and model data since models usually provide results with a greater vertical resolution than a ground-based instrument[1].

3.3. Error budget

In the framework of this work, a method for error analysis [*Bader et al.*, 2014; *Franco et al.*, 2015a, 2015b] has been established for the *Groupe Infrarouge de l'Atmosphère Physique et Solaire* (GIRPAS, Institute of Astrophysics and Geophysics, University of Liège, Belgium, http://girpas.astro.ulg.ac.be,) that combines the classical formulation of error analysis of remote sounding by *Rodgers* [1990] and a perturbation method.

3.3.1. Rodgers formalism

According to *Rodgers* [1990, 2000], the retrieved target profile $\hat{x}$ is related to the true target profile x via the relation:

$$\begin{aligned} \hat{\boldsymbol{x}} - \boldsymbol{x} = (\boldsymbol{A} - \boldsymbol{I})(\boldsymbol{x} - \boldsymbol{x_a}) &\quad \text{smoothing error} \\ + \boldsymbol{G_y K_b}\left(\boldsymbol{b} - \hat{\boldsymbol{b}}\right) &\quad \text{model parameter error} \\ + \boldsymbol{G_y} \Delta f(\boldsymbol{x}, \boldsymbol{b}, \boldsymbol{b'}) &\quad \text{forward model error} \\ + \boldsymbol{G_y}\, \boldsymbol{\varepsilon} &\quad \text{retrieval noise} \end{aligned} \qquad (3.9)$$

where $\boldsymbol{A} = \partial\hat{\boldsymbol{x}}/\partial\boldsymbol{x}$ is the averaging kernel, $\boldsymbol{K_b} = \partial F/\partial\boldsymbol{b}$ expresses the sensitivity of the measurement to the forward model parameters, $\boldsymbol{G_y} = \partial\hat{\boldsymbol{x}}/\partial\boldsymbol{y}$ is the gain matrix representing the sensitivity of the retrieved profile to the measurement, and x_a represents the a priori profile.

First, the smoothing error expresses the uncertainty related to finite vertical resolution of the remote sounding system. Regarding the model parameter error, it accounts for the difference between the true value of the forward model parameters, represented by $\boldsymbol{b}$, and $\hat{\boldsymbol{b}}$, our best estimate of the latter. On the other hand, the forward model error is based on the relation between the forward model F and the forward function f:

$$\Delta f(\boldsymbol{x}, \boldsymbol{b}, \boldsymbol{b'}) = f(\boldsymbol{x}, \boldsymbol{b}, \boldsymbol{b'}) - F(\boldsymbol{x}, \boldsymbol{b}) \qquad (3.10)$$

and expresses the error in the forward model relative to real physics. Finally, measurement noise is described by the error term ε and represents the contribution from the random observational error.

[1] Indeed, this method has been applied in Chapter 6 for the comparison of methane results from FTIR ground-based observations and from the GEOS-Chem Chemical Transport Model.

3.3.2. Perturbation method

The perturbation method developed considers the worst identified case scenario and thus gives a maximum error on the retrieved columns [*Bader et al.*, 2014; *Franco et al.*, 2015a, 2015b]. A non-exhaustive list of the most common parameters considered includes systematic errors, such as the spectroscopic line parameters or the misalignment of the instrument, while uncertainty on the temperature and on the solar pointing is considered to be source of random error. If relevant, other parameters may be included within the error budget. As an example, one can quantify the impact of the choice of the target species a priori profile on the retrieved columns with a perturbation method by fitting a subset of representative spectra with other reliable a priori [*Franco et al.*, 2015a, 2015b].

Errors on the retrieved columns to line intensity uncertainties have been addressed with the *Error_spec* code. *Error_spec* has been specifically developed in the framework of this thesis to produce linelist files with incremented and decremented line intensities (or air-broadening width). To this end, *Error_spec* reads the uncertainty indices corresponding to the lines of the target species as detailed in [Table 5 of *Rothman et al.*, 2005] to assume the maximum errors associated to it. This way, replacing the spectroscopic linelists by the incremented linelists enables us to quantify the impact of the line intensity −or air-broadening width– on the retrieved columns.

In addition, we accounted for an error of 10% on the instrument alignment at the maximum path difference and for a 0.2° error in the solar pointing. The uncertainty on the pressure−temperature profiles is provided by NCEP, i.e. 1.5 °C up to 20 km, 2 °C up to 30 km, 5 °C near 35 km and then progressively increasing up to 9 °C at 50 km. By comparing the two official NDACC algorithms, *Hase et al.* [2004] and *Duchatelet et al.* [2010] have established that the forward model may induce a maximum error of 1% on the retrieved columns for a suite of tropospheric and stratospheric FTIR target gases with either broad or narrow absorption lines.

When water vapor is a strong absorber in the retrieved spectral window(s) and since it shows a great intra-annual variability, the impact of the choice of the a priori state of the water vapor profile may contribute to the random component of the error budget. Indeed, it is of great importance on the error budget as the interfering species (H_2O in this case) need to not be correlated to the target gas. For the Jungfraujoch station, the perturbation corresponds to the variation of the slope of the tropospheric H_2O and HDO a priori mixing ratio profiles simulated by WACCM by a factor 2 [*Duchatelet*, 2011; *Franco et al.*, 2015a, 2015b]. This latter corresponds approximately to the change of slope when taking the 2-σ standard deviation limits around the annually-averaged H_2O mixing ratio profile retrieved above the ISSJ according to [*Sussmann et al.*, 2009].

Through this work, the primary objective was to develop and optimize retrieval strategies for methane, ethane and methanol from solar observations recorded at the Jungfraujoch station. The development and optimization of a retrieval strategy includes: systematic search for and evaluation of absorption lines of the target species and determination of the best combination of spectral windows, spectroscopic linelist (for the target and interfering species), a priori mixing ratio profile, retrieval constraint, among others in

order to limit the interferences, minimize the residuals and maximize the information content and thus maximize the altitude sensitivity range. In addition, the method for error analysis is performed on each available combination of parameters and serves as an indicator for the selection of the best retrieval strategy to be employed.

3.4. The Jungfraujoch station

Results presented in the second part of this work include or are based on ground-based FTIR observations performed at the International Scientific Station of the Jungfraujoch (ISSJ). The ISSJ (Figure 3.7, Swiss Alps, 46.55° N, 7.98° E, 3580 m a.s.l.) is located on the saddle between the Jungfrau (4158m a.s.l.) and the Mönch (4107m a.s.l.) summits. This research station offers unique conditions for infrared solar observations because of weak local pollution (no major industries within 20 km) and very high dryness due to the high-altitude (in dry conditions around two-thirds of water vapor lies below the altitude of 3.6 km) and the presence of the Aletsch Glacier in its immediate vicinity. Indeed, the amount of water vapor (H_2O), a strong absorber in the infrared that often interferes with absorption features of other telluric gases, can be as low as twenty times less than at sea level. The ISSJ allows us to investigate the atmospheric background conditions over central Europe and the mixing of air masses between the planetary boundary layer and the free troposphere [*Reimann*, 2004].

Figure 3.7. The Jungfraujoch station. [*Grindelwald Tourismus*, 2015]

In 1950, M. Migeotte (ULg) started pioneering infrared solar observations at the Jungfraujoch, with a 1 m focal length grating spectrometer reaching resolutions going from 0.12 to 0.40 cm^{-1}. At this stage, resolutions were high enough to record strong features characteristic of minor constituents of the Earth's atmosphere, like methane, CH_4 [*Nielsen and Migeotte*, 1952] or carbon monoxide, CO [*Migeotte and Neven*, 1950]. Eight years later, L. Delbouille and G. Roland installed a more efficient 7.3 m focal length grating spectrometer. This instrument, receiving solar light from a coelostat installed outside on the observatory terrace, was mainly used to systematically record observations for the production of two solar spectrum atlases in the infrared, visible and near-UV [*Delbouille and Roland*, 1963; *Delbouille et al.*, 1973].

Forty years ago, R. Zander (ULg) detected the presence of hydrogen fluoride in the atmosphere from infrared solar spectra recorded by the Liège group with a double-pass 2.5-meter focal length grating instrument during a stratospheric balloon flight over Texas (USA) in 1974 [*Zander*, 1975], demonstrating that the products issued from the photodissociation of CFCs reach the stratosphere. Detection of HF in the atmosphere in addition to the identification of the catalytic cycles involved in stratospheric ozone depletion [*Crutzen*, 1970; *Johnston*, 1971; *Molina and Rowland*, 1974; *Stolarski and Cicerone*, 1974] prompted the ULg scientists to resume their atmospheric-oriented observations at the Jungfraujoch station, to monitor the abundance of gases such as HCl, HF and CH_4.

To this end, in 1976, the Jungfraujoch 7.3 m focal length double-pass spectrometer was equipped with a special grating and a liquid nitrogen-cooled InSb detector for solar observations to be extended in the infrared, out to about 5.4 µm. It achieved spectral resolution of nearly 0.02 cm^{-1} and signal-to-noise ratio of up to 250. Narrow infrared spectral windows encompassing isolated lines of HF, HCl, N_2O, CH_4 and NO_2 have been regularly recorded with this instrument until 1989.

The need for larger signal-to-noise ratios allowing to detect and quantify an increasing number of chemically important trace gases present at very low concentrations required the design, development and adoption of a Fourier Transform Spectrometer [*Roland*, 1965; *Malbrouck*, 1977]. In particular, a Connes-type [*Connes*, 1971] stepping-mode FTIR spectrometer of 1 m optical path difference (ultimate spectral resolution of 0.005 cm^{-1}) equipped with a lead-sulphide detector (PbS) was developed at ULg and installed at the coudé focus of the Jungfraujoch telescope in 1974. It was successfully operated for recording infrared solar spectra from about 1 to 3 µm [*Malbrouck*, 1977]. However, the stepping mode allows for slow scanning speed and was not adequate for fast observations needed in atmospheric composition studies at low solar height observations. Indeed, in order to observe weakly absorbing trace gases, long atmospheric slant paths are more convenient.

In 1978, improvements of that instrument such as an extension of the spectral infrared coverage out to 14 µm, a doubling of the optical path difference, to reach a spectral resolution of 0.0025 cm^{-1} (see Figure 3.8), and a scanning speed increase by a factor 100 obtained by adopting a continuous scanning mode instead of the stepping one were designed [*Delbouille and Roland*, 1995]. This upgraded home-made FTIR instrument was tested then put into regular operation in 1984. The double-pass grating spectrometer was retired in 1989, allowing for regular comparisons between results obtained with the homemade and the double-pass grating spectrometers over up to 5 years [*Zander et al.*, 2008].

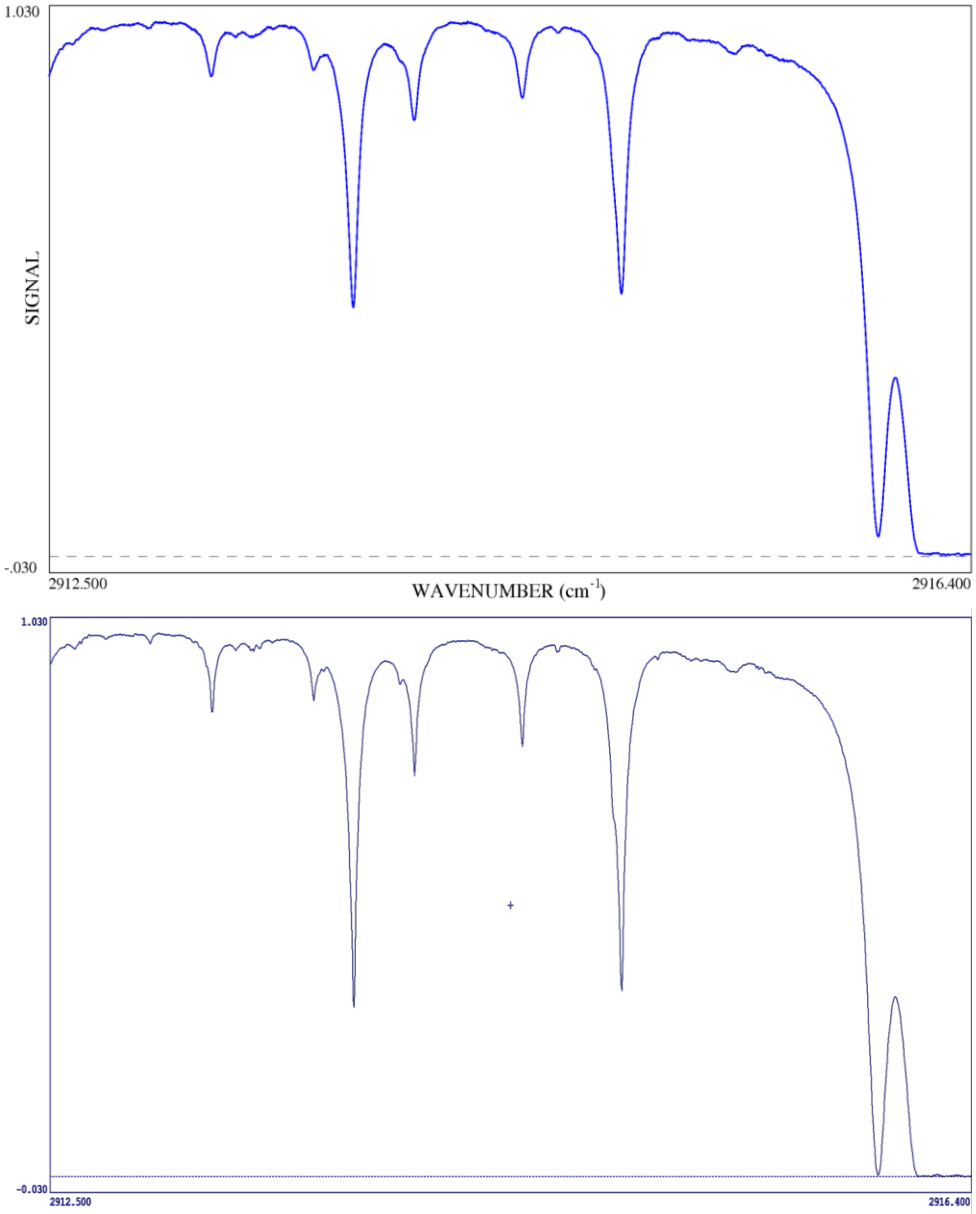

Figure 3.8. Spectrum from the DPGS (upper frame) and FTIR (lower frame) spectrometers on the 2912.5–2916.4 cm^{-1} domain recorded respectively on the 24th of April 1987 and on the 18th of April 2003, with solar zenith angle of 76.12 ° and 76.16 °, respectively.

In 1990, as a result of the creation of the Network for the Detection of Stratospheric Change (NDSC, currently known as the Network for Detection for Atmospheric Change Composition or NDACC since 2005, the slow scanning speed and low throughput Double-Pass Grating Spectrometer (DPGS) was replaced by an FTIR instrument, namely a commercial Bruker IFS-120 HR, achieving an ultimate spectral resolution of 0.001 cm^{-1} and a signal-to-noise ratio exceeding several thousands. Intercomparison tests between the homemade and the Bruker FTIR systems were useful in assessing any level of biasing between retrieved column abundances from simultaneous observations. Currently, infrared spectral domains covered by the Bruker FTIR spectrometer allows for short-, middle- and long-term study, of the evolution of more than

25 atmospheric species such as detailed in Table 3.1. Regular observations with both the homemade and the Bruker spectrometer in addition to the double-pass grating spectrometer gather a unique worldwide collection of solar observations of more than 45 000 spectra that covers more than 39 years of uninterrupted IR monitoring. Figure 3.9 illustrates harmonized total column time series of methane above Jungfraujoch from *Bader* [2011] as retrieved from observations recorded with different instruments such as the double-pass grating spectrometer and both FTIR instruments in addition to historic CH_4 observations from [*Zander et al.*, 1989].

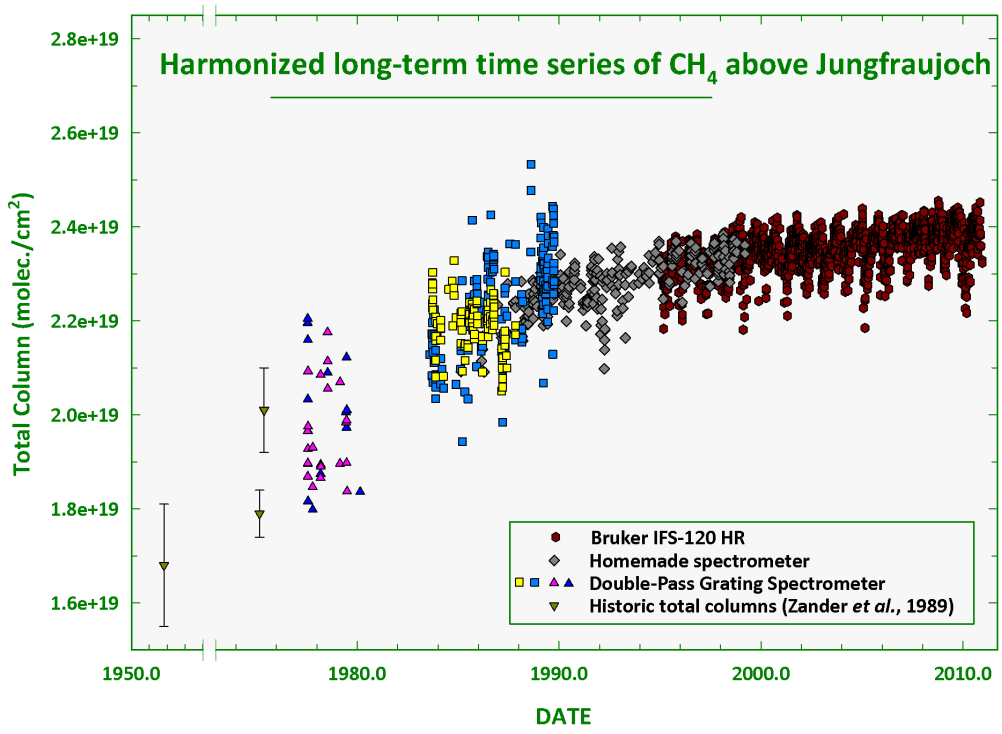

Figure 3.9. Harmonized long-term time series of methane above Jungfraujoch from [*Bader*, 2011]. *Methane total column retrieved from (i) the Bruker IFS-120 HR spectrometer (dark red circles), (ii) the homemade spectrometer (grey diamonds), (iii) the Double-Pass Grating Spectrometer (yellow and blue squares, and blue and pink triangles), and (iv) historic observations (dark yellow down triangles) with their associated uncertainties (black bars) from* [*Zander et al.*, 1989].

Climate-relevant, i.e. greenhouse gases as support to the Kyoto protocol	H_2O, CO_2, [(a)]CH_4, N_2O, CF_4, SF_6
Ozone-relevant as support to the Montreal protocol	O_3, NO, NO_2, HNO_3, $ClONO_2$, HCl, HF, COF_2, CFC-11, CFC-12, HCFC-22, HCFC-142b, CCl_4
Air quality, biomass burning,…	CO, [(b)]CH_3OH, [(c)]C_2H_6, C_2H_2, C_2H_4, HCN, HCHO, HCOOH, NH_3
Others	OCS, N_2, many isotopic forms (HDO, CH_3D, $^{13}CH_4$, ^{13}CO,…)

Table 3.1. Atmospheric species currently targeted at the ISSJ. [*Mahieu et al.*, 2015]. *(a) See chapter 6. (b) See chapter 4. (c) See chapter 5.*

3.5. Atmospheric monitoring: other datasets involved

This section provides a brief description of the several datasets used through the second part of this work for comparisons with our FTIR results. They comprise both observations and model simulations.

3.5.1. Observations

2.5.1.1. The NDACC network

The international Network for the Detection of Atmospheric Composition Change (http://www.ndacc.org/) is composed of more than 70 high-quality, remote-sensing research stations worldwide for observing and understanding the physical and chemical state of the atmosphere, for gauging the atmospheric composition changes and for assessing its impact on global climate or air quality. The NDACC network is divided into 9 working groups, each one associated to one type of instrument that were selected on the basis of their remote-sensing capabilities and their demonstrated stability for long-term operation (for details of site locations and operating equipment, see http://www.ndacc.org).

In 1986, the decision was made to set up a Network for the Detection of Stratospheric Change (NDSC) in support of the 1985 Vienna Convention for the Protection of the Ozone Layer. This ground-based long-term measuring network was designed to provide the earliest possible detection of changes in the composition and structure of the stratosphere and to understand the causes of those changes. After five years of planning, instrument design and implementation, the NDSC began network operations in January 1991. As *Kurylo* [1991] mentioned, the network's short-term goals are: to study the temporal and spatial variability of atmospheric composition and structure, to provide the basis for ground truth and complementary measurements for satellite systems, and to critically test multidimensional stratospheric models and provide the broad data base required for improved model development.

While the NDSC remained committed to monitoring changes in the stratosphere with an emphasis on the long-term evolution of the ozone layer, as a result of its increasing capabilities of monitoring tropospheric source gases, its priorities have broadened considerably to encompass issues such as the detection of trends in overall atmospheric composition and understanding their impacts on the stratosphere and troposphere, and establishing links between climate change and atmospheric composition [*Zander et al.*, 2008]. In 2005, the NDSC formally supported the Kyoto Protocol by extending the range of target species to atmospheric components targeted by the Kyoto Protocol. Consequently, in 2005, the NDSC has been renamed Network for the Detection of Atmospheric Composition Change (NDACC).

Among the 9 working groups, the Infrared Working Group (IRWG, https://www2.acom.ucar.edu/irwg) represents a worldwide network of infrared Fourier-transform spectrometers. It is a multi-national collection of over twenty high resolution spectrometers that regularly perform ground-based solar observations in order to record the atmospheric absorption spectrum from sites distributed from pole to pole. The Figure 3.10 displays the measurements stations which are affiliated to the NDACC as part of the infrared working group.

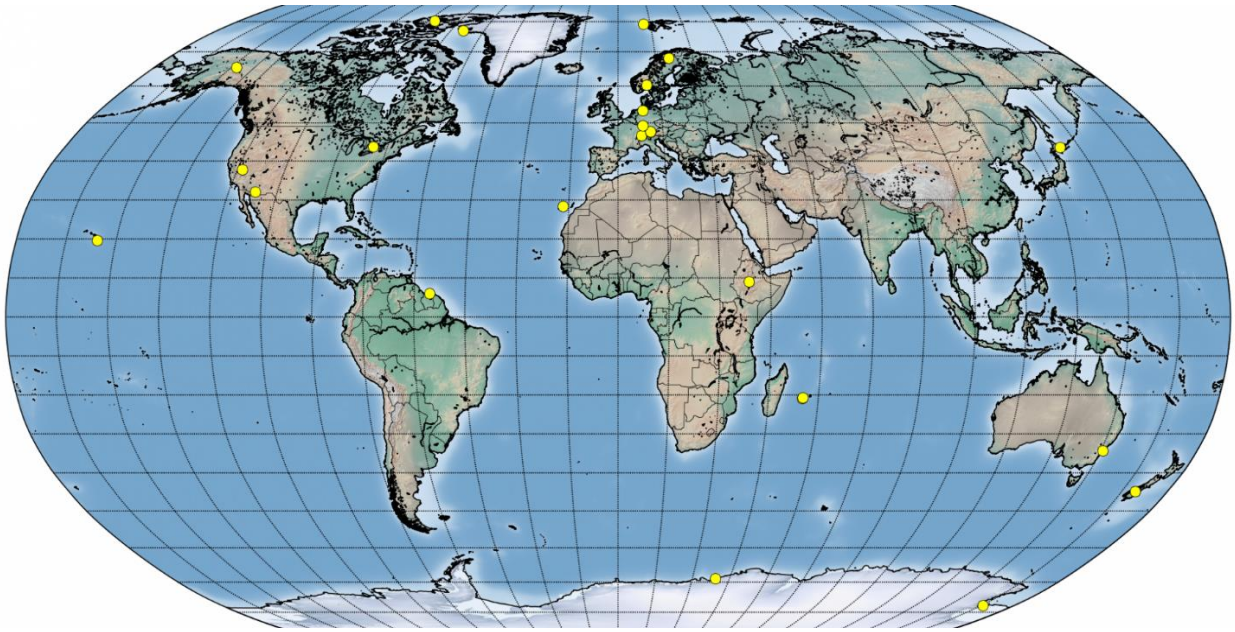

Figure 3.10. Map of measurement stations as part of the NDACC Infrared working group. From Dr. D. Feist, Max Planck Institute for Biogeochemistry, Jena, Germany.

3.5.1.2. ACE-FTS

The SCISAT-1, also known as the Atmospheric Chemistry Experiment [ACE, *Bernath et al.*, 2005], is a Canadian satellite mission whose concept is based on the successful ATMOS (Atmospheric Trace Molecule Spectroscopy) instrument that first flew as part of the Spacelab 3 (SL-3) Space Shuttle in 1985 and three times on the ATLAS (Atmospheric Laboratory for Applications and Science) space shuttle missions [*Gunson et al.*, 1996] for remote sensing of the Earth's atmosphere. The ACE was launched into low Earth circular orbit (650 km) and at a high inclination (74°) in August 2003, benefiting of a coverage of tropical, mid-latitude, and polar regions. ACE aims to understand the chemical and dynamical processes that control the distribution of ozone in the stratosphere and upper troposphere, particularly in the Arctic, to explore the relationship between atmospheric chemistry and climate change, to study the effects of biomass burning on the free troposphere and to measure aerosols and clouds to reduce the uncertainties in their effects on the global energy balance.

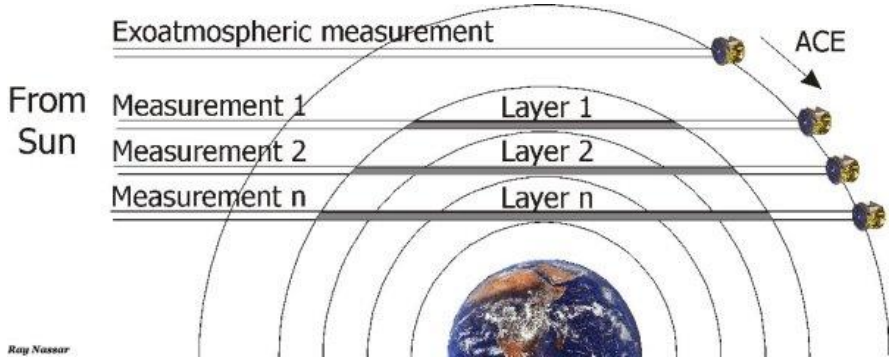

Figure 3.11. Solar occultations as performed by ACE-FTS. http://www.ace.uwaterloo.ca/solar_occultation.html.

The main instrument onboard ACE is a Fourier Transform Spectrometer (FTS) built by ABB-Bomem and equipped with two detectors (InSb and HgCdTe) that covers from 750 to 4400 cm^{-1} with a high resolution of 0.02 cm^{-1} to measure vertical distribution of trace gases and temperature. As illustrated in Figure 3.11, during sunrise and sunset, the FTS measures sequences of atmospheric absorption spectra in the limb viewing geometry with different slant paths and tangent heights. As described in *Bernath et al.*, [2005], the ACE-FTS measurement sequence during a sunset occultation starts with the suntracker pointing to deep space to record a set of instrument self-emission spectra. The deep space spectra are followed by a set of high sun reference spectra obtained by pointing to the center of the sun, and then a sequence of occultation spectra starting at 150 km tangent altitude are obtained at a rate of one scan every 2 s as the sun sets. These spectra are then inverted into vertical profiles of atmospheric constituents, with a vertical resolution of about 4 km from the cloud tops up to about 150 km.

3.5.1.3. in situ GC-MS surface measurements

The Jungfraujoch station also welcomes continuous gas chromatography-mass spectrometry (GC-MS) measurements of gases performed by the Laboratory for Air Pollution and Environmental Technology, Swiss Federal Laboratories for Materials Testing and Research (EMPA) in the framework of the Global Atmosphere Watch (GAW) program of the World Meteorological Organization (WMO, www.wmo.int).

The gas-chromatography coupled with mass spectrometry is a technique that allows for a qualitative and quantitative analysis of several components found within the initial sample. Gas chromatography is an analytical separation technique used to analyze volatile substances in the gas phase such as air samples. Through this separation technique, the components of a sample are separated by dragging of a mobile phase through a stationary phase. The separation will then occur either by the successive adsorption and desorption on the stationary phase or by a difference of solubility into each phase. Regarding mass spectrometry, this analytical chemistry technique allows the quantification of a sample's composition by measuring the mass-to-charge ratio. Indeed, in a typical mass spectrometry procedure, the sample is ionized and the formed ions are separated according to their mass-to-charge ratio.

Networks involved in monitoring the atmosphere composition with either continuous or flask gas chromatography MS measurements at the surface, include the Earth System Research Laboratory from the National Oceanic and Atmospheric Administration (NOAA/ESRL, Boulder, CO, USA, http://www.esrl.noaa.gov/gmd/), the Advanced Global Atmospheric Gases Experiment (AGAGE; Massachusetts Institute of Technology, Cambridge, MA; https://agage.mit.edu/) and the GAW programme. The NOAA/ESRL formerly known as the Climate Monitoring and Diagnostics Laboratory (CMDL) began measurements of climatically important gases on an expanded scale in the mid-1970s. The measurement program includes around the clock measurements at 4 baseline observatories and 8 tall towers, air samples collected at more than 50 sites, and air samples collected regularly from small aircraft mostly in North America. Its mission involves answering key scientific questions in climate forcing, ozone depletion, and air quality. AGAGE has been measuring the composition of the global atmosphere continuously since 1978 from its 14 coastal or mountain stations around the world. The GAW programme (http://www.wmo.int/pages/prog/arep/gaw/gaw_home_en.html) is a partnership involving 30 global and

more than 400 regional atmospheric research stations in 80 countries created in 1989 by the consolidation of two observing networks established during the in 1950s. The three of them share the same objective to provide reliable and accurate measurements of trace gases and information on the chemical composition of the atmosphere, its natural and anthropogenic change. The data collected therefore help to improve the understanding of interactions between the atmosphere, the oceans and the biosphere.

3.5.2. Models

In the second part of this work, model simulations are used as support to interpret our observations and results interpretation. This section provides a quick overview of the models involved in the studies presented in the second part while a more complete description of the simulations employed will be given when mentioned.

3.5.2.1. WACCM

The Whole Atmosphere Community Climate Model [WACCM; *Chang et al.*, 2008; https://www2.cesm.ucar.edu/working-groups/wawg] is a circulation model developed at the National Center for Atmospheric Research (NCAR, Boulder, CO). Chemistry and tracers are calculated using the Model for Ozone and Related Tracers (MOZART), while mesospheric and thermospheric physics are implemented from the Thermosphere Ionosphere Mesosphere Electrodynamics General Circulation Model (TIME-GCM). The model spans the range of altitude from the surface to 140 km.

Within the IRWG, in the use of WACCM outputs for a priori vertical distribution of atmospheric constituents to retrieve is recommended with the aim of using an harmonized and consistent set as a priori profiles for all sites. The vertical distributions are built from monthly WACCMv6 averaged over the 1980-2020 time period and then interpolated to each site from the model output. It includes more than 90 species including major greenhouse gases and air pollutants. Currently, the latest version of WACCM, i.e. version 6, should replace all previous version. However, we will show in chapter 5 that in order to develop a retrieval strategy optimized for a specific station (the Jungfraujoch station in our case) WACCM may not provide the best results in terms of residuals, information content and retrieved vertical profiles. Therefore, it may be required to use additional datasets such as other models and/or observations

3.5.2.2. IMAGES

The Intermediate Model of the Annual and Global Evolution of Species [IMAGES; *Müller and Brasseur*, 1995, 1999] is a global three-dimensional chemical transport model which extends from the surface to the lower stratosphere on 25 vertical levels (up to the pressure of 50 hPa or approximately 22.5 km). IMAGES is run at a resolution of 5° in latitude and longitude with a time step equal to 6 hours. The model simulates the concentration of 59 long- and short-lived atmospheric constituents through a chemical mechanism including 133 gas-phase reactions, 29 photodissociations, and 3 heterogeneous reactions on the surface of sulfate aerosols. Large-scale transport parameters are driven by averaged climatological fields from the European Centre for Medium-Range Weather Forecasts (ECMWF, http://www.ecmwf.int/).

3.5.2.3. CHASER

The CHemical AGCM for Study of atmospheric Environment and Radiative forcing model [CHASER; *Sudo*, 2002; *Sudo and Akimoto*, 2007], has been developed mainly in the Nagoya University and the Japan Agency for Marine-Earth Science and Technology (JAMSTEC) in the framework of the Model for Interdisciplinary Research on Climate-Earth System Model, MIROC-ESM-CHEM [*Watanabe et al.*, 2011]. CHASER is a chemistry coupled climate model used in cooperation with the aerosol component model SPRINTARS [Spectral Radiation-Transport Model for Aerosol Species; *Takemura*, 2005]. It studies tropospheric ozone and related chemistry and their impact on climate by simulating detailed chemistry in the troposphere and stratosphere with an on-line aerosol simulation including production of particulate nitrate and secondary organic aerosols.

3.5.2.4. GEOS-Chem

GEOS-Chem [*Bey et al.*, 2001a; www.geos-chem.org] is a global 3-D CTM for atmospheric composition driven by meteorological input from the Goddard Earth Observing System (GEOS) of the NASA Global Modeling and Assimilation Office and managed by the GEOS-Chem Support Team, based at Harvard University and Dalhousie University with support from the US NASA Earth Science Division and the Canadian National and Engineering Research Council. The model supports input data from GEOS-4 (1° x 1.25° horizontal resolution, 55 vertical levels), GEOS-5 (0.5° x 0.666°, 72 levels), MERRA (0.5° x 0.666°, 72 levels), and GEOS-FP (0.25° x 0.3125°, 72 levels, starting in April 2012). The GEOS meteorological data archive has a temporal resolution of 3 hours (MERRA, GEOS-FP) or 6 hours (GEOS-4, GEOS-5).

GEOS-Chem simulations can be conducted at the native resolution of the GEOS fields or at coarser resolution (2° x 2.5° or 4° x 5°). Standard GEOS-5 and GEOS-FP nested windows for aerosol-oxidant simulations are available for East Asia [*Chen et al.*, 2009], North America [*van Donkelaar et al.*, 2012; *Zhang et al.*, 2012], and Europe [*van Donkelaar et al.*, 2013].

GEOS-Chem includes detailed HO_x-NO_x-VOC-ozone-BrO_x tropospheric chemistry as originally described by [*Bey et al.*, 2001a] and with addition of BrO_x chemistry by *Parrella et al.*, [2012]. GEOS-Chem simulation modes consists of a full chemistry, tagged CO [*Bey et al.*, 2001b], tagged Ox, tagged CH_4 [*Wang*, 2004; *Wecht et al.*, 2014], offline aerosols and CO_2 [*Suntharalingam*, 2004].

Chapter 4 – Methanol

Chapter 4 − Methanol

4.1. Introduction

The primary challenge on the methanol study was to develop a retrieval strategy optimized for observations recorded at the Jungfraujoch station. The development of a methanol retrieval strategy included testing of numerous inversion strategies (see Table 4.0) for evaluation of methanol absorption lines as used in previous studies [*Dufour et al.*, 2007; *Rinsland et al.*, 2009; *Vigouroux et al.*, 2012] and determination of the best combination of spectral windows, the solar zenith angle range, the methanol a priori mixing ratio profile [*Chang et al.*, 2008], and the signal-to-noise ratio for inversion, among others. The successive tests for an optimized retrieval strategy were based on a subset of 314 spectra covering the year 2010, representative of each season and of the range of solar zenith angle. We selected the best strategy on the basis of minimum interferences, minimum residuals and maximum information content. In addition, a systematic and careful error budget has been determined further guiding the choice of the best retrieval strategy for methanol above Jungfraujoch. The evaluations were performed according to the method developed through this work and described in section 2.3. This retrieval strategy is the object of a paper published in the Atmospheric Measurement and Techniques journal [see next section; *Bader et al.*, 2014].

Parameter	Number of tests
Solar zenith angle range	4
Windows, interfering species to retrieve	14
Signal-to-noise ratio for inversion	26
CH_3OH a priori profile	8
Effective apodisation parameter	4
Other	6
Total	**62**

Table 4.0. Overview of tests performed for the optimization of the methanol retrieval strategy for Jungfraujoch.

The evaluation of the combination of spectral windows is based on previous work from the retrieval of CH_3OH from FTIR observations performed at Kitt Peak [*Rinsland et al.*, 2009], from ACE-FTS occultation observations [*Dufour et al.*, 2007] and from FTIR observations at Reunion Island [*Vigouroux et al.*, 2012]. We have for the first time –for ground-based FTIR observations– combined several spectral windows, as illustrated in Figure 4.0.1. The identification of best window limits and of the interfering species to be accounted for has been performed through 14 inversions. Moreover, since the fitting quality is significantly different in both windows, values for the signal-to-noise ratio for inversion (SNR) have been selected for each window individually. The different SNR for both window has been taken into account in the error budget.

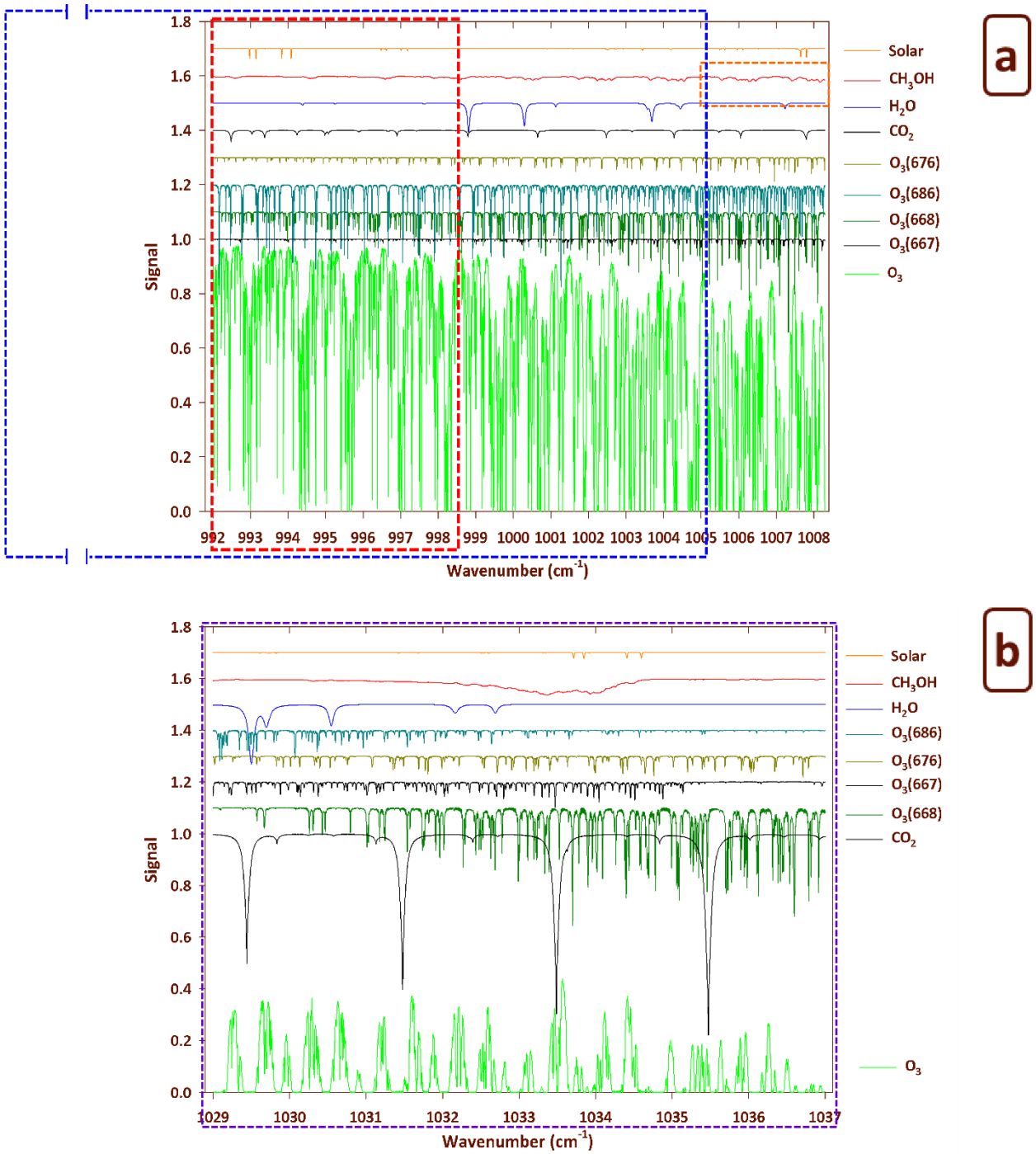

Figure 4.0.1. Simulation for Jungfraujoch, 80° zenith angle, resolution of 6.1 mK or 0.0061 cm^{-1}. For both windows, we display the synthetic spectra for individual contributors (see color codes). HITRAN 2008 and averaged mixing ratio profiles based on the WACCM model climatology have been used for the simulations, except for CH3OH for which our a priori was used (see 4.2.2.). For clarity, the contributions of each species have been vertically shifted. (a) First spectral window used for the retrievals ranging from 992 to 1008.3 cm^{-1}, the red frame shows the 992–998.7 cm^{-1} window from Rinsland et al., [2009]*, the blue frame shows the 984.9–1005.1 cm^{-1} window from ACE-FTS CH3OH retrievals (version 3.5) in addition to supplemental methanol features up to the 1008.3 cm^{-1} limit in the orange frame. (b) The second spectral window defined ranges from 1029 to 1037 cm^{-1} and is from Vigouroux et al., [2012] illustrated by the purple frame.*

Since the CH_3OH absorption lines are quite weak, we needed to restrain the spectra selection from the 498 observations available for the year 2010 to a specific range of solar zenith angle (SZA). To this end, we performed the inversion for the whole SZA range available (Figure 4.0.2) and determined that a minimum SZA of 60° is required to reach a DOFS of approximately 1.

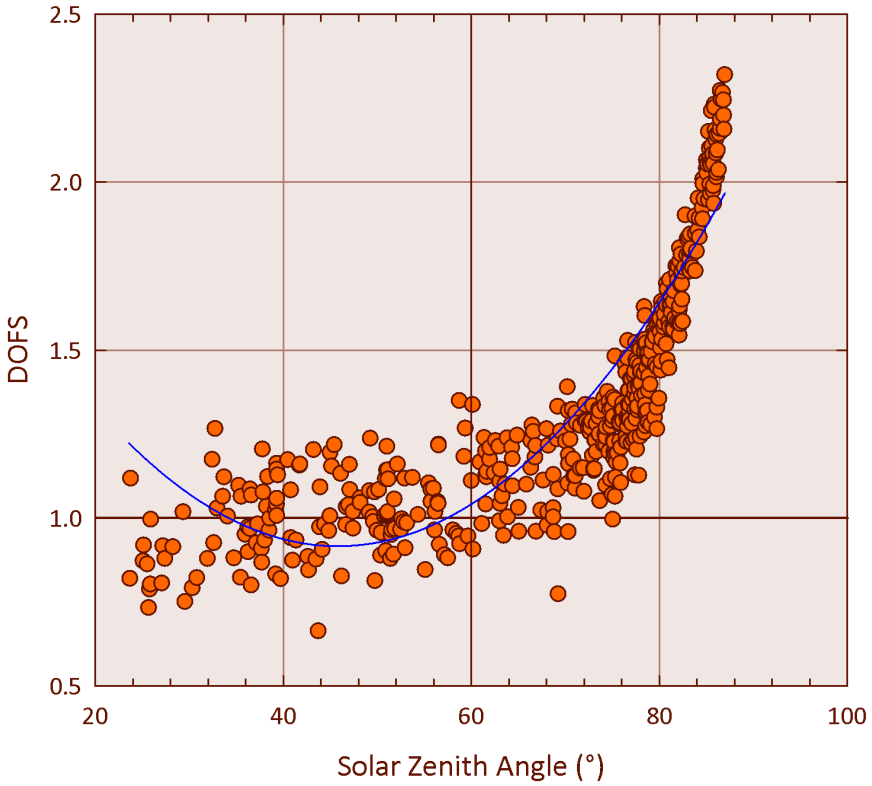

Figure 4.0.2. DOFS as a function of the solar zenith angle. Blue curve is a second order polynomial fit of data.

Even if *Rinsland et al.* [2009] showed evidence of a methanol contribution to the spectra from Kitt Peak FTIR observations (2090 m a.s.l.), we needed to ascertain that retrieved methanol columns were independent of retrieved ozone columns since the Jungfraujoch observations have likely less absorption by CH_3OH due to the high altitude of the station (3580 m a.s.l.). In fact, as illustrated in Figure 4.0.3, retrieved methanol columns are neither correlated with retrieved total columns of O_3 nor $O_3(686)$ with coefficient of determination respectively of 0.0084 and 0.0006. Other parameters have been examined and included in the retrieval strategy such as adjustment of the slope and curvature of the spectrum, the effective apodisation parameter accounting for the good alignment of the instrument.

Harmonization efforts to include homemade FTIR measurements in order to extend the time series of methanol back to 1987 were not conclusive. Indeed, because of their lower signal-to-noise ratio [*Mahieu et al.*, 2014], too many CH_3OH vertical profiles we retrieved showed strong oscillations associated to ungeophysical negative mixing ratio values in the lower-troposphere. Therefore, in [*Bader et al.*, 2014] we only presented results retrieved from the Bruker spectrometer.

Once the retrieval strategy is optimized and the product characterized in terms of information content and uncertainty, we were able to move on with trend and seasonal cycle analysis along with diurnal variations with support –and comparison with– from GC-MS in situ surface measurements [*Legreid et al.*, 2008], ACE-FTS occultations observations [*Dufour et al.*, 2007] and simulations from the model IMAGESv2 [*Stavrakou et al.*, 2011]. This study contributes to filling the gap in FTIR methanol studies. As there still remain large uncertainties in the methanol budget, long-term time series of methanol observations should provide better constraints for model and satellite validation.

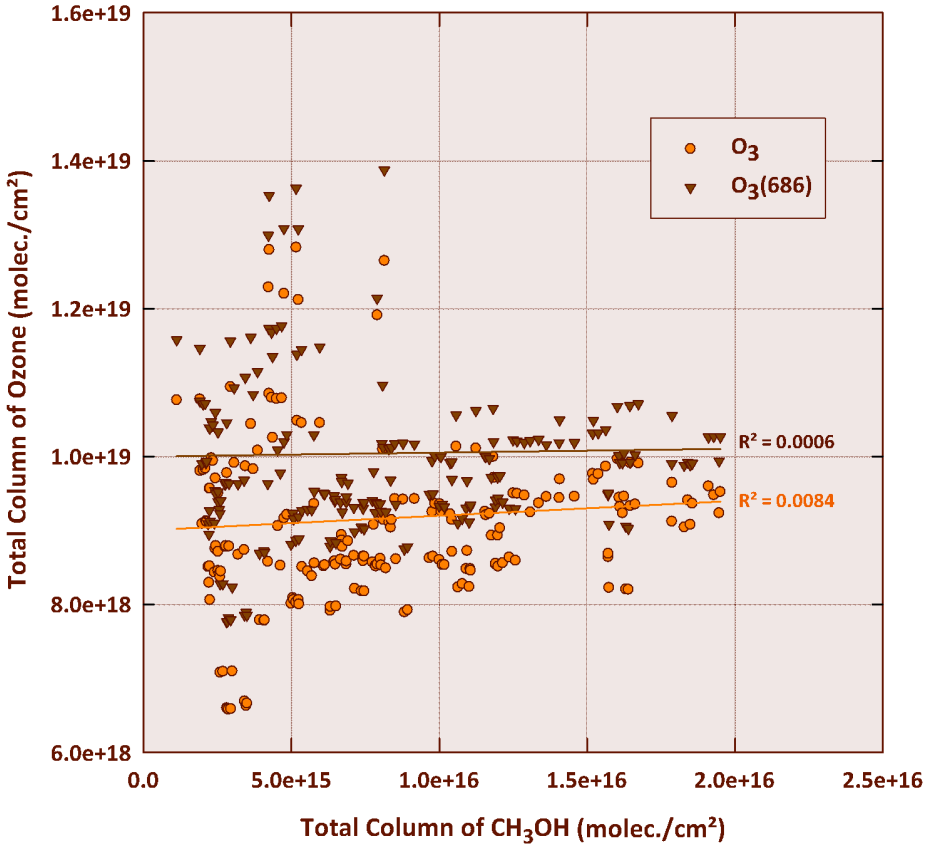

Figure 4.0.3. Total column of ozone (O_3 in orange and O_3(686) in brown) as a function of retrieved total column of methanol. Straight lines show respective linear fit with their associated coefficient of determination.

4.2. Long-term evolution and seasonal modulation of methanol above Jungfraujoch (46.5°N, 8.0°E): optimization of the retrieval strategy, comparison with model simulations and independent observations

Reference: Bader, W., Stavrakou, T., Muller, J.-F., Reimann, S., Boone, C. D., Harrison, J. J., Flock, O., Bovy, B., Franco, B., Lejeune, B., Servais, C., and Mahieu, E.: Long-term evolution and seasonal modulation of methanol above Jungfraujoch (46.5°N, 8.0°E): optimization of the retrieval strategy, comparison with model simulations and independent observations, Atmos. Meas. Tech., 7, 3861-3872, doi: 10.5194/amt-7-3861-2014, 2014.

W. Bader[1], T. Stavrakou[2], J.-F. Muller[2], S. Reimann[3], C. D. Boone[4], J. J. Harrison[5], O. Flock[1], B. Bovy[1], B. Franco[1], B. Lejeune[1], C. Servais[1], and E. Mahieu[1]

[1] Institute of Astrophysics and Geophysics of the University of Liège, Liège, Belgium
[2] Belgian Institute for Space Aeronomy, Avenue Circulaire 3, 1180, Brussels, Belgium
[3] Laboratory for Air Pollution and Environmental Technology, Swiss Federal Laboratories for Materials Testing and Research (EMPA), Dübendorf, Switzerland
[4] Department of Chemistry, University of Waterloo, Ontario, Canada 5Department of Chemistry, University of York, York, UK

Received: 11 April 2014 – Published in Atmos. Meas. Tech. Discuss.: 8 May 2014
Revised: 2 October 2014 – Accepted: 16 October 2014 – Published: 21 November 2014
Edited by: F. Boersma

Abstract

Methanol (CH_3OH) is the second most abundant organic compound in the Earth's atmosphere after methane. In this study, we present the first long-term time series of methanol total, lower tropospheric and upper tropospheric– lower stratospheric partial columns derived from the analysis of high resolution Fourier transform infrared solar spectra recorded at the Jungfraujoch station (46.5°N, 3580 m a.s.l.). The retrieval of methanol is very challenging due to strong absorptions of ozone in the region of the selected v8 band of CH_3OH. Two wide spectral intervals have been defined and adjusted in order to maximize the information content. Methanol does not exhibit a significant trend over the 1995–2012 time period, but a strong seasonal modulation characterized by maximum values and variability in June–July, minimum columns in winter and a peak-to-peak amplitude of 130 %. Analysis and comparisons with in situ measurements carried out at the Jungfraujoch and ACE-FTS (Atmospheric Chemistry Experiment-Fourier Transform Spectrometer) occultations have been performed. The total and lower tropospheric columns are also compared with IMAGESv2 model simulations. There is no systematic bias between the observations and IMAGESv2 but the model underestimates the peak-to-peak amplitude of the seasonal modulations.

4.2.1. Introduction

Methanol (CH_3OH) is the second most abundant organic molecule in the atmosphere after methane, with concentrations between 1 [*Singh et al.*, 2001] and 20 ppbv [*Heikes et al.*, 2002], despite a lifetime that has been estimated to lie between 4.7 days [*Millet et al.*, 2008] and 12 days [*Atkinson et al.*, 2006]. Plant growth is the largest source of methanol with a 65–80 % contribution to its emissions [*Galbally and Kirstine*, 2002; *Jacob*, 2005]. The atmospheric production of CH_3OH through peroxy radical reactions represents up to 15–23 % of its sources [*Madronich and Calvert*, 1990; *Tyndall et al.*, 2001]. Other sources of methanol are plant matter decaying [*Warneke et al.*, 1999], biomass burning [*Dufour et al.*, 2006; *Paton-Walsh et al.*, 2008], fossil fuel combustion, vehicular emissions, solvents and industrial activities.

Methanol influences the oxidizing capacity of the atmosphere through reaction with the hydroxyl radical [*Jiménez et al.*, 2003], its main sink, leading to the formation of water vapor and either CH_3O or CH_2OH radicals, which both react with O_2 to give HO_2 and formaldehyde (H_2CO) [*Millet et al.*, 2006]. The photo-oxidation of formaldehyde, a key intermediate in the oxidation of numerous volatile organic compounds, leads to the formation of HO_2 radicals and carbon monoxide (CO). As a consequence, CH_3OH is considered as a source of CO with a yield close to 1 [*Duncan et al.*, 2007]. The main sources and sink of methanol are characterized by significant seasonal modulations. This results in a strong signal for CH_3OH, with maximum and minimum abundances observed in the Northern Hemisphere at the beginning of July and in December, respectively [*Rinsland et al.*, 2009; *Razavi et al.*, 2011; *Cady-Pereira et al.*, 2012; *Wells et al.*, 2012], reflecting the seasonality of biogenic sources.

In the past decade, ground-based [*Schade and Goldstein*, 2001, 2006; *Karl et al.*, 2003; *Carpenter et al.*, 2004] and aircraft [*Fehsenfeld et al.*, 2006; *Singh et al.*, 2006] in situ measurements combined with space-based measurements, including the Infrared Atmospheric Sounding Interferometer (IASI) on board the MetOp-A satellite [*Razavi et al.*, 2011], the TES (Tropospheric Emission Spectrometer) nadir-viewing Fourier transform spectrometer (FTS), on board the Aura satellite [*Beer et al.*, 2008], and the solar occultations recorded by the Atmospheric Chemistry Experiment-FTS [ACE-FTS, *Bernath et al.*, 2005; *Dufour et al.*, 2006, 2007] have supplied numerous observations of CH_3OH, which have provided valuable insights on the distribution and budget of methanol at the global scale. In addition, previous studies have reported the measurement of methanol from ground-based infrared solar absorption observations performed at Kitt Peak [31.9°N, 111.6°W, 2090 m a.s.l.; *Rinsland et al.*, 2009] and at Saint- Denis [Reunion Island, 21°S, 55°E, 50 m a.s.l.; *Stavrakou et al.*, 2011; *Vigouroux et al.*, 2012]. However, there still remain large uncertainties in our knowledge of the methanol global sources and sinks, as indicated by the large discrepancies existing between different measurement-based estimates of the total sources [*Galbally and Kirstine*, 2002; *Tie et al.*, 2003; *von Kuhlmann*, 2003; *von Kuhlmann et al.*, 2003; *Jacob*, 2005; *Millet et al.*, 2008; *Stavrakou et al.*, 2011]

In this paper, we report the first long-term methanol time series (17 years) derived from ground-based high-resolution infrared spectra recorded with a Fourier transform infrared (FTIR) spectrometer operated under clear sky conditions at the high-altitude International Scientific Station of the Jungfraujoch [ISSJ, Swiss Alps, 46.5°N, 8.0°E, 3580 m a.s.l.; *Zander et al.*, 2008] providing a valuable tool for model and

satellite validation. Most of the available spectra have been recorded within the framework of the Network for Detection of Atmospheric Composition Change monitoring activities (NDACC; see http://www.ndacc.org) complementing the NDACC measurements at northern mid-latitudes. A detailed analysis was conducted to optimize the retrieval strategy of atmospheric methanol in order to minimize the fitting residuals while maximizing the information content. A thorough discussion of the retrieval strategy, data characterization (information content and error budget), long-term trend and seasonal cycle of total and partial columns of methanol above Jungfraujoch is presented here. This paper is organized as follows. A detailed description of the optimized retrieval strategy is given in Sect. 2. The characterization of our data by their eigenvectors and error budget is discussed in Sect. 3. Finally, in Sect. 4, we present and discuss the results, focusing on the intra-annual and intra-day variability of methanol at ISSJ along with comparisons with in situ measurements, satellite occultations and model calculations.

4.2.2. Retrieval strategy

Regular FTIR observations have been carried out at the ISSJ with a homemade spectrometer since 1984, complemented in the early 1990s and then definitely replaced by a commercial Bruker IFS-120HR instrument [*Zander et al.*, 2008]. This spectrometer is equipped with HgCdTe and InSb cooled detectors, allowing us to cover the 650 to 4500 cm^{-1} region of the electromagnetic spectrum. Since 1991, the FTIR instruments are affiliated with the NDACC network.

The Bruker observational database consists of more than 6500 spectra recorded between 1995 and 2012 with an optical filter covering the 700 to 1400 cm^{-1} domain encompassing the fundamental C-O stretching mode v8 of methanol at 1033 cm^{-1}. Spectral resolution, defined as the reciprocal of twice the maximum optical path difference, alternates between 0.004 and 0.006 cm^{-1}. Signal-to-noise (S/N) ratios vary between 250 and 1800 (average spectra resulting from several successive individual Bruker scans, when solar zenith angles vary slowly). The optimization of the retrieval strategy was based on a subset of 314 spectra covering the year 2010.

The CH_3OH column retrievals and profile inversions have been performed using the SFIT-2 v3.91 fitting algorithm. This retrieval code has been specifically developed to derive mixing ratio profiles of atmospheric species from ground based FTIR spectra [*Rinsland et al.*, 1998]. It is based on the semi-empirical implementation of the Optimal Estimation Method (OEM) developed by [*Rodgers*, 1990]. Vertical profiles are derived from simultaneous fits to one or more spectral intervals in at least one solar spectrum with a multilayer, line-by-line calculation that assumes a Voigt line shape [*Drayson*, 1976]. The model atmosphere adopted above the Jungfraujoch altitude consists of a 39 layers scheme with progressively increasing thicknesses, from 3.58 km to reach the 100 km top altitude. The pressure-temperature profiles are provided by the National Center for Environmental Prediction (NCEP, Washington DC, USA, http://www.ncep.noaa.gov/) while the solar line compilation supplied by F. Hase (KIT) [*Hase et al.*, 2006] has been assumed for the solar absorptions. Line parameters used in the spectral fitting process were taken from the HITRAN 2008 spectroscopic compilation [*Rothman et al.*, 2009]. Methanol lines were added to the HITRAN compilation for the first time in 2004 [*Rothman et al.*, 2005]. The parameters for the 10 µm region

are described in the paper by *Xu et al.* [2004] and were derived from measurements with two high-spectral resolution FTS instruments.

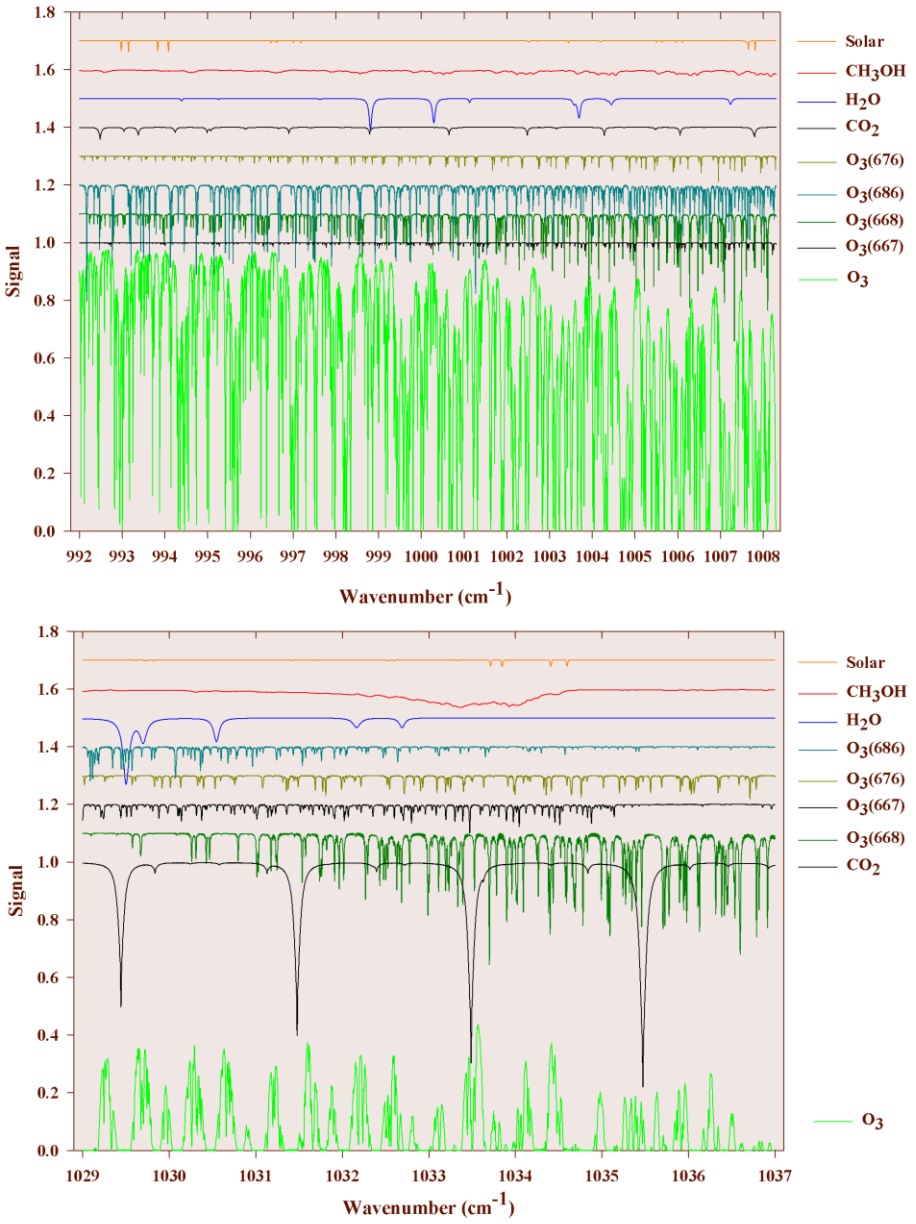

Figure 4.1. Simulation for Jungfraujoch, 80° zenith angle, 6.1 mK. For both windows, we display the synthetic spectra for individual contributors (see color codes). HITRAN 2008 and averaged mixing ratio profiles based on the WACCM model climatology have been used for the simulations, except for CH3OH for which our a priori was used (see text). For clarity, the contributions of each species have been vertically shifted.

Two spectral windows both encompassing the ν8 C–O stretch absorption band of methanol have been defined. Synthetic spectra (6.1 mK or 0.0061 cm^{-1}, zenith angle of 80°) have been computed for the first and second order absorbers in both selected windows and are illustrated in Figure 4.1. The first interval ranges from 992 to 1008.3 cm^{-1} and is based on windows used in previous investigations. A 992–998.7 cm^{-1}

window was employed for the retrieval of CH_3OH from Kitt Peak FTS spectra [*Rinsland et al.*, 2009] and a 984.9–998.7 cm^{-1} window was used for the initial retrievals of methanol from ACE-FTS occultation observations [*Dufour et al.*, 2007]. The latest ACE-FTS CH_3OH retrievals (version 3.5) use an extended window from 984.9 to 1005.1 cm^{-1}. Measuring in the limb, ACE-FTS measurements start to saturate for wavenumbers above 1005.1 cm^{-1} for occultations with higher than average O_3 levels. As ground-based observations do not have this problem, we included supplemental methanol features up to the 1008.3 cm^{-1} limit. The second interval, ranging from 1029 to 1037 cm^{-1} is used by [*Vigouroux et al.*, 2012].

Absorption by the main ozone isotopologue (^{16}O-^{16}O-^{16}O or O_3) captures nearly 93 and 98 % of the IR radiation in the "1008" and "1037" windows respectively and is close to saturation in the latter one. Methanol features are much weaker, with mean absorption of 1.7 and 1.8 % in the "1008" and "1037" windows respectively. Additional absorptions are associated with O_3 isotopologues, such as O_3(668) or (^{16}O-^{16}O-^{18}O), O_3(686) or (^{16}O-^{18}O-^{16}O), O_3(676) or (^{16}O-^{17}O-^{16}O) and O_3(667) or (^{16}O-^{16}O-^{17}O) as well as carbon dioxide (CO_2) and water vapor (H_2O). Since the CH_3OH absorption lines are quite weak, only spectra with solar zenith angles greater than 65° and up to 80° have been analyzed. During the retrievals, both windows were for the first time fitted simultaneously.

The a priori mixing ratio profile for the CH_3OH target is a zonal mean (for the 41–51°N latitude band) of 903 occultations recorded by the ACE-FTS instrument (version 3.5) between 27 March 2004 and 3 August 2012, extending from 5.5 to 30 km tangent altitudes. The profile was extrapolated to 1 ppbv to the surface [*Singh et al.*, 2001; *Heikes et al.*, 2002], and to 0.05 ppbv [*Singh et al.*, 2006; *Dufour et al.*, 2007] for upper layers. The covariance matrix is specified for each layer as a percentage of the a priori profile and an ad hoc correlation length, which is interpreted as a correlation between layers decaying along a Gaussian. For methanol, we adopted a 50 %.km^{-1} diagonal covariance and a Gaussian half width of 4 km for extra diagonal elements. A priori profiles for all interfering molecules are based on the WACCM [version 5, the Whole Atmosphere Community Climate Model, e.g. *Chang et al.*, 2008] model climatology for the 1980-2020 period and the ISSJ station. The vertical profiles of CH_3OH, O_3 and O_3(668) are fitted during the iterative process while the a priori distributions of O_3(686), O_3(676), O_3(667), H_2O and CO_2 are scaled. Since the fitting quality is significantly different in both windows, two different values for the signal-to-noise ratio for inversion have been selected, i.e. 180 and 40 for the "1008" and "1037" domains, respectively.

When fitted independently, we observe a compact correlation between the corresponding CH_3OH total columns retrieved from both windows with a small bias of 15 ± 13 % (2σ). When comparing ozone total columns respectively retrieved from the strategy described in this work and from the retrieval strategy applied within the NDACC network [window limits: 1000–1005 cm^{-1},*Vigouroux et al.*, 2012], no significant bias emerges from the comparison between the two ozone total column sets, with a mean relative difference of -0.8 ± 2.4 % (2σ), demonstrating a proper fit of the main interference involved in our methanol retrieval strategy. Additional functions are also included in the fitting process to account for deviations from a perfectly aligned FTS. As an effective apodisation function, we assumed a polynomial function of order 2 [*Barret et al.*, 2002]. The effective apodisation parameter (EAP) gives the value of the effective apodisation function at the maximum optical path difference and is synonymous of a well-aligned

instrument when it is close to 1.0. The inversion of the EAP has been included in our retrieval as well as in the NDACC's retrieval strategy of ozone. The EAP derived from both strategies proved to be consistent, with a mean relative difference of 0.7 ± 2.6 % (2σ). Those three latter points give confidence in the combination of the two selected windows and in our optimized retrieval strategy.

4.2.3. Data characterization and error budget

Information content has been carefully evaluated and typical results are displayed on Figure 4.2. The information content is significantly improved, with a typical degree of freedom for signal (DOFS) of 1.82, in comparison with DOFS of about 1 in previous studies [e.g. *Rinsland et al.*, 2009; *Vigouroux et al.*, 2012]. In Figure 4.2, the first eigenvector and eigenvalue (see left panel, in orange) show that the corresponding information is mainly coming from the retrieval (99 %). The increase of information content allows us to retrieve a tropospheric column (Tropo, from 3.58 to 10.72 km) with only 1 % of a priori dependence as well as two partial columns with less than 30 % of a priori dependence (second eigenvector), i.e. a low-tropospheric (LT, from 3.58 to 7.18 km) and an upper troposphere–lower stratosphere (UTLS, from 7.18 to 14.84 km).

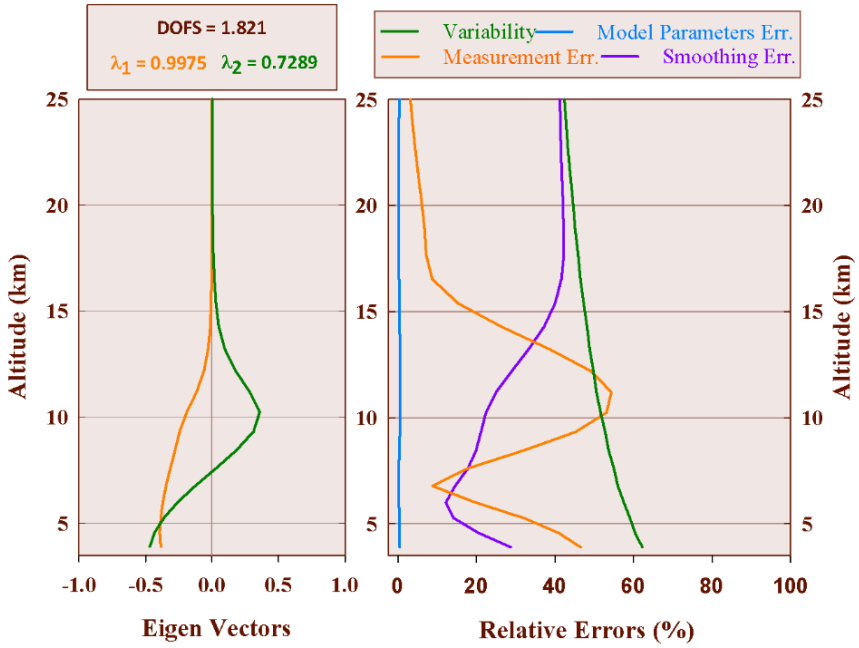

Figure 4.2. Typical results for information content and error budget. Left frame: first eigenvectors and corresponding eigenvalues. Right frame: error budget, with identification of the main error components, together with the assumed variability (see color codes and Table 4.1 for additional information).

The error budget is calculated following the formalism of *Rodgers* [2000], and can be divided into three different error sources: the smoothing error expressing the uncertainty due to finite vertical resolution of the remote sounding system, the forward model parameters error, and the measurement noise error. The right panel of Figure 4.2 gives the corresponding error budget, with identification of the main error components, together with the assumed variability. Error contributions for total and all three partial columns are reported in Table 4.1.

Through a perturbation method, we also accounted for other error sources: systematic errors, such as the spectroscopic line parameters and the misalignment of the instrument, while uncertainty on the temperature and on the solar tracking is considered to be source of random error. Table 4.1 provides an error budget resulting from major instrumental and analytical uncertainties. For the spectroscopic line parameters, we included in our error budget the uncertainty on line intensities provided by the HITRAN database. As methanol line intensities matter, a rough idea of the accuracy of the intensities can be obtained from Table 8 of the *Xu et al.* [2004] study, as it reports an RMS deviation of 7 %. It should be noted that the uncertainty on ozone and its isotopologues lines, according to HITRAN-08 parameters, amounts to between 5 and 10 % [*Rothman et al.*, 2009]. However, an extremely high accuracy of ozone spectroscopic parameters is required in order to retrieve methanol columns properly.

We noted that the SFIT-2 algorithm fails to perform a satisfying retrieval when using spectroscopic parameters with ozone lines intensity incremented by 10 %, suggesting that the error on the concerned lines intensity is more likely to be closer to 5 (or even lower) than to 10 %. Therefore, we accounted for an error on ozone and its isotopologues line intensities of 5 % in our error budget.

Error Sources	Max. Error (%)				
	TC	Tropo	LT	UTLS	
Variability	46	50	57	48	
	Systematic Errors (%)				Comments
	TC	Tropo	LT	UTLS	
Line intensity CH_3OH	7.02	7.11	6.39	9.22	Xu et al., 2004
Line intensity interfering gases	1.00	1.73	3.96	0.91	Rothman et al., 2009 and ± 5% for all O_3 isotopologues lines
ILS	0.41	0.33	1.19	2.39	± 10% misalignment
Forward model	1	< 1	< 1	< 1	Retrieval algorithm-related
Total	7.17	7.39	7.68	9.62	
	Random Errors (%)				
	TC	Tropo	LT	UTLS	
P-T profiles	1.2	2.3	11.3	8.6	From NCEP
SZA	0.2	0.4	3.1	1.4	0.2°
Smoothing	0.4	4.4	16.1	15.2	Barret et al., 2002
Measurement noise	5.2	19.4	35.9	37.5	
Model parameters	0.7	0.6	0.5	1.2	
Total	5.37	20.04	40.18	41.43	
Relative Standard Deviation	6.60	8.34	22.59	21.11	

Table 4.1. Error budget for total and all three partial columns. TC: total column, Tropo: tropospheric column, LT: lower tropospheric layer, UTLS: upper troposphere/lower stratosphere.

We accounted for an error of 10 % on the instrument alignment at the maximum path difference. By comparing the two official NDACC algorithms, *Hase et al.* [2004] and *Duchatelet et al.*, [2010] have established that the forward model may induce a maximum error of 1 % on the retrieved columns for a suite of FTIR target gases. The uncertainty on the pressure–temperature profiles is provided by NCEP with an error of 1.5 K from the ground to an altitude of about 20 km. Concerning the upper levels, the uncertainty increases with altitude, from 2 K around 25 km until 9 K at the top. The uncertainty on the solar zenith angle (SZA) is estimated at 0.2°.

We also provide in Table 4.1 the mean relative standard deviation for each daily mean for days with three or more measurements. It is found to be of the same order of magnitude as the random error. The dominant contribution to the systematic error is the error on methanol spectroscopic lines, while the measurement noise error is the main component of random error. Both systematic and random errors are given in Table 4.1, with 7 % and around 5 % respectively on the total columns.

4.2.4. Results and comparisons

Since the improvement in information content allows us to compute partial columns with only a 30 % a priori dependence and as the random error on the tropospheric column is about four times the error on total columns (see Table 4.1), we focus our trend analysis on total, LT and UTLS columns. Therefore, an analysis of the seasonal variation of methanol in the lower troposphere and the UTLS has been performed, including comparisons with in situ measurements [*Legreid et al.*, 2008] and to ACE-FTS occultation observations, respectively. Comparisons with simulations obtained from the IMAGESv2 global chemistry-transport model [*Stavrakou et al.*, 2011] have also been conducted.

4.2.4.1. Data description

In situ measurements have been performed at the ISSJ station from air samples collected on a two-stage adsorbent system connected to a gas chromatograph–mass spectrometer [GC-MS; *Legreid et al.*, 2008]. The system was in operation during four measurement campaigns in 2005, which were performed from 8 February until 8 March 2005 for the winter measurements, spring measurements followed from 22 April until 30 May, in summertime measurements start from 5 August until 19 September and autumn measurements from 14 October until 1 November, with a frequency of about one sample every 50 min. A total of 1848 measurements of methanol on 122 days have been compared with our lower-tropospheric column time series for the year 2005.

Monthly mean UTLS columns have been derived from measurements taken by the ACE-FTS instrument and compared to our UTLS product. We selected and converted into partial columns the mixing ratios measured by ACE-FTS during ~140 occultations performed in the altitude range of 7.5–14.5 km [version 3.5; *Boone et al.*, 2013] in the 41.5° to 51.5° northern latitude zone between 30 March 2004 and 20 February 2013.

Two model simulations of daily methanol mixing ratios in the 2004–2012 time period obtained from the IMAGESv2 global chemistry-transport model [fully described in *Stavrakou et al.*, 2011] are presented here. The IMAGESv2 model was run at a resolution of 2° in latitude and 2.5° in longitude and with a time step of 6h. It has 40 vertical (hybrid sigma-pressure) levels between the Earth's surface and the lower stratosphere 25 (44 hPa). Daily averaged mixing ratios calculated by the model at the model pixel comprising the ISSJ station were used to calculate the partial and total columns above the station. The first simulation "MEGAN", is performed using MEGANv2.1 bottom-up emissions, which are calculated using an emission model fitted to net ecosystem flux measurements. The second one, "IASI", uses emissions constrained by IASI vertical column data in an inverse modelling framework based on the adjoint of IMAGESv2.

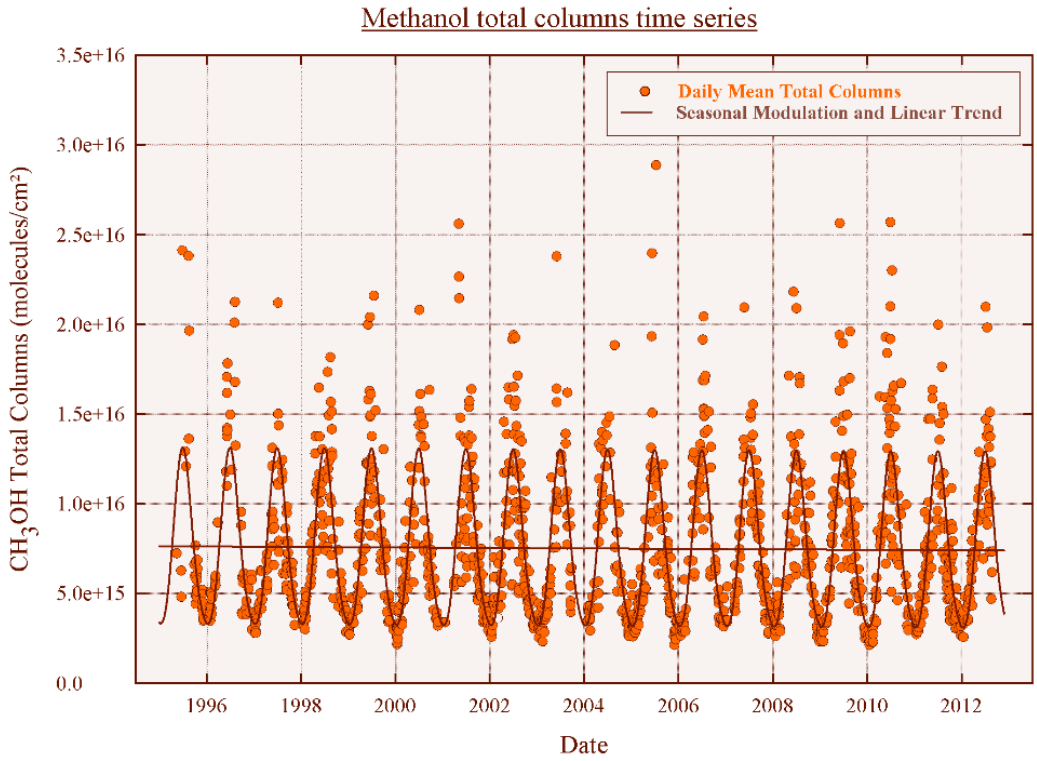

Figure 4.3. Daily mean total (orange circles) column time series of CH_3OH above Jungfraujoch. Brown curves show the linear and seasonal trend components computed with the bootstrap resampling method (Gardiner et al., 2008).

4.2.4.2. Time series and long-term trend

In order to produce the first long-term time series of atmospheric methanol above Jungfraujoch, three criteria were used to reject noisy measurements or weak absorption: (i) when negative methanol mixing ratios are retrieved; (ii) when RMS (root mean square, difference between calculated and observed absorption) was out of the interval defined by the 95 % level of confidence (2σ); (iii) when the number of iterations reached the fixed maximum. After implementation of these criteria, the total number of valid measurements is 4271 obtained on 1476 days of measurements between 1995 and 2012. For the trend calculations, we used the statistical tool developed by *Gardiner et al.* [2008] that employs a bootstrap resampling method. The function fitted to the time series is a combination of a linear component and a 3rd order Fourier series, i.e.:

$$F(t,b) = c_0 + c(t-t_0) + b_1\, cos\, 2\pi(t-t_0) + b_2\, sin\, 2\pi(t-t_0) + b_3\, cos\, 4\pi(t-t_0) + b_4\, sin\, 4\pi(t-t_0) + b_5\, cos\, 6\pi(t-t_0) + b_6\, sin\, 6\pi(t-t_0) \quad (4.1)$$

where c_0 is the abundance at the reference time t_0 for the linear component (seasonalised data), and c is the annual trend. Figure 4.3 shows the whole times series of daily mean methanol total columns above Jungfraujoch. We evaluated the trend of methanol total columns over the 1995–2012 time period and found a yearly negative trend of (-1.34 ± 2.71) x 10^{13} molecules.cm^{-2} or -0.18 ± 0.36 % (2σ), i.e. a non-significant trend at this level of confidence, which is consistent with the trend computed by *Rinsland et al.* [2009]. A non-significant trend has been computed also for both partial column subsets. Hence the results indicate a long-term trend which is not statistically significant and a strong seasonal variation.

4.2.4.3. Methanol seasonal modulation

As the results for the full time series do not indicate a statistically significant trend, we illustrate in Figure 4.4 the daily mean total columns over a 1-year time base. The strong seasonal modulation of methanol is characterized by minimum values and variability in December to February and maximum columns in June–July. The methanol maximum in summer indicated by our results is consistent with the maximum observed for free tropospheric methanol above Kitt Peak [*Rinsland et al.*, 2009] and the analysis of IASI tropospheric measurements over Europe [*Razavi et al.*, 2011]. The mean peak-to-peak amplitude of a seasonal cycle computed by Gardiner's tool and expressed as a percentage of the corresponding CH3OH yearly mean column amounts to 130.1 ± 1.6 % (1σ), while the seasonal modulation above Kitt Peak amounts to 64.6 ± 0.1 % showing a similar amplitude with the IASI measurements [*Razavi et al.*, 2011] for subtropical regions.

The IMAGESv2 model estimates a seasonal modulation of methanol in phase with the one we measured, but underestimates the peak-to-peak amplitude with 88.6 ± 1.3 % and 70.4 ± 1.2 % for "IASI" and "MEGAN" respectively. The MEGAN emission fluxes are dependent on temperature, visible ration fluxes, leaf area index and leaf age, and they show a pronounced seasonal variation at mid-latitudes, with peak values in early summer. The IASI-derived emissions peak somewhat earlier than in the MEGAN inventory, a result consistent with modelling studies using TES methanol data [*Cady-Pereira et al.*, 2012; *Wells et al.*, 2012] as well as with other studies based on in situ concentration measurements [*Jacob*, 2005] or on flux measurements [*Laffineur et al.*, 2012], which showed substantially higher methanol emission rates by young leaves compared to mature or senescent leaves.

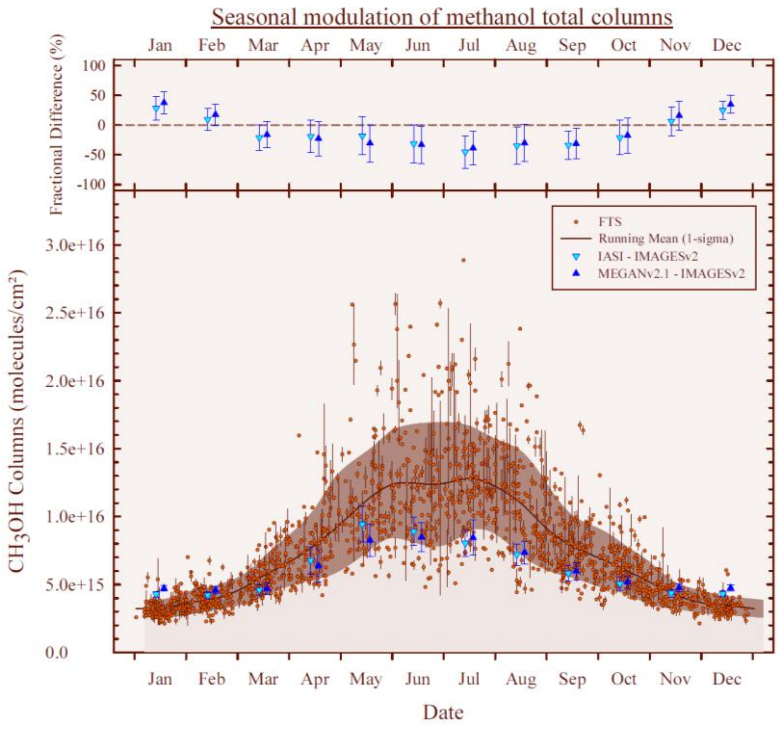

Figure 4.4. Seasonal modulation of methanol total columns. Dots with vertical lines represent the daily mean total columns over a 1-year time base and their associated standard deviation. The brown curve corresponds to a running mean fit to all data points, with a 15-day step and a 2-month wide integration time. The area corresponds to the 1_ standard deviation associated to the running mean curve. Up and down blue triangles are the monthly means of the model IMAGESv2 simulations for MEGAN and IASI respectively. Upper frame shows monthly fractional difference between FTIR results and IMAGESv2 simulations.

No systematic bias is observed on the whole time series, but a seasonal bias is characterized (see Figure 4.4): the maximum fractional difference {(IMAGES - FTIR) / [(IMAGES + FTIR) / 2]} between monthly mean results from FTIR measurements and both "IASI" and "MEGAN" simulations is found to occur in July, with -45 ± 27 % and -39 ± 28 %, respectively. The minimum fractional difference amounts to 28 ± 20 % and 38 ± 19 % respectively in January and shows an overestimation of methanol during wintertime by the IMAGESv2 model. The underestimation of methanol by the "IASI" simulation during summertime is unexpected, since this simulation reproduced very well the methanol total columns measured by IASI over Western Europe [Figure 5 in *Stavrakou et al.*, 2011]. Noting that ISSJ does not sample the lower troposphere below 3.58 km altitude, this discrepancy might reflect an overestimation of the simulated vertical gradient of methanol mixing ratios at continental mid-latitudes, which is suggested by comparisons with aircraft campaigns in spring and summer over the United States [*Stavrakou et al.*, 2011]. It is not clear, however, why this issue does not also lead to a similar model underestimation of the methanol column above ISSJ in spring. The overestimated gradient in IMAGES may be due to a well-known problem in chemical transport models, i.e. the overestimation of the hydroxyl radical concentration in the Northern Hemisphere [*Krol and Lelieveld*, 2003]. It could also be related to the large uncertainties in the ocean/atmosphere flux of methanol, given that even the sign of this flux is not well constrained [*Millet et al.*, 2008], and since IASI data were not considered sufficiently reliable over the ocean in the optimization of emissions using IMAGES by *Stavrakou et al.* [2011].

4.2.4.4. Methanol diurnal variation

The variation of the methanol abundance throughout the day has also been characterized on Figure 4.5. To this end, we extended the targeted range of solar zenith angle (SZA) going from 30° to 85° and selected only those whose retrieval provided a DOFS of at least 1. Due to the large seasonal variation, we divided our measurements into three subsets corresponding to summer (June, July, August), winter Figure 4.5. Methanol diurnal variation. Total columns versus the solar zenith angle for winter, summer and the rest of the year. Blue lines represent linear regressions and their corresponding standard deviation (1σ). (December, January, February) and the rest of the year. Even though we found no significant trend of methanol through the day in summer, a significant increase during winter and the rest of the year has been evaluated at 0.4 ± 0.3 and 1.1 ± 0.2 %.degree^{-1} in the morning. For the afternoon, the corresponding rates amount to -0.9 ± 0.2 and -0.5 ± 0.1 %.degree^{-1}, showing significant decreases. A rough approximation of those trends gives an increase of approximately 5.5 ± 10^{13} and 2.7 ± 10^{14} molecules cm^{-2}.h^{-1} in the morning and to a decrease of -1.6x10^{14} and -1.9x10^{14} molecules cm^{-2}.h^{-1} in the afternoon for winter and the rest of the year, respectively.

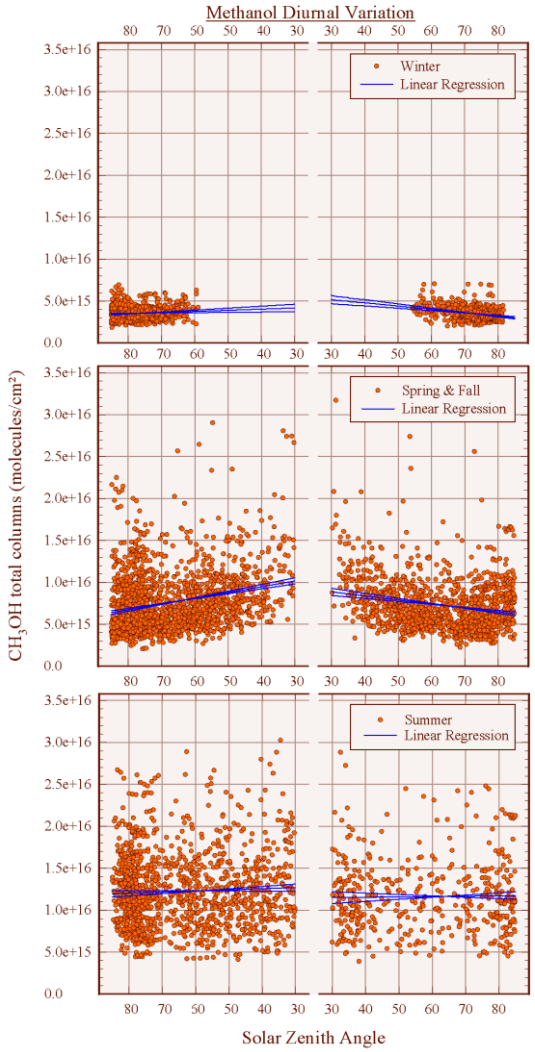

Figure 4.5. Methanol diurnal variation. Total columns versus the solar zenith angle for winter, summer and the rest of the year. Blue lines represent linear regressions and their corresponding standard deviation (1σ).

The causes for the observed diurnal variation are not clear. Major methanol sources such as biogenic production by living plants and photochemical production are stronger during daytime, due to the key role played by solar radiation in photosynthesis and other biotic processes, as well as in the generation of OH radicals through photolytic processes [*Logan et al.*, 1981]. However, these sources are expected to peak during the summer, when the diurnal variation of the column is found to be negligible. Since the photochemical sink of methanol (i.e. reaction with OH) is strongest during the day, the observed diurnal variation (and absence thereof during summer) could result from the variable balance between sources and sinks. However, OH fields, produced by the GEOS-CHEM model [*Bey et al.*, 2001] have been examined and no direct correlation with our methanol total columns has been found. Moreover, since the IMAGES model includes those processes but still fails to reproduce the observed diurnal variation, it appears likely that other factors play a significant role, e.g. orography-induced wind patterns bringing boundary layer air to the free troposphere above the station's altitude. Besides model simulations, in situ measurements have also been explored. However, the existing data sets being "campaign-type", the statistics are too weak to draw clear conclusions on this subject. More efforts should be put in further research on processes governing the methanol diurnal variation.

4.2.4.5. Methanol in the lower troposphere

In Figure 4.6, our lower tropospheric columns show a seasonal modulation with characteristics close to the seasonal variation of total columns with similar occurrence of maximum and minimum but a wider peak-to-peak amplitude of 168 ± 3 %. The upper panel of Figure 4.6 also shows monthly fractional differences between the FTIR results and both simulations from the IMAGESv2 model [*Stavrakou et al.*, 2011] as well as seasonal differences with in situ measurements performed at the Jungfraujoch [*Legreid et al.*, 2008].

Neither of the IMAGESv2 series stands out, since they both underestimate the peak-to-peak amplitude with 78 ± 2 % and 101 ± 2 % for MEGAN and IASI, respectively. For both series, methanol is overestimated in winter (DJF) and shows a good agreement in spring (MAM) as well as in October and November. During summertime, results during July are significantly underestimated but the difference for the remaining 3 months (June, August and September) is close to non-significant.

The seasonal amplitude shows a good agreement on the data dispersion (see error bars) except for the autumn season with more compact values. The high standard deviation in summer appears to be due to only a few days with high methanol mixing ratios. These days are characterized by trajectories originating from the south, where biogenic sources are more active. Indeed, it has been established by *Legreid et al.* [2008], that there is a considerable contribution of methanol from the south since methanol is emitted in large amounts from biogenic sources [*Singh et al.*, 1994; *Jacob*, 2002, 2005; *Fall*, 2003] more active in the south of the Alps than in the north. Furthermore, air masses from the south are transported over Northern Italy, which is a highly industrialized area with considerable anthropogenic emissions.

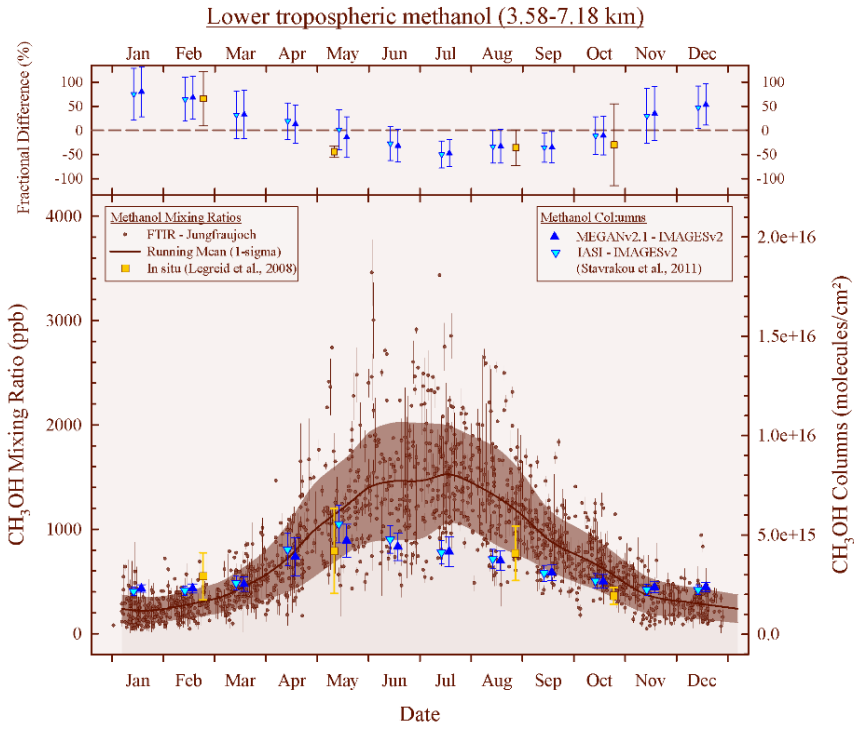

Figure 4.6. Lower-tropospheric methanol (3.58–7.18 km). Dots with vertical lines represent the daily mean lower-tropospheric columns over a 1-year time base and their associated standard deviation. The brown curve corresponds to a running mean fit to all data points, with a 15-day step and a 2-month wide integration time. The area corresponds to the 1σ standard deviation associated to the running mean curve. Up and down blue triangles are monthly means of the model IMAGESv2 simulations for MEGAN and IASI respectively [*Stavrakou et al.*, 2011]. *Yellow squares are seasonal means of methanol in situ measurements* [*Legreid et al.*, 2008]. *The upper panel shows monthly fractional difference between the FTIR results and IMAGESv2 simulations and seasonal fraction difference with in situ measurements.*

4.2.4.6. Methanol in the upper troposphere–lower stratosphere (UTLS)

The comparison between the UTLS FTIR columns, both IMAGES data sets and monthly mean results from ACE-FTS occultations illustrated in Figure 4.7 shows an overall agreement within the estimated uncertainties. As for total and lower-tropospheric columns, methanol variability is underestimated by the IMAGESv2 model. On the other hand, the seasonal cycle of methanol UTLS columns is satisfactorily characterized by FTIR results and the IMAGES simulations in terms of absolute value with a non-significant mean fractional difference with FTIR of -6 ± 49 % and 1 ± 48 %, respectively for MEGAN and IASI. The peak-to-peak amplitudes of the three series, i.e. 93 ± 2 % for FTIR, 82 ± 2 % for MEGAN and 92 ± 2 % for IASI are in very good agreement as well as the timing of the maximum (June–July).

A close to statistical agreement is observed between Jungfraujoch results and the UTLS columns derived from ACE-FTS data with a mean fractional difference of 33 ± 30 % despite substantially higher ACE methanol columns in March and May. The differences for these 2 months may be attributed to the fact that the monthly mean results from ACE-FTS encompass a 10° latitudinal band and therefore occultations may be capturing local events such as plumes from biomass burning out of range for the Jungfraujoch station.

Biases in the ACE methanol retrievals have recently been addressed by [*Harrison et al.*, 2012]. Adoption of a new set of infrared absorption cross sections for methanol led to the determination of ACE UTLS columns higher by up to 25 % [calculations based two occultations; see Figure 4.6 of Harrison et al., 2012], depending on the temperature of the measurement. Therefore, by applying those new cross sections to our Jungfraujoch retrievals, we would likely identify a bias in the same range, depending on the season and thus the vertical temperature distribution. The effect on total (and partial) columns will have to be evaluated on the basis of larger statistics for each season and using the new cross sections of *Harrison et al.* [2012].

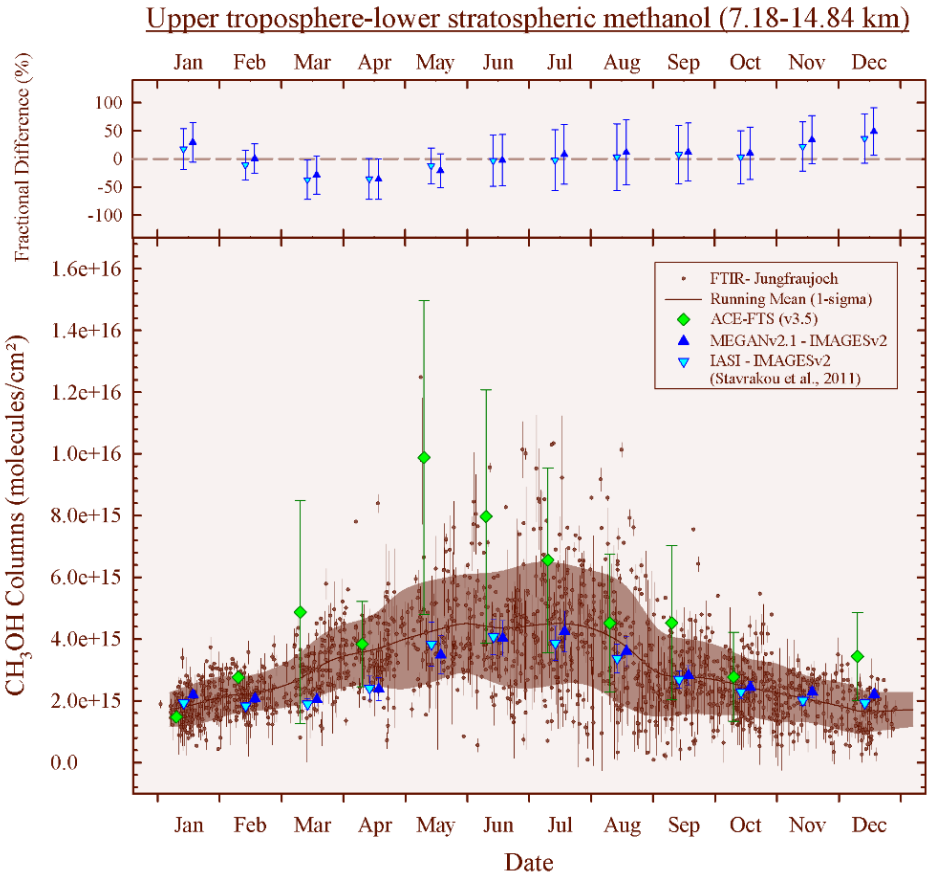

Figure 4.7. Upper troposphere–lower stratospheric methanol (7.18–14.84 km). Dots with vertical lines representing daily mean lower-tropospheric columns over a 1-year time base and their associated standard deviation. The brown curve corresponds to a running mean fit to all data points, with a 15-day step and a 2-month wide integration time. The area corresponds to the 1σ standard deviation associated to the running mean curve. Up and down blue triangles are the monthly means of the model IMAGESv2 simulations for MEGAN and IASI respectively (Stavrakou et al., 2011). Green diamonds are the monthly means of methanol retrieved from ACE-FTS occultations with the error bars representing the standard deviation (2σ). Upper frame show monthly fractional difference between FTIR results and IMAGESv2 simulations and ACE-FTS results.

4.2.5. Conclusions

A long-term time series of methanol has been determined from the analysis of a 17-year time series of infrared solar absorption spectra recorded with a commercial Fourier transform spectrometer Bruker IFS120HR, operated at the high-altitude International Scientific Station of the Jungfraujoch [ISSJ, Swiss Alps, 45° N, 8.0° E, 3580 m a.s.l.; *Zander et al.*, 2008] providing a valuable tool for model and satellite validation and complementing the NDACC measurements at northern mid-latitudes.

The results were analyzed using the SFIT-2 v3.91 fitting algorithm and thanks to the combination of spectral windows used in previous studies for the retrieval of methanol from FTS spectra [*Dufour et al.*, 2007; *Rinsland et al.*, 2009; *Vigouroux et al.*, 2012], we have significantly improved the information content. With a typical DOFS of 1.82, a total column and two partial columns time series are available, i.e. a lower-tropospheric (LT, 3.58-7.18 km) and an upper tropospheric– lower stratospheric one (UTLS, 7.18-14.84 km). Both random and systematic error sources have been identified and characterized using the spectra recorded in the year 2010, and are found to be respectively 5 and 7 % for the total column.

The analysis of the time series does not reveal a significant long-term trend but shows a high peak-to-peak amplitude of the seasonal cycle of 129.4 ± 5.5 % (1σ) for total columns. Methanol total and partial columns are characterized by a strong seasonal modulation with minimum values and variability in December to February and maximum columns in June–July. First analysis of methanol diurnal variation shows an increase of methanol in the morning and a decrease during the afternoon for all seasons but summer.

Comparisons with methanol measurements obtained with other techniques (in situ and satellite) give satisfactory results. The FTIR lower tropospheric data compared to in situ measurements generally shows a good agreement regarding the data dispersion. Concerning the UTLS partial columns, there is a close to statistical agreement with ACE-FTS occultations despite higher ACE columns of methanol in March and May.

The IMAGESv2 simulations underestimate the peak-to-peak amplitude for total and lower-tropospheric columns. Despite the absence of a systematic bias between our results and the IMAGESv2 simulations, comparisons show seasonal differences with an overestimation of winter methanol and an underestimation during summertime, which might be explained by an overestimation of the vertical gradient of methanol mixing ratios by the model. Regarding UTLS columns, the peak-to-peak amplitude and timing of the maximum (June–July) in both IMAGESv2 simulations are in very good agreement with the FTIR results.

Even though the role of plant growth in methanol budget is confirmed by its seasonality, large uncertainties remain in the methanol budget. Thanks to the improvement of the information content of our retrieval and therefore our vertical resolution, our partial column time series should contribute to better constraints for model simulations and therefore may lead to a better understanding of methanol budget.

Chapter 5 – Ethane

Chapter 5 − Ethane

5.1. Introduction

Through this work, I contributed to *Franco et al.*, [2015a] by developing and optimizing the strategy for inversion of ethane from FTIR observations recorded at the Jungfraujoch station. The development of the retrieval strategy includes the testing of 110 retrieval strategies in order to evaluate the best combination of parameters (see Table 5.0). By combining 3 micro-windows for the first time for Jungfraujoch and by including improved spectroscopic parameters such as C_2H_6 pseudo-lines [*Harrison et al.*, 2010] and updated line parameters for methyl chloride [*Bray et al.*, 2011, 2012] and ozone, we achieved a mean DOFS of 2.11 ± 0.27 which represents a significant improvement compared to previous works carried out at ISSJ, with typical DOFS of about 1.5. Selection of the best retrieval strategy has been performed on the basis of minimum residuals, maximum DOFS and realistic retrieved profiles (i.e. no ungeophysical negative mixing ratio values). Finer and careful comparisons of eigenvectors and eigenvalues have been performed when simple residuals/DOFS analysis was not sufficient to select among the tested strategies.

Parameter	Number of tests
Windows limits and combination	7
Windows, interfering species to retrieve	18
Spectroscopic linelist	25
Signal-to-noise ratio for inversion	10
C_2H_6 a priori distribution	9
Water vapor	5
Total	**74**

Table 5.0. Overview of tests performed for the optimization of the methanol retrieval strategy for Jungfraujoch.

The limits of each window have been refined based on previous work [*Mahieu et al.*, 1997; *Notholt et al.*, 1997; *Rinsland et al.*, 2000; *Zhao*, 2002; *Meier et al.*, 2004; *Gardiner et al.*, 2008; *Paton-Walsh et al.*, 2010; *Angelbratt et al.*, 2011; *Vigouroux et al.*, 2012] and the combination of those three windows has been tested for the first time for Jungfraujoch observations. Moreover, careful identification of interfering species that contribute to the absorption spectrum has been performed. We settled to five interfering species including CH_3Cl, O_3, CH_4, H_2O, and C_2H_6 as illustrated in Figure 5.0.1.

Improved spectroscopic parameters have been included in our retrieval strategy and the impact of each set of spectroscopic parameters on residuals has been quantified for each window individually and for each combination of window through this paper (see Figure 5.2).

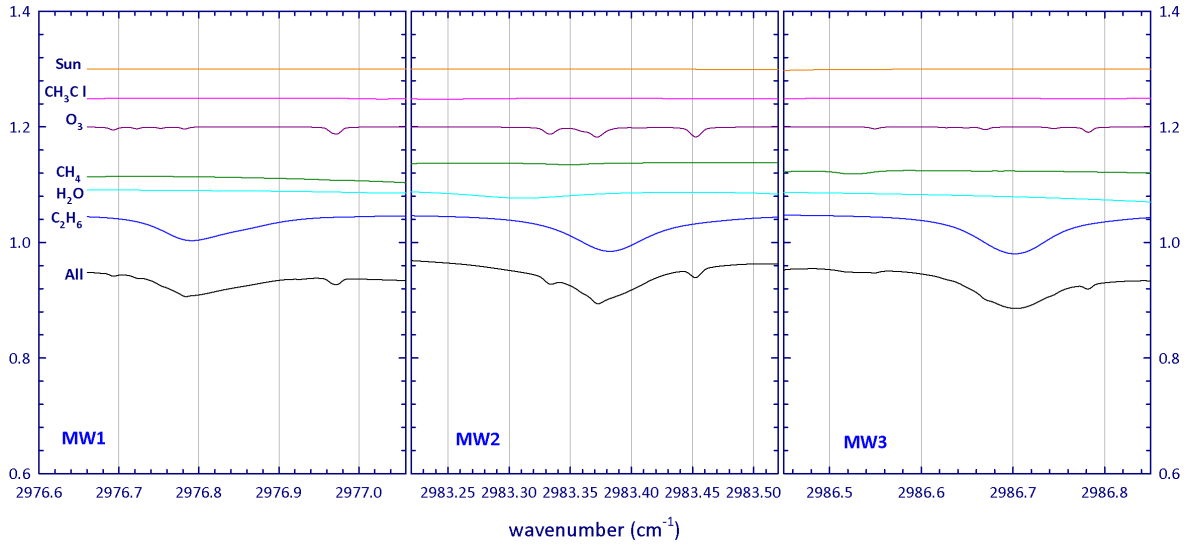

Figure 5.0.1. Simulation for Jungfraujoch, 60° zenith angle, 6.1 mK. For the three windows, we display the synthetic spectra for individual contributors (see color codes). HITRAN 2008 and averaged mixing ratio profiles based on the WACCM model climatology have been used for the simulations. For clarity, the contributions of each species have been vertically shifted.

Numerous a priori vertical distribution built from satellite observations, in situ GCMS surface measurements and CTMs and interpolated on the layering scheme adopted for Jungfraujoch retrievals were tested. They included a zonal mean (for the 41−51°N latitude band) of 771 occultations recorded by the ACE-FTS instrument [*Bernath et al.*, 2005] between the 2nd of November in 2004 and the 8th of February in 2011 extending from 8.5 to 20 km with an extension down to 3.58 km based on EMEP in situ gas chromatography surface measurements at the Rigi station (47.07 °N, 8.45 °E, 1031 m a.s.l., at a distance of 68 km from the Jungfraujoch station) and an upper extension up to 100 km from the WACCM model climatology [*Chang et al.*, 2008]. Simulations from CTMs to build a priori ethane vertical distribution included:

− simulations over the 1980–2020 time period from WACCMv5 and WACCMv6 climatology,
− daily mean C_2H_6 profiles over the 2007−2009 time period from the CHASER model [*Sudo*, 2002],
− hourly C_2H_6 profiles over the year 2005 from a Norwegian CTM developed at the university of Oslo [version 2 and version 3; *Berntsen and Isaksen*, 1997],
− daily mean C_2H_6 profiles over the 2007-2009 time period from the GEOS-Chem model [*Bey et al.*, 2001].

From careful analysis of retrieved profiles in addition to analysis of residuals, information content, and vertical sensitivity, we selected the use of a priori issued from the model CHASER in the framework of an optimized retrieval strategy of ethane for Jungfraujoch as presented in the next section. However, it has been determined that to ensure consistency between FTIR NDACC measurement stations, we will opt for a scaled version of the latest WACCM simulation (i.e. version 6) for a priori distribution of ethane for each site. The scaling factor applied to the WACCM profile will be determined from the CHASER simulation depending on the considered station.

Other parameters have been examined and included in the retrieval strategy such as the signal-to-noise ratio for inversion. Moreover, the pre-fitting of water vapor profiles has been considered in order to provide pre-adjusted water vapor profiles to the actual retrieval strategy. Indeed, water vapor captures 78.9, 78.3 and 78.03 % of the IR radiation in the MW1, MW2 and MW3 windows respectively and need to be carefully considered. However, the pre-adjustment of water vapor profiles has been discarded since it did not provide satisfactory improvement of residuals and information content while it considerably increased computing time. The situation is however not as favorable for low-altitude and/or humid NDACC sites which will likely have to include this pre-fit.

5.2. Retrieval of ethane from ground-based FTIR solar spectra using improved spectroscopy: recent burden increase above Jungfraujoch

B. Franco[1], F., W. Bader[1], G. C. Toon[2], C. Bray[3], A. Perrin[4], E. V. Fischer[5], K. Sudo[6,7], C. D. Boone[8], B. Bovy[1], B. Lejeune[1], C. Servais[1], E. Mahieu[1]

[1] Institute of Astrophysics and Geophysics, University of Liège, B -4000 Liège (Sart-Tilman), Belgium
[2] Jet Propulsion Laboratory, California Institute of Technology, Pasadena California, 91109, USA
[3] CEA, DEN, DPC, F-91191 Gif-sur-Yvette, France
[4] Laboratoire Interuniversitaire des Systèmes Atmosphériques (LISA-UMR7583) CNRS, Universités Paris Est Créteil and Paris Diderot (IPSL), F-94010 Créteil cedex, France
[5] Department of Atmospheric Science, Colorado State University, Fort Collins, CO USA
[6] Graduate School of Environmental Studies, Nagoya University, Nagoya, Japan
[7] Department of Environmental Geochemical Cycle Research, Japan Agency for Marine-Earth Science and Technology, Yokohama, Japan
[8] Department of Chemistry, University of Waterloo, Ontario, Canada

Received: 11 December 2014 − Received in revised form: 12 March 2015 − Accepted: 13 March 2015
Published in Journal of Quantitative Spectroscopy & Radiative Transfer: 20 March 2015

Edited by: L. Rothman

Abstract

An improved spectroscopy is used to implement and optimize the retrieval strategy of ethane (C_2H_6) from ground-based Fourier Transform Infrared (FTIR) solar spectra recorded at the high-altitude station of Jungfraujoch (Swiss Alps, 46.5°N, 8.0°E, 3580 m a.s.l.). The improved spectroscopic parameters include C_2H_6 pseudo-lines in the 2720−3100 cm^{-1} range and updated line parameters for methyl chloride and ozone. These improved spectroscopic parameters allow for substantial reduction of the fitting residuals as well as enhanced information content. They also contribute to limiting oscillations responsible for ungeophysical negative mixing ratio profiles. This strategy has been successfully applied to the Jungfraujoch solar spectra available from 1994 onwards. The resulting time series is compared with C_2H_6 total columns simulated by the state-of-the-art chemical transport model GEOS-Chem. Despite very

consistent seasonal cycles between both data sets, a negative systematic bias relative to the FTIR observations suggests that C_2H_6 emissions are underestimated in the current inventories implemented in GEOS-Chem. Finally, C_2H_6 trends are derived from the FTIR time series, revealing a statistically significant sharp increase of the C_2H_6 burden in the remote atmosphere above Jungfraujoch since 2009. Evaluating cause of this change in the C_2H_6 burden, which may be related to the recent massive growth of shale gas exploitation in North America, is of primary importance for atmospheric composition and air quality in the Northern Hemisphere.

5.2.1. Introduction

Ethane (C_2H_6) is the most abundant non-methane hydrocarbon in the Earth's atmosphere with a lifetime of approximately months [*Rudolph*, 1995]. On a global scale, the main sources of C_2H_6 are leakage from the production, transport of natural gas loss (62 %), biofuel consumption (20 %) and biomass burning (18 %), mainly located in the Northern Hemisphere [*Logan et al.*, 1981; *Rudolph*, 1995; *Xiao et al.*, 2008]. Biogenic and oceanic sources are generally very small [*Rudolph*, 1995]. The main sink of C_2H_6 in the troposphere is oxidation via reaction with hydroxyl radicals (OH), while in the stratosphere reaction with chlorine atoms dominates [*Aikin et al.*, 1982].

Ethane has a large impact on tropospheric composition and impacts the distribution of ozone (O_3) through several pathways, making it a compound of great interest as a sensitive indicator of tropospheric pollution and transport [*Rinsland et al.*, 2002]. By acting as a major sink for tropospheric OH, the abundance of C_2H_6 impacts the lifetime of methane (CH_4). Thus C_2H_6 is an indirect greenhouse gas with a net global warming potential of 5.5 [100 year horizon; *Collins et al.*, 2002]. Similarly, C_2H_6 influences the atmospheric content of carbon monoxide [CO; *Aikin et al.*, 1982]. Ethane also has a significant impact on air quality as it is an important source of peroxyacetyl nitrate (PAN), a thermally unstable reservoir for nitrogen oxide radicals [NO_x; *Rudolph*, 1995; *Fischer et al.*, 2014]. By providing the main NO_x source in many regions of the atmosphere, PAN has a major effect on the production and loss of O_3.

Atmospheric C_2H_6 abundances can be measured using various techniques. Previous measurements of C_2H_6 include Fourier Transform InfraRed (FTIR) spectrometer observations by the balloon-borne Jet Propulsion Laboratory MkIV Interferometer [*Toon*, 1991], aircraft air samples collected during the NASA's Global Tropospheric Experiment Field Missions Pacific Exploratory Mission [e.g., PEM-West A; *Blake et al.*, 1996 and TRACE-A; *Fishman et al.*, 1996; *Chatfield et al.*, 1998], solar occultations recorded by the Atmospheric Chemistry Experiment-Fourier Transform Spectrometer [ACE-FTS; *Rinsland*, 2005], ground-based measurements by gas chromatograph [e.g.: *Browell*, 2003; *Swanson*, 2003; *Wingenter et al.*, 2005] and finally limb-scans performed by the Michelson Interferometer for Passive Atmospheric Sounding (MIPAS) onboard the European ENVIronmental SATellite [ENVISAT; *Glatthor, N. et al.*, 2009]. Analysis of these data records has significantly increased our understanding of the long range transport of C_2H_6.

Ethane has also been measured by ground-based FTIR technique at several latitudes in both hemispheres, covering different time periods [e.g.: *Rinsland, C. P. et al.*, 1998; *Rinsland et al.*, 1999, 2000, 2002; *Zhao*, 2002; *Gardiner et al.*, 2008; *Angelbratt et al.*, 2011; *Vigouroux et al.*, 2012; *Viatte et al.*, 2014].

Nevertheless, strong latitudinal, seasonal and local fluctuations on small spatial and temporal scales make C_2H_6 secular trend determination difficult from the existing observations. Indeed, its concentration in the atmosphere is largely influenced by strong vertical mixing and dilution with background air during transport from emission sources.

In this paper, we present a 20-year long-term time series of C_2H_6 derived from ground based high-resolution infrared solar spectra recorded with a Bruker 120HR FTIR spectrometer operated under clear sky conditions at the high-altitude International Scientific Station of the Jungfraujoch [referred to below as ISSJ; Swiss Alps, 46.5°N, 8.0°E, 3580m a.s.l.; *Zander et al.*, 2008]. Such a long-term time series in the remote atmosphere allows for air quality monitoring and provides a valuable tool for model and satellite validation. The solar spectra used here have been recorded within the framework of the Network for Detection of Atmospheric Composition Change monitoring activities (NDACC; see http://www.ndacc.org).

This work furthers the C_2H_6 dataset previously published in *Rinsland et al.*, [2000] and *Mahieu et al.*, [1997] for the ISSJ station and it presents an improved retrieval strategy in terms of reduced residuals and enhanced information content, combining three spectral domains for the first time at ISSJ. A careful selection of the available spectroscopic datasets is performed in order to minimize the fitting residuals. A thorough discussion of the retrieval strategy and data characterization (information content and error budget) is presented here along with trend analysis and preliminary comparison with the three-dimensional state-of-the-art global chemical transport model (CTM) GEOS-Chem.

This paper is organized as follows. A detailed description of the optimized retrieval strategy is given in Section 5.2.2. Section 5.2.3 reports the characterization of the FTIR geophysical products and provides a detailed error budget. Supporting model simulations are described in Section 5.2.4. Section 5.2.5 presents a preliminary comparison between FTIR and GEOS-Chem seasonal cycles of the C_2H_6 burden above Jungfraujoch as well as the entire 1994−2014 time series of daily-mean total columns and corresponding trends. Section 5.2.6 concludes this study with a short summary and discussions of the results, identifying avenues for future work.

5.2.2. FTIR data set

5.2.2.1. Instrumental setup

All the spectra analyzed here have been recorded at ISSJ, located in the Swiss Alps at 3580m altitude on the saddle between the Jungfrau (4158m a.s.l.) and the Mönch (4107m a.s.l.) summits. This station offers excellent conditions to perform solar observations, particularly in the infrared, because of weak local pollution (no major industries within 20 km) and very high dryness thanks to the high-altitude and the presence of the Aletsch Glacier. Indeed, the amount of water vapor (H_2O), a strong interference in the infrared, is at least twenty times lower than at sea level. Due to these factors, the ISSJ station allows for investigating the atmospheric background conditions over central Europe and the mixing of air masses from planetary boundary layer and free troposphere [e.g.: *Zellweger et al.*, 2003; *Reimann*, 2004].

Here we use observations performed with a commercial Bruker IFS-120HR instrument [*Zander et al.*, 2008]. This spectrometer, affiliated to the NDACC network since 1991, is equipped with HgCdTe and InSb cooled detectors covering the 650-4500 cm^{-1} region of the electromagnetic spectrum.

The Bruker observational database investigated in the present study consists of more than 11 500 spectra recorded between September 1994 and August 2014 with an optical filter covering the 2400 to 3100 cm^{-1} range encompassing the perpendicular v7 fundamental stretching band of C_2H_6. Spectral resolutions, defined as the reciprocal of twice the maximum optical path difference, alternate between 0.004 and 0.006 cm^{-1}. The signal-to-noise (S/N) ratio varies between 300 and 4500 (average spectra resulting from several successive individual Bruker scans, when solar zenith angles vary slowly). The optimization of the retrieval strategy has been based on a subset of about 600 spectra during 2003.

5.2.2.2. Retrieval strategy

The C_2H_6 column retrievals and profile inversions have been performed using the SFIT-2 v3.91 fitting algorithm. This retrieval code has been specifically developed to derive mixing ratio profiles of atmospheric species from ground-based FTIR spectra [*Rinsland, C. P. et al.*, 1998]. It is based on the semi-empirical implementation of the Optimal Estimation Method (OEM) developed as in [*Rodgers*, 1990]. Vertical profiles are derived from simultaneous fits to one or more spectral intervals of at least one solar spectrum with a multilayer, line-by-line calculation that assumes a Voigt line shape [*Drayson*, 1976].

For the first time at ISSJ, C_2H_6 retrievals have been carried out using three micro windows simultaneously (see Table 5.1). The first micro-window (MW1) is centered on the well-known strong and sharp $^PQ_3$ sub-branch of the perpendicular v7 fundamental stretching band [*Pine and Rinsland*, 1999] and extends from 2976.660 to 2977.059 cm^{-1}. This $^PQ_3$-MW1 is the only one taken into account previously for the Jungfraujoch station [*Mahieu et al.*, 1997; *Rinsland et al.*, 2000] and at many other FTIR sites [e.g.: *Zhao*, 2002; *Gardiner et al.*, 2008; *Paton-Walsh et al.*, 2010; *Angelbratt et al.*, 2011]. The second micro-window (MW2) includes the $^PQ_1$ sub-branch around 2983.3 cm^{-1}, as suggested in [*Meier et al.*, 2004] and used in [*Vigouroux et al.*, 2012] in combination with MW1, and extends from 2983.200 to 2983.500 cm^{-1}. Finally, a third micro-window (MW3) encompasses the $^RQ_0$ C_2H_6 sub-branch around 2986.7 cm^{-1}, extending from 2986.450 to 2986.850 cm^{-1}. The MW3 has only been fitted at dry high-latitude sites [*Notholt et al.*, 1997; *Viatte et al.*, 2014] because of strong H_2O interferences. Within these micro-windows, the major interfering species whose vertical profiles are scaled during the retrieval process are CH_4, H_2O, O_3 and methyl chloride (CH_3Cl).

Micro-windows (cm^{-1})	Interfering species
2976.660–2977.059	H_2O, O_3, CH_3Cl, CH_4
2983.200–2983.500	H_2O, O_3, CH_3Cl, CH_4
2986.450–2986.850	H_2O, O_3, CH_3Cl, CH_4

Table 5.1. List of the micro-windows used for the FTIR retrieval of C_2H_6 at Jungfraujoch and the interfering species taken into account. Simple scaling of the corresponding vertical profiles of the interfering species is allowed throughout the iterative retrieval process.

The model atmosphere adopted above the altitude of the ISSJ station consists of a 39-layer scheme extending from 3.58 km up to 100 km with progressively increasing thicknesses. The pressure-temperature profiles are provided by the National Centers for Environmental Prediction (NCEP, Washington DC, USA, http://www.ncep.noaa.gov/) while the solar line compilation supplied by [*Hase et al.*, 2006] has been assumed for the non-telluric absorptions.

The C_2H_6 a priori mixing ratio profile corresponds to a mean of a 2007−2009 CHASER [Chemical AGCM for Study of atmospheric Environment and Radiative forcing; *Sudo*, 2002] simulation (Figure 5.1.a; see Sect. 5.2.4.1). A priori profiles for all interfering molecules are based on the 1980−2020 simulation of the WACCM model [version of WACCM profiles; the Whole Atmosphere Community Climate Model; e.g., *Chang et al.*, 2008] for the ISSJ station.

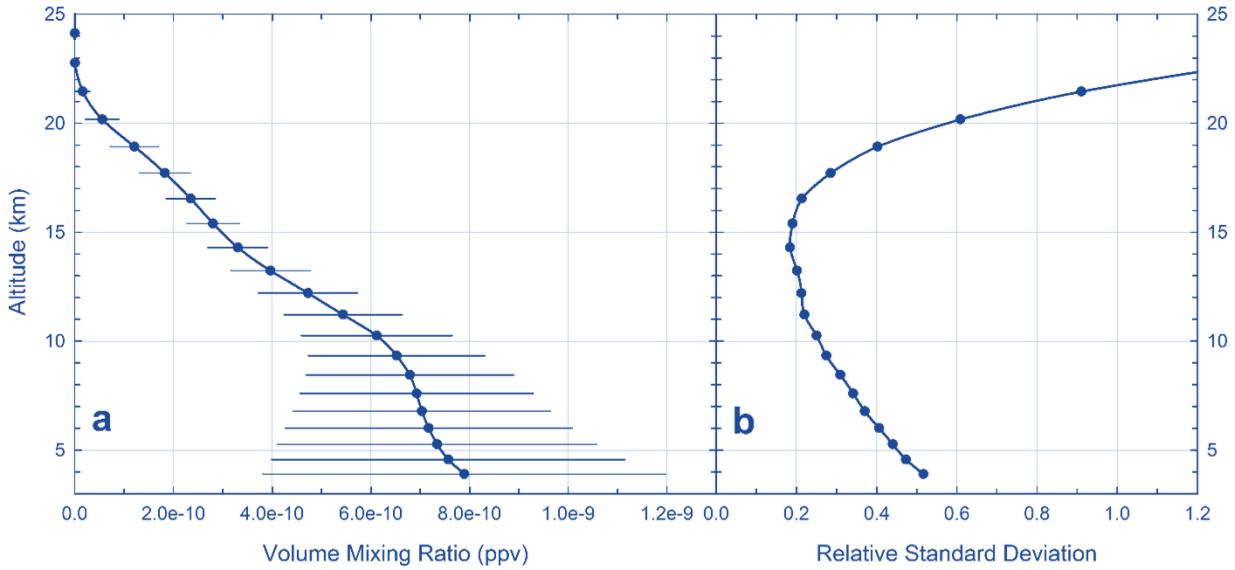

Figure 5.1. (a) C_2H_6 a prioriprofilewith1-σ standard deviation derived from a 2007–2009 CHASER simulation used for the FTIR retrievals at Jungfraujoch. (b) Averaged relative standard deviation of C_2H_6 VMR derived from the same CHASER simulation and used as diagonal elements of the covariance matrix for the FTIR retrievals.

In a usual OEM, the covariance matrix should reject the natural variability of the target gas profile [*Rodgers*, 2003]. It is specified for each layer as a percentage of the a priori profile and an ad hoc correlation length, which is interpreted as a correlation between layers decaying along a Gaussian. For C_2H_6, we have adopted the relative standard deviation profile derived from the CHASER results (Figure 5.1b) as the diagonal values of the covariance matrix and a Gaussian inter-layer correlation with a half-width length of km for extra diagonal elements of the covariance matrix.

It is worth noting that this C_2H_6 retrieval strategy has been optimized in such a way to limit the fraction of retrieved profiles presenting negative mixing ratios. By setting up an inter-layer correlation of 4 km and the S/N ratio for inversion at 300, the retrieved information content at Jungfraujoch is slightly constrained deliberately but the retrieval process is stabilized and strong oscillations in the lower levels of the retrieved

profiles are avoided. This way, less than 9 % of solar spectra have been rejected because of ungeophysical retrieved mixing ratio values. Moreover, statistics have shown that there is no correlation between the seasonality and the fraction of rejected solar spectra. Hence we ensure here homogeneous data coverage and sampling throughout the entire time series (see Section 5.2.5.2).

5.2.2.3. Spectroscopy

Ethane has a complicated spectrum with 12 interacting normal vibration modes, which makes it difficult to accurately predict the spectrum. Therefore, it is essential to take a closer look at the spectroscopic parameters. First C_2H_6 line parameters go back to the work of *Pine and Lafferty*, [1981] with the assignment of C_2H_6 transitions but no ^PQ-branches were included. In 1987, to support the Atmospheric Trace Molecule Spectroscopy Experiment (ATMOS), an empirical linelist for the strongest ^PQ-branches of C_2H_6 covering the 2973−3001 cm^{-1} region was developed [*Brown et al.*, 1987]. Pacific North West National Laboratory (PNNL, Washington, USA, http://nwir.pnl.gov) measured C_2H_6 cross-sections from 700 to 6500 cm^{-1} at a 0.1 cm^{-1} resolution while a quantum mechanically based linelist for the $^PQ_3$ branch at 2976 cm^{-1} was developed [*Pine and Rinsland*, 1999] and included in the HITRAN 2004 database [*Rothman et al.*, 2005]. The latest HITRAN C_2H_6 update (July 2007) contains Pine and Rinsland $^PQ_3$ branch as well as Brown's empirical linelist for the other ^PQ-branches but still lacks information for weaker absorptions features.

Quantum-mechanical analysis of the C_2H_6 spectrum remains very difficult and is still lacking, except for the $^PQ_3$ branch. The current state of C_2H_6 parameters in HITRAN 2004 and HITRAN 2008 [*Rothman et al.*, 2009] is rather unsatisfactory in the 3 µm region for all spectral features other than the $^PQ_3$ branch. A new set of C_2H_6 cross-sections was therefore developed [*Harrison et al.*, 2010], based on new high resolution IR spectra recorded with and without additional synthetic air at the Rutherford Appleton Laboratory Molecular Spectroscopy Facility (RAL, UK, http://www.stfc.ac.uk/ralspace/) using a high resolution FTIR spectrometer. These cross sections for C_2H_6 have been measured in the 3 µm spectral region and calibrated in intensity by using low resolution spectra from the PNNL IR database as a reference. Finally, [*Lattanzi et al.*, 2011] published a linelist including an improved representation of P- and R-branch lines of C_2H_6. However, based on the quality of fits to Harrison's lab spectra, it has been evaluated that the Q-branch features which we use for our retrieval strategy are poorly represented compared to HITRAN 2008, (evaluation of this linelist can be found at http://mark4sun.jpl.nasa.gov/report/Evaluation of Lattanzi C_2H_6 linelist.pdf).

In 2011, an empirical pseudo-line-list (PLL) was fitted to Harrison's C_2H_6 lab spectra (the PLL and description can be found at http://mark4sun.jpl.nasa.gov/pseudo.html). The PLL generally provides a convenient and accurate way of interpolating/extrapolating in temperature and pressure to conditions not covered by lab measurements (Harrison's measurements in the case of this study for C_2H_6). In the present work, these pseudo-lines have been combined and tested with three versions of HITRAN (i.e. 2004, 2008 and 2012; [*Rothman et al.*, 2005, 2009, 2013]).

As the 2950–3020 cm^{-1} region encompasses absorption features from many atmospheric gases, the related spectroscopic parameters need to be as complete and accurate as possible in order to best simulate the atmospheric spectra. To this end, in addition to the C_2H_6 PLL, two updates have been included in our linelist. The first one consists of an update for three O_3 lines (encompassed in MW1) provided by P. Chelin (Laboratoire de Physique Moléculaire pour l'Atmosphère et l'Astrophysique, Paris, France, Personal Communication, 2004) in the framework of the UFTIR (Time series of Upper Free Troposphere observations from a European ground-based FTIR network) project. The second update concerns the CH_3Cl line positions and line intensities for the ν_1, ν_4 and $3\nu_6$ CH_3Cl bands in the 3.4 µm region [*Bray et al.*, 2011, 2012]. Fourier transform spectra have been recorded at high resolution at the Laboratoire de Dynamique, Interactions et Réactivité in France. Measurements of line positions and line intensities have been performed for both isotopologues $^{12}CH_3{}^{35}Cl$ and $^{12}CH_3{}^{37}Cl$ in the ν_1, ν_4, $3\nu_6$ bands and line intensities have been compared to the recent 174 integrated intensities from PNNL.

Spectroscopic parameters	RMS (%)			Mean column
	MW1	MW2	MW3	(x 10^{16} molec.cm^{-2})
HITRAN 2004	0.2118	0.2974	0.5213	1.08
HITRAN 2004 + C_2H_6 PLL	0.1905	0.2283	0.1626	1.00
HITRAN 2004 + C_2H_6 PLL + O_3	0.1406	0.2283	0.1648	0.99
HITRAN 2004 + C_2H_6 PLL + O_3 + CH_3Cl	0.1158	0.2357	0.1410	1.01
HITRAN 2008	0.4705	0.1772	0.5200	1.03
HITRAN 2008 + C_2H_6 PLL	0.1329	0.1332	0.1627	0.97
HITRAN 2008 + C_2H_6 PLL + O_3	0.1316	0.1331	0.1623	0.98
HITRAN 2008 + C_2H_6 PLL + O_3 + CH_3Cl	0.1067	0.1179	0.1379	0.99
HITRAN 2012 + C_2H_6 PLL + O_3	0.1230	0.2151	0.1657	0.96

Table 5.2. Root mean square (RMS) residuals of the calculated spectra relative to observations (in %) for each micro-window when fitting are presentative subset of 229 solar spectra from the year 2003 and using different combinations of spectroscopic parameters (see first column). These residuals are displayed in Figure 5.2 for the HITRAN 2008 compilation and updates. Note that HITRAN 2004 includes the August 2006 updates and that the CH_3Cl update tested here is already part of the original HITRAN 2012 release. The averages of the resulting column values (x 10^{16} molec.cm^{-2}) are listed in the last column. A typical and representative standard deviation of 25 % is associated with these mean columns.

Table 5.2 summarizes the residuals (relative to observations) and mean retrieved columns associated with the use of the HITRAN 2004 [including the August 2006 updates; e.g., *Esposito et al.*, 2007], 2008 and 2012 compilations with the different spectroscopic improvements mentioned above. Note that the CH_3Cl update tested here is already part of the original HITRAN 2012 release. These tests have been performed on a subset of 229 representative solar spectra from the year 2003. Figure 5.2 displays mean observed and calculated spectra as well as residuals, and illustrates the improvement of residuals brought by each update compared to the initial HITRAN 2008 database. By comparing residuals for each micro-window, we can evaluate the major contributions brought by the C_2H_6 PLL and O_3 updates (Figure 5.2.b) compared to

the original HITRAN 2008 parameters (Figure 5.2.a). Finally, Figure 5.2.c shows a refinement of residuals on the edges of MW1 and MW3 due to the use of the CH_3Cl update. From Table 5.2 it appears that HITRAN 2008 along with the three updates minimizes the residuals in all micro-windows and hence is currently the best spectroscopic database to employ for ISSJ solar spectra. It is worth noting that the increased residuals observed with the HITRAN 2012 compilation compared to the set up using HITRAN 2008, especially in MW2 (see Table 5.2), are due to changes in H_2O parameters, more particularly in temperature and pressure-dependency parameters of the H_2O feature at 2983.316 cm^{-1}.

5.2.3. Data characterization and error budget

5.2.3.1. Characterization of the FTIR retrievals

The averaging kernel matrix (**A**) is resulted by the inversion process of FTIR solar spectra and characterizes the information content of the retrievals. It describes how the retrieved concentration and vertical distribution of an absorber in the atmosphere are related to the true profile (x_t) and also provides the contribution of the a priori (x_a) to the retrieved profile (x_r) according to Equation 5.1.

$$x_r = x_a + \boldsymbol{A}(x_t - x_a) \tag{5.1}$$

Figure 5.3 displays the mean averaging kernels for each vertical layer (Figure 5.3.b; expressed in molec.cm^{-2}/molec.cm^{-2}) and calculated on the basis of the 2008−2010 individual retrieved profiles, as well as the leading eigenvalues and eigenvectors (Figure 5.3.a). The vertical sensitivity of our retrieval strategy is illustrated by the total column averaging kernel drawn in black dashed line in Figure 5.3.b (here with values divided by 10 for visibility purpose). It indicates very good sensitivity to the true state of the atmosphere below ~13 km altitude, with 99 % of the information content independent from the a priori profile (x_a) and mainly provided by the first eigenvector. The second and third eigenvectors and their associated eigenvalues indicate that the sensitivity of the retrievals extends in the lower stratosphere up to ~20 km, with some additional vertical resolution.

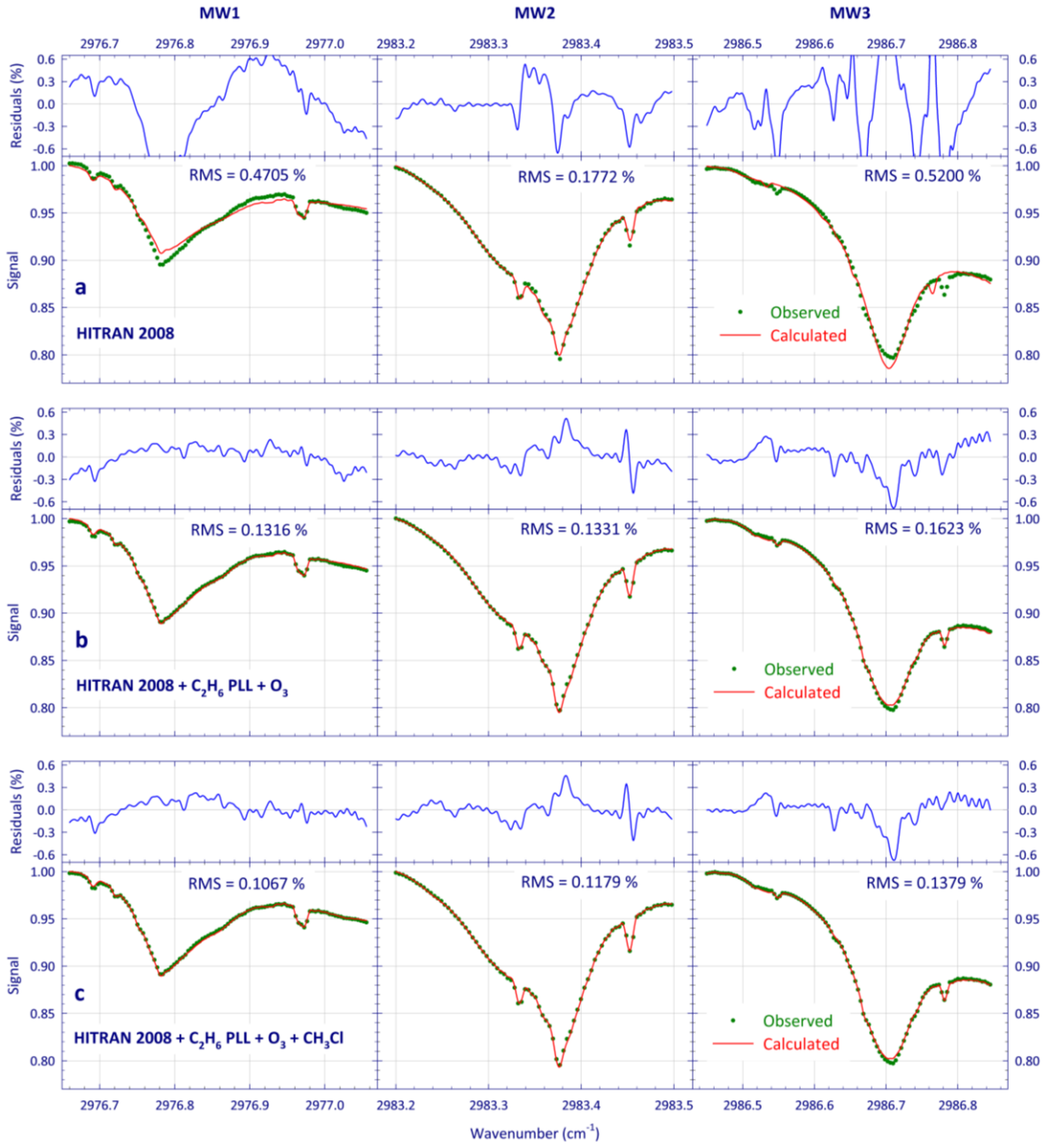

Figure 5.2 Mean observed (green dots) and calculated (red lines) spectra and associated residuals (obs. – calc.; blue lines) for a representative subset of 229 spectral fits with in the three micro-windows used for the C_2H_6 retrieval at ISSJ. Spectroscopic compilations used here are (a) the original HITRAN 2008 database, (b) HITRAN 2008 combined with the C_2H_6 PLL as well as O_3 update and (c) HITRAN 2008 combined with C_2H_6, O_3 and updated CH_3Cl lines. Note the improvements brought by the different updates on the residuals, whose mean values are provided in Table 5.2.

With a mean degree of freedom for signal (DOFS) of 2.11 ± 0.27 (1-σ confidence interval calculated over all 2008–2010 fitted spectra) and the two leading eigenvalues equal to 0.99 and 0.86, two independent pieces of information may be deduced from the averaging kernels. A first partial column is derived in the lower troposphere (from the ISSJ elevation up to ~8.5 km altitude) and a second one spanning the 8.5–22 km altitude range is identified in the upper troposphere lower stratosphere. The sensitivity of our

retrieval strategy is slightly diminishing for altitudes above ~13 km, but a large part of the information content (at least 60 %) is still provided by the measurements at the 22 km level. Although independent partial columns are available from the retrieval process at ISSJ, we will only consider total columns of C_2H_6 in this study.

When compared with other recent works using pseudo-lines to retrieve C_2H_6 amounts, the content of information obtained from our retrievals is consistent with results from e.g., [*Viatte et al.*, 2014] at Eureka, Canada (80.0°N, 86.4°W, 610 m a.s.l.; DOFS = 2.00 ± 0.20) who also employed the three micro-windows, and represents a significant improvement compared to previous works carried out at ISSJ, with typical DOFS of about 1.5 when using the $^PQ_3$ feature alone. The simultaneous use of the three non-contiguous micro-windows allows for a significant gain in retrieved information content compared to three non-simultaneous retrievals which would be subsequently averaged. The DOFS obtained from the individual use of each micro-window are 1.51 ± 0.24, 1.86 ± 0.25 and 1.70 ± 0.23 for MW1, MW2 and MW3, respectively.

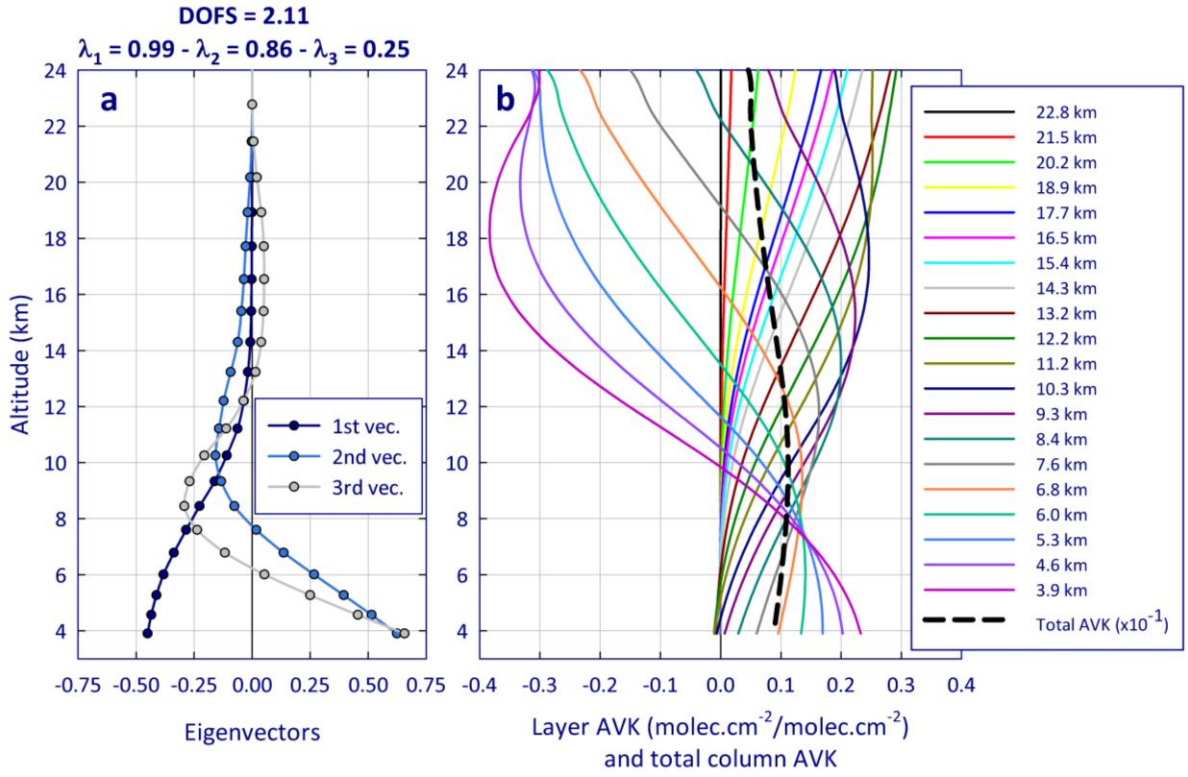

Figure 5.3. (a) First eigenvectors and associated eigenvalues, and (b) individual averaging kernels for each layer between the 3.6 and 24.0 km altitude range and total column averaging kernel (thick dashed line; divided here by 10 for visibility purpose) characterizing the FTIR retrievals of C_2H_6 at ISSJ. The information content has been established on the basis of all the individual retrieved profiles throughout the 2008–2010 timespan. The averaging kernels from 2008–2010 are used in Section 5.2.5.1 to smooth GEOS-Chem profiles in comparison with the FTIR products. Moreover, tests have shown that the DOFS, eigenvectors and averaging kernels calculated on the basis of other years provide consistent results in terms of information content.

5.2.3.2. Error budget

Table 5.3 summarizes the major sources of uncertainty that may affect the C_2H_6 columns retrieved from the ISSJ solar spectra, as well as estimates of their respective contribution to either systematic or random component of the error budget. The total errors are the square root of the sum of the squares of each of the contributing uncertainty sources. Most of the error contributions (excepting when specified below) have been calculated on the basis of all solar spectra from year 2003 according to the sensitivity tests listed in the last column of Table 5.3. The C_2H_6 retrieval is also characterized at ISSJ by an assumed variability of 29.2 % and a daily relative standard deviation (calculated here for the days with at least three observations) equal to 4.0 %.

The major contribution to the systematic component of the error budget comes from uncertainties on the C_2H_6 spectroscopy. An error of 4 % on the line intensity from the original spectra measurements has been reported in *Harrison et al.*, [2010]. In addition, the uncertainty induced by the conversion of C_2H_6 cross-sections into pseudo-lines is estimated at 4 % [*Rinsland et al.*, 2012], including the random error in the pseudo-line spectroscopic parameters and the systematic error due to an imperfect representation of the physics by the pseudo-lines. We have combined the 4 % from *Harrison et al.*, [2010] in quadrature with the 4 % from the conversion into pseudo-lines, giving a conservative 246 uncertainty of 5.6 % on the C_2H_6 absorption. When assuming this uncertainty during the inversion process, the retrieved C_2H_6 columns are affected by systematic anomalies of 5.6 %.

Retrieved column biases due to line intensity uncertainties related to the interfering species have been gauged independently by assuming the maximum errors quoted in the HITRAN 2008 (for H_2O, CH_4 and O3) and HITRAN 2012 (for the CH_3Cl updated line parameters, included in this official release) databases during the fitting process. The column anomalies corresponding to each interfering gases have been combined in quadrature and contribute for 0.9 % to the systematic component of the error budget.

Other contributions to the total systematic error are minor. The total columns are retrieved from high quality solar spectra using the SFIT algorithm within uncertainties estimated at ±1 % [*Hase et al.*, 2004]. The impact of an assumed instrumental misalignment of ±10 % at the maximum path difference on the retrieved columns is almost negligible (0.1 %). Finally, the impact of the selection of the a priori C_2H_6 state on the retrieved columns is estimated by adopting other realistic C_2H_6 mixing ratio profiles simulated by the GEOS-Chem and WACCM models as a priori, which leads to small divergences by up to 1.2 %.

As random errors, we have assumed a 0.2°error in the solar pointing and have adopted the temperature-profile uncertainties quoted by NCEP (±1.5 °C between the ground and 20 km altitude, ±2.0 °C for the 20-30 km altitude range, and from ±5 °C at 35 km up to ±9 °C at the stratopause). The corresponding biases on the retrieved C_2H_6 columns amount to 0.8 and 1.3 %, respectively. As in *Franco et al.*, [2015], we have also made the tropospheric slope of the H2O a priori profile vary by a factor 2; such perturbations only induce 0.1 % bias in the C_2H_6 columns, highlighting the independence of the C_2H_6 retrieval to the tropospheric water vapor content for a dry high-altitude site.

Error source	Error (%)	Comments
Assumed variability	29.2	
Relative standard deviation	4.0	For the days with at least 3 observations
Systematic errors		
C_2H_6 spectroscopy and conversion into pseudo-lines	5.6	± 5.6% uncertainty on line intensity
Line intensity of interfering gases	0.9	HITRAN 2008 uncertainties (up to 10% for H_2O, 20 % for O_3, 30 % for CH_4 and 20 % for CH_3Cl)
ILS	0.1	± 10% misalignment and instrument bias
Forward model	1.0	Retrieval algorithm-related
C_2H_6 a priori profile	1.2	C_2H_6 a priori profiles derived from GEOS-Chem and WACCM
Total Systematic Error	5.9	
Random errors		
Temperature profiles	1.3	NCEP profile uncertainty (see text)
H2O a priori profile	0.1	Changes by a factor of 2 in H2O a priori slope
Solar Zenith Angle(SZA)	0.8	± 0.2° bias
Measurement noise	1.6	
Smoothing	1.1	
Model parameters	0.2	
Total Random Error	2.4	

Table 5.3. Error budget of the C_2H_6 retrievals at ISSJ, including the impact of systematic and random uncertainties on total columns retrieved from all individual solar spectra recorded during the year 2003, according to specifics given in the last column. The contributions of measurement noise, smoothing and model parameters have been estimated on the basis of a representative subset of solar spectra following the formalism of Rodgers, [2000].

According to the formalism of *Rodgers* [2000] and such as detailed in Section 2.2.2 in *Vigouroux et al.*, [2009], we have computed the gain and sensitivity matrices of a subset of solar spectra representative of the ISSJ dataset in terms of S/N ratio, DOFS, solar zenith angle, residuals, etc., eventually providing the respective contributions of measurement noise (1.6 %), smoothing (1.1 %) and forward model parameters (0.2 %) to the total random error.

The estimated total systematic and random errors affecting our retrieved C_2H_6 columns amount to 5.9 and 2.4 %, respectively. The latter represents a significant improvement compared to *Rinsland et al.*, [2000], where only the 2976–2977 cm^{-1} micro-window with the $^PQ_3$ branch for inversion of the ISSJ solar spectra is used and where the random component of the error budget is estimated in a similar way at 6.6 % (and also found 5.9 % of total bias for the systematic component).

5.2.4. Supporting model simulations

5.2.4.1. CHASER

The CHASER model [*Sudo*, 2002; *Sudo and Akimoto*, 2007], developed mainly in the Nagoya University and the Japan Agency for Marine-Earth Science and Technology (JAMSTEC), is a chemistry coupled climate model, simulating atmospheric chemistry and aerosols in cooperation with the aerosol component model SPRINTARS [Spectral Radiation-Transport Model for Aerosol Species; *Takemura*, 2005]. It has also been developed in the framework of the Model for Interdisciplinary Research on Climate-Earth System Model, MIROC-ESM-CHEM [*Watanabe et al.*, 2011]. CHASER simulates detailed chemistry in the troposphere and stratosphere with an on-line aerosol simulation including production of particulate nitrate and secondary organic aerosols.

For this study, the model's horizontal resolution is selected to be 2.8°x 2.8°with 36 vertical layers extending from the surface up to about 50 km altitude. As the overall model structure, CHASER is fully coupled with the climate model core MIROC, permitting atmospheric constituents (both gases and aerosols) to interact radioactively and hydrologically with meteorological fields in the model. For replicating the past meteorological conditions in the model, this study employs a nudged chemical transport model version of CHASER in which wind fields and temperatures calculated by the MIROC's AGCM are relaxed to meteorological reanalysis data. In this study, the NCEP final reanalysis data set is used as a nudging constraint with the HadISST data set (Hadley Centre Sea Ice and Sea Surface Temperature) for distributions of sea surface temperatures and sea ice. Chemistry component of CHASER considers the chemical cycle of O_x-NO_x-HO_x-CH_4-CO with oxidation of Non-Methane Volatile Organic Compounds (NMVOCs), halogen chemistry and NH_x-SO_x-NO_3 system simulating 96 chemical species with 287 chemical reactions. In the model, NMVOCs include C_2H_6, C_2H_4, propane (C_3H_8), C_3H_6, C_4H_{10}, acetone, methanol and biogenic NMVOCs (isoprene, terpenes).

Anthropogenic emissions (for NO_x, CO, CH_4, NMVOCs, NH_3, SO_2, black carbon and organic carbon) are specified using the EDGAR-HTAP2 (Emission Database for Global Atmospheric Research, targeted for 2008: http://edgar.jrc.ec.europa.eu/) and fire emissions are based on the MACC's reanalysis data (Monitoring Atmospheric Composition & Change; https://gmes-atmosphere.eu/about/project structure/input_data/d_re/) for individual years/months. For biogenic NMVOC emissions, we employ calculation by the land ecosystem/trace gas emission model VISIT [Vegetation Integrative SImulator for Trace gases; *Ito*, 2010].

5.2.4.2. GEOS-Chem

GEOS-Chem (version 9-01-03: http://acmg.seas.harvard.edu/geos/doc/archive/man.v9-01-03/index.html) is a global 3-D CTM capable of simulating global trace gas and aerosol distributions. GEOS-Chem is driven by assimilated meteorological fields from the Goddard Earth Observing System version (GEOS-5) of the NASA Global Modeling Assimilation Office (GMAO). The GEOS-5 meteorology data have a temporal frequency of 6 h (3 h for mixing depths and surface properties) and are at a native horizontal resolution of 0.5°x 0.667°with 72 hybrid pressure-σ levels describing the atmosphere from the surface up to 0.01 hPa. In the framework of this study, the GEOS-5 fields are degraded for model input to

a 2°x 2.5°horizontal resolution and 47 vertical levels by collapsing levels above ~80 hPa. The chemical mechanism applied here is the standard full chemistry GEOS-Chem simulation, including detailed O_3-NO_x-Volatile Organic Compound (VOC)-aerosol coupled chemistry [see *Bey et al.*, 2001 and *Park et al.*, 2004 for full description] with updates by *Mao et al.*, [2010].

Ethane is emitted from anthropogenic and pyrogenic sources in GEOS-Chem. The RETRO (REanalysis of the TROpospheric chemical composition) emission inventory [*van het Bolscher et al.*, 2008] is the global default for anthropogenic NMVOC emissions aside from C_2H_6 and C_3H_8. Ethane and C_3H_8 emissions in RETRO are low compared to the GEOS-Chem inventories from *Xiao et al.*, [2008], which are unbiased relative to the pre-2004 observations presented as in *Xiao et al.*, [2008]. Thus we used the C_2H_6 and C_3H_8 emission inventories from *Xiao et al.*, [2008]. Ethane emissions from biomass burning are from the Global Fire Emissions Database (GFED3) monthly biomass burning emissions [*van der Werf et al.*, 2010].

The GEOS-Chem model output presented here covers the period July 2005 May 2013, for which the GEOS-5 meteorological fields are available. We have used a one-year run for spin-up from July 2004 to June 2005, restarted several times for chemical initialization. The model outputs consist of C_2H_6 mixing ratio profiles at a three-hour time frequency, saved at the closest 2°± 2.5°pixel of the ISSJ station. To account for the vertical resolution and sensitivity of the FTIR retrievals, the individual concentration profiles simulated by GEOS-Chem are interpolated onto the vertical grid of FTIR. They are then averaged into daily profiles and eventually smoothed by applying the FTIR averaging kernels A (see Equation 5.1) according to the formalism of *Rodgers*, [2003]. The averaging kernels used to convolve the model outputs are seasonal averages over March-May, June-August, September-November and December-February obtained from the 2008−2010 individual FTIR retrievals. The following comparison between FTIR and smoothed GEOS-Chem data involves the days with observations available within the July 2005−May 2013 time period only (i.e. 915 days of observations).

5.2.5. Ethane time series

In this section, we first present a preliminary comparison between C_2H_6 FTIR total columns and simulations by the GEOS-Chem model by illustrating the seasonal cycle of C_2H_6 at ISSJ. We have taken into account the vertical resolution and specific sensitivity of the FTIR retrievals before comparison with the model data. We then report the entire 1994−2014 time series of daily-mean total columns and corresponding trends.

5.2.5.1. Seasonal cycle

The seasonal cycle of C_2H_6 abundances above ISSJ is illustrated in Figure 5.4, which displays on a one-year time base the monthly means of FTIR total columns and associated 1-σ standard deviation as error bars. The running mean of the FTIR daily average data (not shown here), computed using a two-month integration length and a 15-day time step, is drawn in solid blue line. The shaded area corresponds to the 1-σ standard deviation around the running mean. The FTIR data subset used in Figure 5.4 spans the July 2005−May 2013 time period in order to coincide with the GEOS-Chem simulation. A similar running mean and standard deviation have also been calculated on the basis of the daily-averaged total columns

simulated by GEOS-Chem (after smoothing by the FTIR averaging kernels). These are represented by the red curve and by the shaded area in Figure 5.4, respectively.

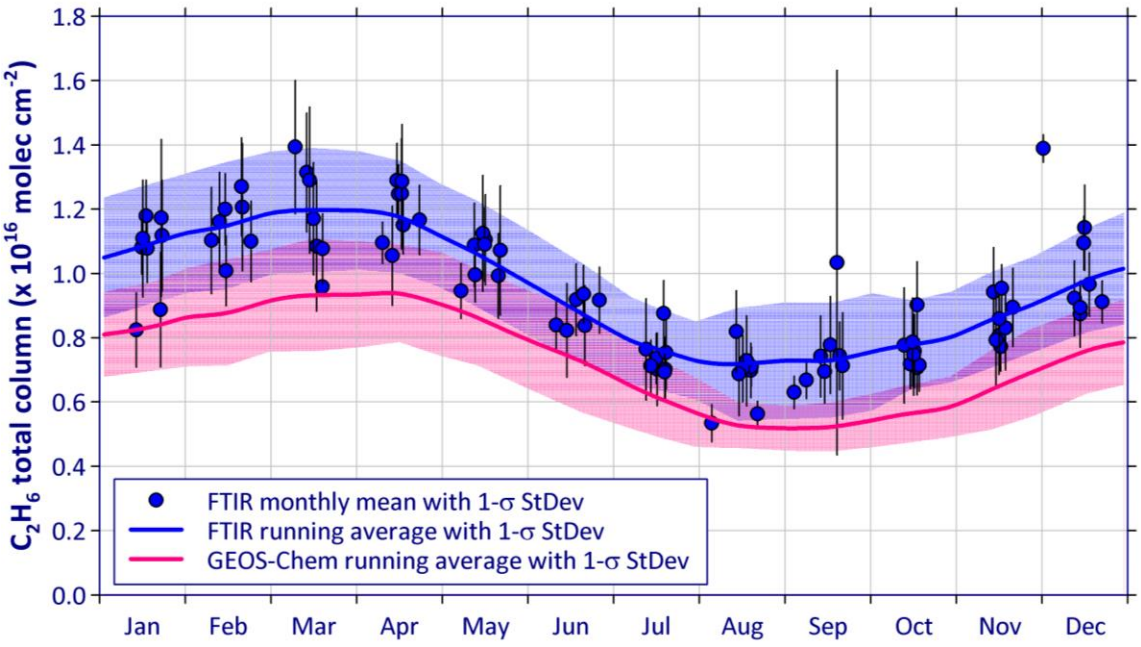

Figure 5.4. Monthly-averaged total columns of C_2H_6 and associated 1-σ standard deviation bars displayed on a 1-year time base, from the FTIR retrievals performed above ISSJ between July 2005 and May 2013. The blue curve and shaded area show on a 1-year time base the running mean fit to the daily-averaged columns (with a 2-month wide integration time and a 15-day time step) and the associated 1-σ standard deviation, respectively. The red line and shaded area represent corresponding information, but deduced from the smoothed GEOS-Chem output. Note that the 1-σ standard deviations around the running mean are calculated on the basis of the daily-averaged columns and hence include interannual fluctuations as well as variability of the monthly mean.

The seasonal cycle of C_2H_6 apparent in the FTIR total column data and model output are in good agreement, characterized by a maximum in March−April and a minimum in August−September. Since fossil fuel production is the main source of C_2H_6 emissions [*Xiao et al.*, 2008] and does not present a particular seasonal cycle during the year [*Pozzer et al.*, 2010], the strong seasonal cycle of C_2H_6 burden is primarily driven by the photochemical oxidation rate by OH radicals, which is enhanced during summer [*Schmidt et al.*, 1991; *Simpson et al.*, 2012]. At mid and high latitudes, C_2H_6 accumulates during wintertime and peaks in late winter due to its relatively long lifetime and slow exchange with lower latitudes [*Rinsland et al.*, 2000]. Consistent values of seasonal amplitude, i.e. the difference between the maximum and minimum running means divided by the annual average over the whole time period, are associated with these seasonal modulations: 50.4 % and 57.3 % for FTIR and GEOS-Chem, respectively. A direct comparison between the daily-mean C_2H_6 total columns derived from the CTM and ground-based observations is presented in Figure 5.5 and shows a correlation R of 0.77.

However, it appears clearly on Figures 5.4 and 5.5 that the C_2H_6 burden simulated by GEOS-Chem is systematically lower than the FTIR measurements. Over the mid-2005–mid-2013 time period, the daily-averaged modeled C_2H_6 columns present a systematic bias of -26.7 ± 16.5 % relative to the FTIR daily means, and the two data sets cannot be reconciled by accounting for the systematic errors affecting the observations (see Table 5.3). The systematic bias is hypothesized to be driven by an underestimation of the C_2H_6 emissions used by the model that were developed only considering data collected prior to 2004. Incorporating updated and more accurate emission inventories into GEOS-Chem is the focus of ongoing work and is beyond the scope of this paper.

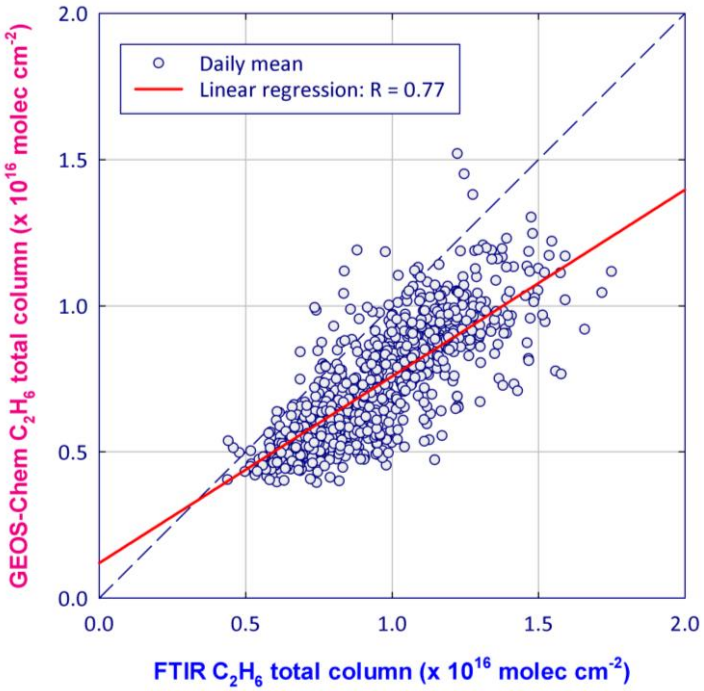

Figure 5.5. FTIR daily-averaged total columns of C_2H_6 versus daily-averaged C_2H_6 abundances derived from smoothed GEOS-Chem profiles over the July 2005–May 2013 time span. The straight red line corresponds to the linear regression (with R as the correlation coefficient) between both data sets.

The retrieved columns of C_2H_6 at ISSJ are consistent with ground-based FTIR measurements from other stations in terms of amounts and seasonal cycle, taking into account the latitude and elevation of the ISSJ station [*Rinsland et al.*, 2001, 2002; *Zhao*, 2002; *Gardiner et al.*, 2008; *Angelbratt et al.*, 2011; *Vigouroux et al.*, 2012; *Zeng et al.*, 2012; *Viatte et al.*, 2014]. At high altitude stations such as ISSJ, lower burden and seasonal amplitude are generally observed due to high concentrations of C_2H_6 in the lowest tropospheric layers [*Angelbratt et al.*, 2011]. For instance, monthly-mean columns ranging between 1.76 ± 0.40 and 3.36 ± 0.30 x 10^{16} molec.cm^{-2} and a corresponding seasonal amplitude of 63 % were obtained from ground-based FTIR solar spectra recorded over 1995-2000 at two Northern Hemisphere mid-latitude (44°N) stations located almost at sea level in Japan [*Zhao*, 2002]. The amplitude of the seasonal cycle is generally larger at high-latitude sites because of the enhanced fossil fuel emissions [*Zeng et al.*, 2012] and very weak oxidation rate by OH radicals in winter, allowing C_2H_6 to accumulate substantially during this season. At

Eureka, *Viatte et al.*, [2014] retrieved monthly-mean C_2H_6 columns between 1.2 and 2.85 x 10^{16} molec.cm^{-2} from FTIR observations for 2007−2011, and the amplitude of the seasonal cycle was 93 %.

5.2.5.2. Long-term trend

Figure 5.6 presents the long-term time series of daily-averaged C_2H_6 total columns (in molec.cm^{-2}) retrieved from the ISSJ solar spectra for the September 1994−August 2014 time period, which consists of 11 859 measurements spread over 2 224 days of observation. The error bars associated with these daily means correspond to the 1-σ standard deviation of the measurements within each day. This FTIR database homogeneously covers the investigated time span. We have used the statistical bootstrap resampling tool developed as in *Gardiner et al.*, [2008] to fit the whole daily time series in order to determine the C_2H_6 long-term linear trend (as well as the associated uncertainty) and the seasonal modulation. This bootstrap method combines a linear function and a 3rd order Fourier series taking into account the intra-annual variability of the data set.

Moreover, a running mean of the daily average data with a three-year wide integration time and a six-month step has revealed a minimum in the time series between the end of 2008 and the beginning of 2009. Therefore we have fitted both 1994−2008 and 2009−2014 time periods separately with the bootstrap tool that has returned two statistically-significant trends of C_2H_6 total columns at the 2-σ confidence level: - 9.56 ± 1.91 x 10^{13} molec.cm^{-2}.yr^{-1} and 4.35 ± 0.81 x 10^{14} molec.cm^{-2}.yr^{-1}, respectively. Then we have used both 1995.0 and 2009.0 columns modeled by the bootstrap tool as references in order to calculate the relative annual trends.

Analysis of the 1994−2008 time span reveals a regular decrease of the C_2H_6 amounts above ISSJ by -0.92 ± 0.18 %.yr^{-1} relative to 1995.0. This negative trend is consistent with measurements and corresponding trends of atmospheric C_2H_6 burden presented in *Simpson et al.*, [2012] and *Aydin et al.*, [2011], both studies attributed the decline of global C_2H_6 emissions from the mid-1980s to reduced fugitive emissions from fossil fuel sources in Northern Hemisphere rather than a decrease in biomass burning and biofuel use (the other major sources of C_2H_6). These fugitive emissions mainly include natural gas loss due to evaporation, venting and flaring as well as equipment leaks during the production and processing of natural gas and oil. Consistent trends derived from FTIR solar spectra have already been reported at ISSJ by previous studies, but over shorter time periods: - 2.70 ± 0.30 %.yr^{-1} over 1985−1995 [*Mahieu et al.*, 1997], - 1.20 ± 0.65 %.yr^{-1} over 1995−1999 [*Rinsland et al.*, 2000], -1.05 ± 0.35 %.yr^{-1} over 1995−2004 [*Gardiner et al.*, 2008] and - 1.51 ± 0.23 %.yr^{-1} over 1996−2006 [*Angelbratt et al.*, 2011]. Global C_2H_6 emissions did not decline as rapidly between 2000 and 2010 period compared to the 1980s and 1990s [*Aydin et al.*, 2011; *Simpson et al.*, 2012], and this is consistent with our reported negative trend, which is smaller than reported in previous ISSJ studies.

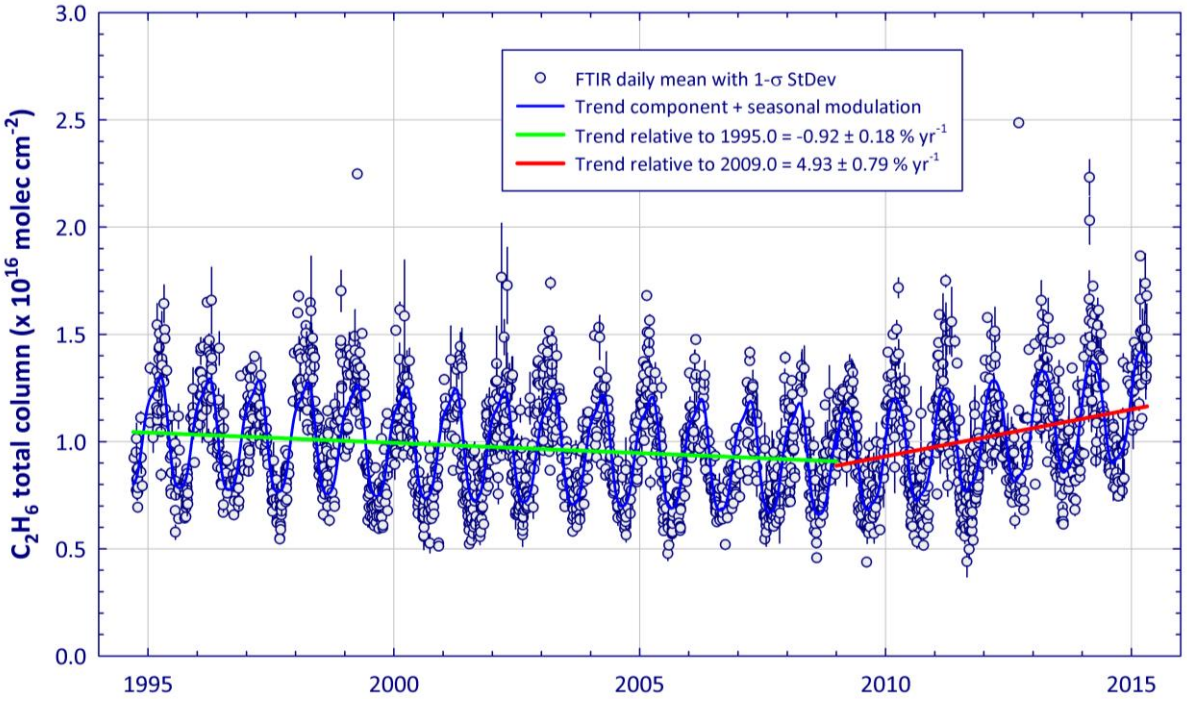

Figure 5.6. FTIR time series of daily-averaged C_2H_6 total columns and associated 1-σ standard deviation bars above ISSJ from September 1994 to August 2014. The functions fitted to all available daily means (including seasonal modulation and trend component) and calculated by the bootstrap resampling tool of [Gardiner et al., [2008] over the 1994–2008 and 2009–2014 time periods are drawn in blue curve. The green and red solid lines correspond to the trend components of these fitting functions.

Conversely, for the 2009−2014 time period, the bootstrap tool reveals a strong positive trend of C_2H_6 total columns of 4.90 ± 0.91 %.yr^{-1} relative to 2009.0 above ISSJ. We have also applied the bootstrap tool to the 3.58−8.88 and 8.88−22.10 km partial columns of C_2H_6 above ISSJ (see Section 5.2.3.1) and have found very similar positive trends relative to 2009.0, suggesting a vertically-homogeneous increase of C_2H_6 throughout the troposphere (and lower stratosphere). To our knowledge, this recent increase of the C_2H_6 burden in the background atmosphere has not been reported and its origin is still unidentified.

A hypothetical source may be enhanced fugitive emissions of C_2H_6 linked to the recent growth in the exploitation of shale gas and tight oil reservoirs. The growth has been especially massive in North America. Indeed, positive anomalies of CH_4 related to the oil and gas industries have been recently detected from space over regions of North America where the drilling productivity began to grow rapidly after 2009 (see [69]). This hypothesis is supported by measurements derived from 1 986 solar occultation observations performed over North America (16°−88°N and 173°−50°W) between 2004 and the middle of 2013 by the ACE-FTS instrument [*Bernath et al.*, 2005]. We employed the version 3.5 ACE-FTS data [*Boone et al.*, 2013], which includes an improved retrieval strategy for C_2H_6, within the 8−16 km altitude range. Applying the bootstrap tool to the ACE-FTS partial columns over the 2004-2008 and 2009-2013 time periods, we have calculated statistically-significant trends (at the 2-σ level) of - 1.75 ± 1.30 and 9.4 ± 3.2 %.yr^{-1} relative to 2005.0 and 2009.0, respectively, which are consistent with the FTIR trends when accounting for the associated uncertainty ranges. Trends derived from 906 ACE-FTS measurements between 10°−40°S do not

reveal any recent increase of the C_2H_6 burden. Instead these data show a statistically significant decrease (- 1.62 ± 1.08 %.yr^{-1}) over the 2004 to mid-2013 time period. This suggests that the observed increase of C_2H_6 is limited to the Northern Hemisphere.

It is worth noting that the GEOS-Chem CTM does not reproduce this recent increase in the abundance of C_2H_6 above ISSJ, suggesting emission inventories for C_2H_6 and other light alkanes may not be properly accounting for the enhanced fugitive emissions from recent natural gas and oil production.

5.2.6. Discussions and conclusions

In this study, we have developed and optimized a new strategy based on an improved spectroscopy to retrieve C_2H_6 total and partial columns from ground-based FTIR solar spectra recorded at the dry and high-altitude ISSJ. The selected spectroscopic parameters accounted for in the three micro-windows include C_2H_6 pseudo-lines based on cross-section laboratory spectra as well as updated line features for O_3 and CH_3Cl. Such an improved spectroscopy has yielded substantially reduced fitting residuals, enhanced information content (with a mean DOFS of 2.11 ± 0.27 for the whole data set) and less solar spectra discarded because of ungeophysical mixing ratio profiles.

We have applied this strategy to the long-term FTIR time series available at ISSJ (spanning 1994−2014) and compared the retrieved total columns to C_2H_6 columns simulated by the GEOS-Chem CTM, taking into account the vertical sensitivity of the retrievals by convolving the modeled profiles with the FTIR averaging kernels. The observations and the model present consistent seasonal cycles, but GEOS-Chem under-predicts the observed C_2H_6 burden throughout the seasonal cycle. This suggests an underestimation of C_2H_6 emissions in the model and points to the need for improved inventories for further GEOS-Chem simulations and sensitivity tests.

Finally, we have presented the 20-year ISSJ time series of C_2H_6 column abundance. Using a bootstrap resampling tool, we have calculated a statistically-significant negative trend in C_2H_6 total columns until 2009, consistent with prior studies and with our understanding of global C_2H_6 emissions. However, the ISSJ time series has also revealed a strong positive trend in C_2H_6 over the last years of the record, from 2009 onwards. Such a recent increase in the remote atmosphere is still unreported and, because of the involvement of C_2H_6 in the global VOC-HOx-NOx chemistry responsible for generating or destroying tropospheric O_3, investigating both its cause and its impact on air quality should be a high priority for the atmospheric chemistry community.

This C_2H_6 increase extends beyond previous positive short-term anomalies already observed in the Northern Hemisphere, which occur every 3−5 years and are generally associated with variability in biomass burning emissions [*Simpson et al.*, 2006, 2012]. The seasonal cycle of C_2H_6 above ISSJ is primarily driven by the photochemical cycle of its main sink (OH radicals). We argue that it is unlikely that the recent increase can be attributed to sharp fluctuations of OH concentration in the atmosphere because the global OH levels have not exhibited large interannual variability since the end of the 20th century [*Montzka et al.*, 2011]. Indeed, neither CO nor other species that have oxidation by OH as their major removal pathway

such as hydrogen cyanide (HCN) and acetylene (C_2H_2), do not present an upturn in their retrieved columns above ISSJ over the last years. However, CH_4, which is closely linked to C_2H_6 [*Simpson et al.*, 2006, 2012], has also presented globally a renewed rise after 2006 [*Kirschke et al.*, 2013]. We hypothesize that the observed recent increase in C_2H_6 above ISSJ could represent a change in C_2H_6 throughout the Northern Hemisphere and may be the product of a large increase in fugitive emissions related to the recent upturn in the development of North American shale gas and tight oil reservoirs.

The lifetime of C_2H_6 is approximately months, and this makes C_2H_6 influenced by vertical mixing and long-range transport. Ethane is therefore a convenient tracer of anthropogenic activity for remote sensing [*Schmidt et al.*, 1991]. Measurements of C_2H_6 in the remote troposphere can also be used to identify air masses that have originated in regions with significant oil and gas production [*Simpson et al.*, 2012]. Air masses impacted by intense episodes of biomass burning have already been detected in the retrieved C_2H_6 columns at ISSJ, associated with severe tropical emissions from Asia during the strong El Niño event of 1997−1998 [*Rinsland et al.*, 2000]. Our future work will focus on combining an analysis of C_2H_6 measurements from ground-based FTIR solar spectra and observations from ACE-FTS with dedicated GEOS-Chem simulations with updated inventories. The goal will be to identify the cause of the recent increase in C_2H_6 and evaluate the magnitude of emissions required to produce the observed changes.

5.3. Follow-up and ongoing work

Ongoing work carried out at GIRPAS is planned in two steps, first focused on North America and then on the global scale. The recent increase of C_2H_6 will be confirmed and quantified through the analysis of time series derived from FTIR observations at Northern American sites (e.g. Toronto, Boulder,…). This will allow verifying the hypothesis that massive shale gas exploitation in the US is responsible for the observed re-increase. Since best emission inventories currently available significantly underestimate the observed C_2H_6 burden, we need to investigate on better C_2H_6 emissions. The bottom-up approach will consist in evaluating the amount of C_2H_6 emitted to match the C_2H_6 upturn as observed by FTIR measurements while the top-down approach will assess a new emission inventory of C_2H_6 in North America, based on observations of methane from the Greenhouse Gases Observing Satellite [GOSAT, developed by the Japan Aerospace Exploration Agency, JAXA, *Kuze et al.*, 2009] and inferred using C_2H_6/CH_4 emission ratios.

The C_2H_6 re-increase will be characterized at a global level by achieving a multi-site study regrouping most ground-based FTIR observation sites (NDACC or non-affiliated that perform measurements since at least 2009). In an effort of producing harmonized C_2H_6 time series, the C_2H_6 retrieval strategy as developed and described in [*Franco et al.*, 2015a] with comments provided above will be applied to all participating stations. This global FTIR study will provide additional information for us to infer adjusted C_2H_6 emission inventories and therefore enabling us to assess the impact of the C_2H_6 re-increase on the "air quality". Indeed, thanks to the improved information content associated to this newly optimized retrieval strategy we are able to derive tropospheric C_2H_6 partial columns from FTIR observations. From tropospheric C_2H_6 partial columns, the impact on levels of tropospheric O_3 will be quantified thanks to dedicated simulations.

Chapter 6 – Methane

Chapter 6 – Methane

6.1. Introduction

The harmonization of a retrieval strategy for methane for the whole infrared working group of NDACC to which I contributed is still ongoing. The major remaining issues are the availability of highly accurate and consistent spectroscopic parameters for CH_4 and the inversion of water vapor alongside. Indeed, as mentioned by *Sussmann et al.* [2011] and *Frankenberg et al.* [2008], erroneous spectroscopic parameters can lead to airmass-dependent artifacts impacting methane seasonality. Regarding water vapor, it presents strong absorption lines close to CH_4 lines and therefore heavily impacts the interference errors associated to the retrieval of CH_4 even leading to the determination of wrong CH_4 seasonality for low altitude humid sites. Most retrieval strategies applied at ground-based FTIR stations are either based on the work of *Sepúlveda et al.*, [2012] or *Sussmann et al.*, [2011].

The manuscript presented in the following sections is in preparation for submission in Atmospheric Chemistry and Physics in the framework of the special issue "Twenty-five years of operations of the Network for the Detection of Atmospheric Composition Change (NDACC) (AMT/ACP/ESSD Inter-Journal SI)". My contributions to this multi-site study include (in chronological order):

- optimization of the retrieval strategy of CH_4 for Jungfraujoch,
- retrieval of the whole FTIR observations from the Bruker operated at the Jungfraujoch,
- analysis of total, tropospheric and stratospheric CH_4 time series as observed by the ten FTIR sites,
- determination of the trend affecting those time series over the 2005-2012 time period,
- regridding of the GEOS-Chem tagged simulations to the ten stations,
- smoothing of the GEOS-Chem simulations for each station by their respective averaging kernels,
- analysis of tropospheric, stratospheric and total columns of CH_4 since 2005 as simulated by GEOS-Chem,
- analysis of the 11 tracers and their changes since 2005 as simulated by GEOS-Chem for each FTIR stations.

The methods employed for the above mentioned tasks are fully detailed in the following sections.

6.2. Changes of atmospheric methane (CH_4) since 2005 from NDACC FTIR measurements and GEOS-Chem tagged simulation

Whitney Bader[1], B. Bovy[1], S. Conway[2], K. Strong[2], D. Smale[3], A. J. Turner[4], P. F. Bernath[5,6], T. Blumenstock[7], A. Coulon[8], B. Franco[1], O. Garcia[9], D. Griffith[10], F. Hase[7], P. Hausmann[11], N. Jones[10], B. Lejeune[1], I. Murata[12], I. Morino[13], H. Nakajima[13], C. Paton-Walsh[10], J. Robinson[3], M. Schneider[7], C. Servais[1], R. Sussmann[11] and E. Mahieu[1].

[1] Institute of Astrophysics and Geophysics, University of Liège, Liège, Belgium
[2] Department of Physics, University of Toronto, Toronto, ON, M5S 1A7, Canada
[3] National Institute of Water and Atmospheric Research, NIWA, Lauder, New Zealand
[4] School of Engineering and Applied Sciences, Harvard University, Cambridge, MA, USA.
[5] Department of Chemistry and Biochemistry, Old Dominion University, Norfolk, VA 23529, Canada
[6] Department of Chemistry, University of Waterloo, Waterloo, ON N2L 3G1, Canada
[7] Karlsruhe Institute of Technology (KIT), Institute of Meteorology and Climate Research (IMK-ASF), Karlsruhe, Germany
[8] Institute for Atmospheric and Climate Science, ETH Zurich, Zurich, Switzerland
[9] Izaña Atmospheric Research Centre (IARC), Agencia Estatal de Meteorologia (AEMET), Spain
[10] School of Chemistry, University of Wollongong, Australia
[11] Karlsruhe Institute of Technology, IMK-IFU, Garmisch-Partenkirchen, Germany
[12] Graduate School of Environment Studies, Tohoku University, Sendai 980-8578, Japan
[13] National Institute for Environment Studies (NIES), Tsukuba, Ibaraki 305-8506, Japan

Manuscript in preparation for submission in Atmospheric Chemistry and Physics.

Abstract

Changes of atmospheric methane (CH_4) since 2005 have been evaluated using Fourier Transform Infrared (FTIR) solar observations performed at 10 ground-based sites, all members of the Network for Detection of Atmospheric Composition Change (NDACC). From this, we find an increase of atmospheric methane total columns that amounts to 0.30 ± 0.04 %/year for the 2005−2012 period. We used the GEOS-Chem Chemical Transport Model tagged simulation that accounts for the contribution of each emission source and one sink in the total CH_4 simulated based on emissions inventories and transport. After regridding according to NDACC vertical layering using a conservative regridding scheme and smoothing by convolving with respective FTIR seasonal averaging kernels, GEOS-Chem simulation shows an increase of atmospheric methane of 0.35 ± 0.03 %/year which is in agreement with NDACC measurements. Analysis of the GEOS-Chem tagged simulation allows us to quantify the contribution of each tracer to the global methane change since 2005. We find that natural sources such as wetlands and biomass burning contribute to the inter-annual variability of methane. However, anthropogenic emissions such as coal mining, gas and oil transport and exploration which are mainly emitted in the Northern Hemisphere and act as secondary contributors to the global budget of methane, have played a major role in the increase of atmospheric methane observed since 2005.

Conclusions

This work has reported the study of atmospheric methane and two of its derivatives, i.e. ethane and methanol. Those three gases have an impact on air quality through their removal pathway. Indeed, in the troposphere their oxidation impacts the contents of ozone making them act as ozone precursors. In addition, in the stratosphere methane influences the content of ozone and the production of water vapor. Moreover, both methane and ethane contribute to the greenhouse radiative forcing. While the latter is an indirect greenhouse gas because of its sinks, the former is the second most important anthropogenic greenhouse gas after CO_2. Their concentrations have been primarily assessed from ground-based FTIR solar observations recorded at the high alpine International Scientific Station of the Jungfraujoch (3580 m a.s.l.), member of the Network for Detection of Atmospheric Composition Change, in the prospect of studying their long-term trend and recent changes as well as their seasonal and/or diurnal variations.

The primary challenge of this work was the development and optimization of retrieval strategies for the three studied gases from FTIR observations recorded at the Jungfraujoch. The development and optimization of a retrieval strategy is based on the selection of the best combination of parameters in order to limit interferences, minimize residuals, maximize the information content and thus maximize the altitude sensitivity range. To this end, we have performed systematic search for and evaluation of absorption lines of the target species and have determined the best combination of spectral windows. When required, several spectroscopic linelist for the target and interfering species have been tested as well as their impact on residuals and information content. We performed thorough comparisons of a priori mixing ratio profiles for target species produced from satellite observations or model simulations with support from in situ GC-MS surface measurements. Other parameters such as the signal-to-noise ratio for inversion, the solar zenith angle range, the slope and background curvature of the spectra and the effective apodisation parameter have been adjusted. Through this work a method for error analysis associated to the line parameter uncertainty has been developed and is currently of use in the GIRPAS group. It has been employed for each available combination of parameters and has served as an indicator for the selection of the best retrieval strategy to be employed.

A 17-year time series of methanol has been presented from the analysis of FTIR observations recorded at the Jungfraujoch [*Bader et al.*, 2014]. The optimized retrieval strategy consists in the combination, for the first time, of spectral windows that have been used in previous work [*Dufour et al.*, 2006; *Rinsland et al.*, 2009; *Vigouroux et al.*, 2009] resulting in the improvement of the information content. Indeed, with a typical DOFS of 1.82, a total, a lower tropospheric (3.58-7.18 km) and an upper tropospheric-lower stratospheric (UTLS, 7.18-14.84 km) columns are available. Both random and systematic error sources have been identified and characterized using the method developed through this work on spectra recorded in the year 2010, and are found to be respectively 5 and 7 % for the total column. Since the long-term trend analysis of methanol total columns shows no significant trend in the last 17 years, we analyzed the methanol seasonal cycle that exhibits a high peak-to-peak amplitude of 129.4 ± 5.5 % (1σ) for total columns. Methanol total and partial columns are characterized by a strong seasonal modulation with minimum values and variability in December to February and maximum columns in June–July. Regarding methanol diurnal variations, they are characterized by an increase of methanol in the morning and a decrease during the afternoon for all seasons but summer.

The lower tropospheric and upper tropospheric-lower stratospheric columns of methanol retrieved from Jungfraujoch FTIR spectra have been confronted with measurements respectively obtained with surface in situ GC-MS and ACE-FTS satellite measurements, giving satisfactory comparison results. The FTIR lower-tropospheric data shows good agreement with in situ measurements regarding the data dispersion while the retrieved UTLS columns have a close to statistical agreement with ACE-FTS occultations. Comparisons with simulations from the IMAGESv2 model have also been performed. They demonstrated an underestimation by IMAGES v2 of the peak-to-peak amplitude for total and lower-tropospheric columns therefore leading to seasonal differences with an overestimation of winter methanol and an underestimation in summertime by the model whereas we observed no systematic bias between FTIR results and the model IMAGESv2. Regarding UTLS columns, both IMAGESv2 and our FTIR methanol have seasonal cycles in phase and similar peak-to-peak amplitudes.

Even though the role of plant growth in methanol budget is confirmed by its seasonality, large uncertainties remain in the methanol budget. Thanks to the improvement of the information content of our retrieval and therefore our altitude sensitivity range, our total and partial columns time series provide a valuable tool for model and satellite validation and complement the NDACC measurements at northern mid-latitudes.

Regarding ethane, we have developed a new strategy that includes the use of improved spectroscopic parameters that include ethane pseudo-lines based on cross-section laboratory spectra as well as updated line features for ozone and methyl chloride. Such optimized retrieval strategy has substantially reduced fitting residuals and enhanced information content, with a mean DOFS of 2.11 (while previous work using only the branch near 2976 cm^{-1} showed a typical DOFS of 1.5). We have presented here a time series of ethane spanning 20 years of observations made at the Jungfraujoch [between 1994 and 2014; *Franco et al.*, 2015]. Total columns of ethane have been compared with columns simulated by the GEOS-Chem model. Comparisons show a good agreement regarding the seasonal cycle amplitude and phase of ethane but a systematic and significant underestimation of the ethane burden by GEOS-Chem, suggesting an underestimation of emissions of ethane by the emission inventories.

Analysis of long-term trend of ethane showed a negative trend from 1994 until 2009 and revealed a strong positive trend of ethane from 2009 onwards of 4.90 ± 0.91 $\%.year^{-1}$ (wrt 2009.0), reported for the first time [*Franco et al.*, 2015]. Since the main sink of ethane, i.e. the hydroxyl radical has not exhibited large interannual variability since the end of the 20th century [*Montzka et al.*, 2011], since no other species that are primarily removed from the atmosphere by oxidation by the hydroxyl radical present an upturn in their retrieved columns over the last years, and since methane, which shares emission sources with ethane, presents a global renewed rise after 2006 [*Kirschke et al.*, 2013]; we hypothesize that the observed recent increase in ethane above the Jungfraujoch could represent a change in ethane throughout the Northern Hemisphere and may be the product of a large increase in fugitive emissions related to the recent upturn in the development of North American shale gas and tight oil reservoirs.

This hypothesis will be further examined on the northern America continent and then on a global scale. The objective will be to confirm and quantify the recent increase over North America to reinforce the hypothesis that massive US shale gas exploitation US is responsible for the observed increase. To this end, our aim will be to evaluate more representative emission inventories, using top-down and bottom-up approaches in dedicated mode simulations. We will then characterize the ethane increase at a global level that will provide additional information to infer adjusted ethane emission inventories in order to assess the impact of the ethane increase on the air quality.

Finally, we quantified the changes of methane since 2005 from 10 ground-based NDACC sites, with a mean global increase of 0.30 ± 0.04 %.year^{-1} for the 2005-2012 period (wrt 2005.0). A GEOS-Chem tagged simulation that provides the contribution of each emission source and one sink to the total methane simulation, has been used in order to provide hypotheses for the source(s) responsible for the recent methane upturn. After regridding and smoothing of GEOS-Chem simulation results to match the spatial and vertical resolution of the ground-based observations as well as the vertical sensitivity range, comparisons between FTIR observations and a GEOS-Chem tagged simulation covering the 2005-2012 period have been presented. The global mean increase of methane as simulated by GEOS-Chem amounts to 0.35 ± 0.03 %.year^{-1} which is in good agreement with the observed mean annual changes as observed by the ground-based stations.

A detailed analysis of the GEOS-Chem tracer on both the local and global scales was performed in order to quantify the contribution of each tracer to the global methane change since 2005. From this, we determined that natural sources such as wetlands and biomass burning contribute to the inter-annual variability of methane, while the increasing anthropogenic emissions such as coal mining, gas and oil transport and exploration, mainly emitted in the Northern Hemisphere that are secondary contributors to the global budget of methane, have played a major role in the increase of atmospheric methane observed since 2005. Those conclusions are consistent with the hypothesis mentioned above of increasing exploitation of shale gas and oil leading to the increase of atmospheric ethane.

References

- Aikin, A. C., J. R. Herman, E. J. Maier, C. J. McQuillan (1982), Atmospheric chemistry of ethane and ethylene, J. Geophys. Res., 87(C4), 3105, doi:10.1029/JC087iC04p03105.
- Angelbratt, J., J. Mellqvist, D. Simpson, J. E. Jonson, T. Blumenstock, T. Borsdorff P. Duchatelet, F. Forster, F. Hase, E. Mahieu, M. De Mazière, J. Notholt, A. K. Petersen, U. Raffalski, C. Servais, R. Sussmann, T. Warneke, C. Vigouroux (2011), Carbon monoxide (CO) and ethane (C2H6) trends from ground-based solar FTIR measurements at six European stations, comparison and sensitivity analysis with the EMEP model, Atmos. Chem. Phys., 11(17), 9253–9269, doi:10.5194/acp-11-9253-2011.
- Atkinson, R., D. L. Baulch, R. A. Cox, J. N. Crowley, R. F. Hampson, R. G. Hynes, M. E. Jenkin, M. J. Rossi, J. Troe, and IUPAC Subcommittee (2006), Evaluated kinetic and photochemical data for atmospheric chemistry: Volume II: gas phase reactions of organic species, Atmos. Chem. Phys., 6(11), 3625–4055, doi:10.5194/acp-6-3625-2006.
- Aydin, M., K. R. Verhulst, E. S. Saltzman, M. O. Battle, S. a Montzka, D. R. Blake, Q. Tang, and M. J. Prather (2011), Recent decreases in fossil-fuel emissions of ethane and methane derived from firn air., Nature, 476(7359), 198–201, doi:10.1038/nature10352.
- Bader, W. (2011), Extension of the long--term total column time series of atmospheric methane above the Jungfraujoch station: analysis of grating infrared spectra between 1977 and 1989., Master's thesis, Department of Geography, University of Liège.
- Bader, W., T. Stavrakou, J.-F. Muller, S. Reimann, C. D. Boone, J. J. Harrison, O. Flock, B. Bovy, B. Franco, B. Lejeune, C. Servais, E. Mahieu (2014), Long-term evolution and seasonal modulation of methanol above Jungfraujoch (46.5° N, 8.0° E): optimization of the retrieval strategy, comparison with model simulations and independent observations, Atmos. Meas. Tech., 7(11), 3861–3872, doi:10.5194/amt-7-3861-2014.
- Baker, V. R., J. R., Everett, M. Morisawa, N. M. Short, J. M. Coleman, H. H. Roberts, O. K. Huh, A. L. Bloom, R. W. Jr. Blair, A. S. Walker, R. S. Jr. Williams, P. D. Jr. Lowman, J. B. Garvin, R. S. Hayden (1986), Geomorphology from space, edited by N. M. S. Short and R. W. J. Blair, United States Government Printing.
- Barret, B., M. De Mazière, P. Demoulin (2002), Retrieval and characterization of ozone profiles from solar infrared spectra at the Jungfraujoch, J. Geophys. Res. Atmos., 107(D24), 4788, doi:10.1029/2001JD001298.
- Bates, D. R., and M. Nicolet (1950), Atmospheric Hydrogen, Publ. Astron. Soc. Pacific, 62, 106, doi:10.1086/126244.
- Bates, N., Y. Astor, M. Church, K. Currie, J. Dore, M. Gonaález-Dávila, L. Lorenzoni, F. Muller-Karger, J. Olafsson, M. Santa-Casiano (2014), A Time-Series View of Changing Ocean Chemistry Due to Ocean Uptake of Anthropogenic CO2 and Ocean Acidification, Oceanography, 27(1), 126–141, doi:10.5670/oceanog.2014.16.
- Beer, R., M. W. Shephard, S. S. Kulawik, S. A. Clough, A. Eldering, K. W. Bowman, S. P. Sander, B. M. Fisher, V. H. Payne, M. Luo, G. B. Osterman, J. R. Worden (2008), First satellite observations of lower tropospheric ammonia and methanol, Geophys. Res. Lett., 35(9), L09801, doi:10.1029/2008GL033642.

- Bergamaschi, P., S. Houweling, A. Segers, M. Krol, C. Frankenberg, R. A. Scheepmaker, E. Dlugokencky, S. C. Wofsy, E. A. Kort, C. Sweeney, T. Schuck, C. Brenninkmeijer, H. Chen, V. Beck, C. Gerbig (2013), Atmospheric CH_4 in the first decade of the 21st century: Inverse modeling analysis using SCIAMACHY satellite retrievals and NOAA surface measurements, J. Geophys. Res. Atmos., 118(13), 7350–7369, doi:10.1002/jgrd.50480.
- Bernath, P. F., C. T. McElroy, M. C. Abrams, C. D. Boone, M. Butler, C. Camy-Peyret, M. Carleer, C. Clerbaux, P-F. Coheur, R. Colin, P. DeCola, M. DeMazière, J. R. Drummond, D. Dufour, W. F. J. Evans, H. Fast, D. Fussen, K. Gilbert, D. E. Jennings, E. J. Llewellyn, R. P. Lowe, E. Mahieu, J. C. McConnell, M. McHugh, S. D. McLeod, R. Michaud, C. Midwinter, R. Nassar, F. Nichitiu, C. Nowlan, C. P. Rinsland, Y. J. Rochon, N. Rowlands, K. Semeniuk, P. Simon, R. Skelton, J. J. Sloan, M.-A. Soucy, K. Strong, P. Tremblay, D. Turnbull, K. A. Walker, I. Walkty, D. A. Wardle, V. Wehrle, R. Zander, J. Zou (2005), Atmospheric Chemistry Experiment (ACE): Mission overview, Geophys. Res. Lett., 32(15), L15S01, doi:10.1029/2005GL022386.
- Berntsen, T. K., and I. S. A. Isaksen (1997), A global three-dimensional chemical transport model for the troposphere 1 . Model description and CO and ozone results, J. of Geophys. Res., 102, D17, 21 239-21 280, doi: 10.1029/97JD01140.
- Bertram, T. H., A. E. Perring, P. J. Wooldridge, J. Dibb, M. A. Avery, R. C. Cohen (2013), On the export of reactive nitrogen from Asia: NOx partitioning and effects on ozone, Atmos. Chem. Phys., 13(9), 4617–4630, doi:10.5194/acp-13-4617-2013.
- Bey, I., D. J. Jacob, J. A. Logan, R. M. Yantosca (2001b), Asian chemical outflow to the Pacific in spring: Origins, pathways, and budgets, J. Geophys. Res., 106(D19), 23097, doi:10.1029/2001JD000806.
- Bey, I., D. J. Jacob, R. M. Yantosca, J. a. Logan, B. D. Field, A. M. Fiore, Q. Li, H. Y. Liu, L. J. Mickley, M. G. Schultz (2001a), Global modeling of tropospheric chemistry with assimilated meteorology: Model description and evaluation, J. Geophys. Res., 106(D19), 23073, doi:10.1029/2001JD000807.
- Blake, D. R., T.-Y. Chen, T. W. Smith, C. J.-L. Wang, O. W. Wingenter, N. J. Blake, F. S. Rowland, E. W. Mayer (1996), Three-dimensional distribution of non-methane hydrocarbons and halocarbons over the northwestern Pacific during the 1991 Pacific Exploratory Mission (PEM-West A), J. Geophys. Res., 101(D1), 1763, doi:10.1029/95JD02707.
- Bloom, A. A., J. Worden, Z. Jiang, H. Worden, T. Kurosu, C. Frankenberg, D. Schimel (2015), Remote-sensing constraints on South America fire traits by Bayesian fusion of atmospheric and surface data, Geophys. Res. Lett., 42(4), 1268–1274, doi:10.1002/2014GL062584.
- Bloom, A. A., P. I. Palmer, A. Fraser, D. S. Reay, C. Frankenberg (2010), Large-Scale Controls of Methanogenesis Inferred from Methane and Gravity Spaceborne Data, Science, 327(5963), 322–325, doi:10.1126/science.1175176.
- Boone, C. D., K. A. Walker, and P. F. Bernath (2013), Version 3 Retrievals for the Atmospheric Chemistry Experiment Fourier Transform Spectrometer (ACE-FTS), in The Atmospheric Chemistry Experiment ACE at 10: A Solar Occultation Anthology, edited by P. F. Bernath, pp. 103–127, A. Deepak Publishing, Hampton, Virignia, USA.
- Bousquet, P. et al. (2006), Contribution of anthropogenic and natural sources to atmospheric methane variability, Nature, 443(7110), 439–443, doi: 10.1038/nature05132.

- Bousquet, P. et al. (2011), Source attribution of the changes in atmospheric methane for 2006–2008, Atmos. Chem. Phys., 11(8), 3689–3700, doi:10.5194/acp-11-3689-2011.
- Bray, C., A. Perrin, D. Jacquemart, N. Lacome (2011), The v1, v4 and 3v6 bands of methyl chloride in the 3.4-µm region: Line positions and intensities, J. Quant. Spectrosc. Radiat. Transf., 112(15), 2446–2462, doi:10.1016/j.jqsrt.2011.06.018.
- Bray, C., D. Jacquemart, J. Buldyreva, N. Lacome, and a. Perrin (2012), N2-broadening coefficients of methyl chloride at room temperature, J. Quant. Spectrosc. Radiat. Transf., 113(11), 1102–1112, doi:10.1016/j.jqsrt.2012.01.028.
- Brewer, A. W. (1949), Evidence for a world circulation provided by the measurements of helium and water vapour distribution in the stratosphere, Q. J. R. Meteorol. Soc., 75(326), 351–363, doi:10.1002/qj.49707532603.
- Browell, E. V. (2003), Ozone, aerosol, potential vorticity, and trace gas trends observed at high-latitudes over North America from February to May 2000, J. Geophys. Res., 108(D4), doi:10.1029/2001JD001390.
- Brown, L. R., C. B. Farmer, C. P. Rinsland, and R. A. Toth (1987), Molecular line parameters for the atmospheric trace molecule spectroscopy experiment, Appl. Opt., 36(23), 5154–5182.
- Butchart, N. (2014), The Brewer-Dobson circulation, Rev. Geophys., 52(2), 157–184, doi:10.1002/2013RG000448.
- Cady-Pereira, K. E., M. W. Shephard, D. B. Millet, M. Luo, K. C. Wells, Y. Xiao, V. H. Payne, and J. Worden (2012), Methanol from TES global observations: retrieval algorithm and seasonal and spatial variability, Atmos. Chem. Phys., 12(17), 8189–8203, doi:10.5194/acp-12-8189-2012.
- Carpenter L. J. and S. Reimann (Lead Authors), J.B. Burkholder, C. Clerbaux, B.D. Hall, R. Hossaini, J.C. Laube, and S.A. Yvon-Lewis (2014), Ozone-Depleting Substances (ODSs) and Other Gases of Interest to the Montreal Protocol, Chapter 1 in Scientific Assessment of Ozone Depletion: 2014, Global Ozone Research and Monitoring Project –Report No. 55, World Meteorological Organization, Geneva, Switzerland.
- Carpenter, L. J., A. C. Lewis, J. R. Hopkins, K. A. Read, I. D. Longley, and M. W. Gallagher (2004), Uptake of methanol to the North Atlantic Ocean surface, Global Biogeochem. Cycles, 18(4), GB4027, doi:10.1029/2004GB002294.
- Chameides, W., and J. C. G. Walker (1973), A photochemical theory of tropospheric ozone, J. Geophys. Res., 78(36), 8751–8760, doi:10.1029/JC078i036p08751.
- Chang, L., S. Palo, M. Hagan, J. Richter, R. Garcia, D. Riggin, and D. Fritts (2008), Structure of the migrating diurnal tide in the Whole Atmosphere Community Climate Model (WACCM), Adv. Sp. Res., 41(9), 1398–1407, doi:10.1016/j.asr.2007.03.035.
- Chapman, S. (1930), A theory of upper-atmospheric ozone, Mem. R. Meteorol. Soc., 3(26), 103—125.
- Chatfield, R. B., J. A. Vastano, L. Li, G. W. Sachse, and V. S. Connors (1998), The Great African Plume from biomass burning: Generalizations from a three-dimensional study of TRACE A carbon monoxide, J. Geophys. Res., 103(D21), 28059, doi:10.1029/97JD03363.
- Chen, D., Y. Wang, M. B. McElroy, K. He, R. M. Yantosca, and P. Le Sager (2009), Regional CO pollution and export in China simulated by the high-resolution nested-grid GEOS-Chem model, Atmos. Chem. Phys., 9(11), 3825–3839, doi:10.5194/acp-9-3825-2009.

- Chen, Y.-H. (2005), Atmospheric modeling of high- and low-frequency methane observations: Importance of interannually varying transport, J. Geophys. Res., 110(D10), D10303, doi:10.1029/2004JD005542.
- Chen, Y.-H., and R. G. Prinn (2006), Estimation of atmospheric methane emissions between 1996 and 2001 using a three-dimensional global chemical transport model, J. Geophys. Res. Atmos., 111(D10), D10307, doi:10.1029/2005JD006058.
- Collaud Coen, M., E. Weingartner, M. Furger, S. Nyeki, A. S. H. Prévôt, M. Steinbacher, and U. Baltensperger (2011), Aerosol climatology and planetary boundary influence at the Jungfraujoch analyzed by synoptic weather types, Atmos. Chem. Phys., 11(12), 5931–5944, doi:10.5194/acp-11-5931-2011.
- Collins, W. J., R. G. Derwent, C. E. Johnson, and D. S. Stevenson (2002), The Oxidation of Organic Compounds in the Troposphere and their Global Warming Potentials, Clim. Change, 52(4), 453–479, doi:10.1023/A:1014221225434.
- Connes, P. (1971), High resolution and high information Fourier spectroscopy, in 1970-Aspen International Conference Fourier Spectroscopy, edited by G. A. Vanasse, A. T. J. Stair, and D. J. Backer, p. 121, United States Air Force, Air Force Systems Command, Air Force Cambridge Research Laboratories.
- Connor, B. J., D. E. Siskind, J. J. Tsou, A. Parrish, and E. E. Remsberg (1994), Ground-based microwave observations of ozone in the upper stratosphere and mesosphere, J. Geophys. Res., 99(D8), 16757, doi:10.1029/94JD01153.
- Cox, C. J., V. P. Walden, and P. M. Rowe (2012), A comparison of the atmospheric conditions at Eureka, Canada, and Barrow, Alaska (2006-2008), J. Geophys. Res. Atmos., 117(D12), n/a–n/a, doi:10.1029/2011JD017164.
- Crutzen, P. J. (1970), The influence of nitrogen oxide on the atmospheric ozone content, Q. J. R. Meteorol. Soc., 96, 320.
- Crutzen, P. J. (1973), A discussion of the chemistry of some minor constituents in the stratosphere and troposphere, Pure Appl. Geophys., 106, 1385.
- Delbouille, L., and G. Roland (1963), Photometric atlas of the solar spectrum from λ 7498 to λ 12016.
- Delbouille, L., and G. Roland (1995), High-resolution solar and atmospheric spectroscopy from the Jungfraujoch high-altitude station, Opt. Eng., 34(9), 2736, doi:10.1117/12.205676.
- Delbouille, L., L. Neven, and G. Roland (1973), Photometric atlas of the solar spectrum from λ 3000 to λ 10000.
- Delmas, R., G. Mégie, and V.-H. Peuch (2005), Physique et chimie de l'atmosphère, Bélin., Echelles, Paris.
- Dlugokencky, E. J. (2003), Atmospheric methane levels off: Temporary pause or a new steady-state?, Geophys. Res. Lett., 30(19), 1992, doi:10.1029/2003GL018126.
- Dlugokencky, E. J. et al. (2009), Observational constraints on recent increases in the atmospheric CH 4 burden, Geophys. Res. Lett., 36(18), L18803, doi:10.1029/2009GL039780.
- Dlugokencky, E. J., L. P. Steele, P. M. Lang, and K. A. Masarie (1994), The growth rate and distribution of atmospheric methane, J. Geophys. Res., 99(D8), 17021, doi:10.1029/94JD01245.

- Dobson, G. M. B. (1956), Origin and Distribution of the Polyatomic Molecules in the Atmosphere, Proc. R. Soc. A Math. Phys. Eng. Sci., 236(1205), 187–193, doi:10.1098/rspa.1956.0127.
- Dobson, G. M. B., D. N. Harrison, and J. Lawrence (1929), Measurements of the Amount of Ozone in the Earth's Atmosphere and Its Relation to Other Geophysical Conditions. Part III, Proc. R. Soc. A Math. Phys. Eng. Sci., 122(790), 456–486, doi:10.1098/rspa.1929.0034.
- doi:10.1016/j.scitotenv.2007.10.018.
- Drayson, S. R. (1976), Rapid computation of the Voigt profile, J. Quant. Spectrosc. Radiat. Transf., 16(7), 611–614, doi:10.1016/0022-4073(76)90029-7.
- Duchatelet, P. (2011), Fluorine in the atmosphere: Inorganic fluorine budget and long--term trends based on FTIR measurements at Jungfraujoch., Institute of Astrophysics and Geophysics, University of Liège.
- Duchatelet, P., P. Demoulin, F. Hase, R. Ruhnke, W. Feng, M. P. Chipperfield, P. F. Bernath, C. D. Boone, K. A. Walker, and E. Mahieu (2010), Hydrogen fluoride total and partial column time series above the Jungfraujoch from long-term FTIR measurements: Impact of the line-shape model, characterization of the error budget and seasonal cycle, and comparison with satellite and model data, J. Geophys. Res., 115(D22), doi:10.1029/2010JD014677.
- Dufour, G., C. D. Boone, C. P. Rinsland, and P. F. Bernath (2006), First space-borne measurements of methanol inside aged southern tropical to mid-latitude biomass burning plumes using the ACE-FTS instrument, Atmos. Chem. Phys., 6(11), 3463–3470, doi:10.5194/acp-6-3463-2006.
- Dufour, G., S. Szopa, D. a. Hauglustaine, C. D. Boone, C. P. Rinsland, and P. F. Bernath (2007), The influence of biogenic emissions on upper-tropospheric methanol as revealed from space, Atmos. Chem. Phys. Discuss., 7(3), 9183–9202, doi:10.5194/acpd-7-9183-2007.
- Duncan, B. N. (2003), Interannual and seasonal variability of biomass burning emissions constrained by satellite observations, J. Geophys. Res., 108(D2), 4100, doi:10.1029/2002JD002378.
- Duncan, B. N., J. A. Logan, I. Bey, I. A. Megretskaia, R. M. Yantosca, P. C. Novelli, N. B. Jones, and C. P. Rinsland (2007), Global budget of CO, 1988–1997: Source estimates and validation with a global model, J. Geophys. Res. Atmos., 112(D22), D22301, doi:10.1029/2007JD008459.
- Dunkerton, T. (1978), On the Mean Meridional Mass Motions of the Stratosphere and Mesosphere, J. Atmos. Sci., 35(12), 2325–2333, doi:10.1175/1520-0469(1978)035<2325:OTMMMM>2.0.CO;2.
- Esposito, F., G. Grieco, G. Masiello, G. Pavese, R. Restieri, C. Serio, and V. Cuomo (2007), Intercomparison of line-parameter spectroscopic databases using downwelling spectral radiance, Q. J. R. Meteorol. Soc., 133(S3), 191–202, doi:10.1002/qj.131.
- Fall, R. (2003), Abundant Oxygenates in the Atmosphere: A Biochemical Perspective, Chem. Rev., 103(12), 4941–4952, doi:10.1021/cr0206521.
- Farman, J. C., B. G. Gardiner, and J. D. Shanklin (1985), Large losses of total ozone in Antarctica reveal seasonal ClO_x/NO_x interaction, Nature, 315(6016), 207–210, doi:10.1038/315207a0.
- Fehsenfeld, F. C., G. Ancellet, T. S. Bates, A. H. Goldstein, R. M. Hardesty, R. Honrath, K. S. Law, A. C. Lewis, R. Leaitch, S. McKeen, J. Meagher, D. D. Parrish, A. A. P. Pszenny, P. B. Russell, H. Schlager, J. Seinfeld, R. Talbot, R. Zbinden, (2006), International Consortium for Atmospheric Research on Transport and Transformation (ICARTT): North America to Europe—Overview of the 2004 summer field study, J. Geophys. Res. Atmos., 111(D23), D23S01, doi:10.1029/2006JD007829.

- Fischer, E. V., D. J. Jacob, R. M. Yantosca, M. P. Sulprizio, D. B. Millet, J. Mao, F. Paulot, H. B. Singh, A. Roiger, L. Ries, R. W. Talbot, K. Dzepina, S. Pandey Deolal (2014), Atmospheric peroxyacetyl nitrate (PAN): a global budget and source attribution, Atmos. Chem. Phys., 14(5), 2679–2698, doi:10.5194/acp-14-2679-2014.
- Fishman, J., J. M. Hoell, R. D. Bendura, R. J. McNeal, and V. W. J. H. Kirchhoff (1996), NASA GTE TRACE A experiment (September–October 1992): Overview, J. Geophys. Res., 101(D19), 23865, doi:10.1029/96JD00123.
- Fogal, P. F., L. M. LeBlanc, and J. R. Drummond (2013), The Polar Environment Atmospheric Research Laboratory (PEARL): Sounding the Atmosphere at 80° North., Arctic, 66(3), 377–386.
- Forster, P. et al. (2007), Changes in Atmospheric Constituents and in Radiative Forcing. In: Climate Change 2007: The Physical Science Basis. Contribution of Working Group I to the Fourth Assessment Report of the Intergovernmental Panel on Climate Change, in IPCC, edited by S. Solomon, D. Qin, M. Manning, Z. Chen, M. Marquis, K. B. Averyt, M. Tignor, and H. L. Miller, Cambridge, United Kingdom and New York, NY, USA.
- Franco, B. et al. (2015a), Retrieval of ethane from ground-based FTIR solar spectra using improved spectroscopy: Recent burden increase above Jungfraujoch, J. Quant. Spectrosc. Radiat. Transf., 160, 36–49, doi:10.1016/j.jqsrt.2015.03.017.
- Franco, B. et al. (2015b), Retrievals of formaldehyde from ground-based FTIR and MAX-DOAS observations at the Jungfraujoch station and comparisons with GEOS-Chem and IMAGES model simulations, Atmos. Meas. Tech., 8(4), 1733–1756, doi:10.5194/amt-8-1733-2015.
- Frankenberg, C., I. Aben, P. Bergamaschi, E. J. Dlugokencky, R. van Hees, S. Houweling, P. van der Meer, R. Snel, and P. Tol (2011), Global column-averaged methane mixing ratios from 2003 to 2009 as derived from SCIAMACHY: Trends and variability, J. Geophys. Res., 116(D4), D04302, doi:10.1029/2010JD014849.
- Frankenberg, C., P. Bergamaschi, A. Butz, S. Houweling, J. F. Meirink, J. Notholt, A. K. Petersen, H. Schrijver, T. Warneke, and I. Aben (2008), Tropical methane emissions: A revised view from SCIAMACHY onboard ENVISAT, Geophys. Res. Lett., 35(15), L15811, doi:10.1029/2008GL034300.
- Fraser, A., C. C. Miller, P. I. Palmer, N. M. Deutscher, N. B. Jones, and D. W. T. Griffith (2011), The Australian methane budget: Interpreting surface and train-borne measurements using a chemistry transport model, J. Geophys. Res., 116(D20), D20306, doi:10.1029/2011JD015964.
- Fung, I., J. John, J. Lerner, E. Matthews, M. Prather, L. P. Steele, and P. J. Fraser (1991), Three-dimensional model synthesis of the global methane cycle, J. Geophys. Res., 96(D7), 13033, doi:10.1029/91JD01247.
- Galbally, I. E., and W. Kirstine (2002), The Production of Methanol by Flowering Plants and the Global Cycle of Methanol, J. Atmos. Chem., 43(3), 195–229, doi:10.1023/A:1020684815474.
- Gardiner, T. et al. (2008), Trend analysis of greenhouse gases over Europe measured by a network of ground-based remote FTIR instruments, Atmos. Chem. Phys., 8(22), 6719–6727, doi:10.5194/acp-8-6719-2008.

- Glatthor, N., T. von Clarmann, G. P. Stiller, B. Funke, M. E. Koukouli, H. Fischer, U. Grabowski, M. Hoepfner, S. Kellmann, and A. Linden (2009), Large-scale upper tropospheric pollution observed by MIPAS HCN and C_2H_6 global distributions, Atmos. Chem. Phys., 9(24), 9619–9634, doi:10.5194/acp-9-9619-2009.
- Griffith, D. W. T., N. B. Jones, and W. A. Matthews (1998), Interhemispheric ratio and annual cycle of carbonyl sulfide (OCS) total column from ground-based solar FTIR spectra, J. Geophys. Res., 103(D7), 8447, doi:10.1029/97JD03462.
- Grooß, J.-U., and J. M. Russell (2005), Technical note: A stratospheric climatology for O_3, H_2O, CH_4, NO_x, HCl and HF derived from HALOE measurements, Atmos. Chem. Phys., 5(10), 2797–2807, doi:10.5194/acp-5-2797-2005.
- Gunson, M. R. et al. (1996), The Atmospheric Trace Molecule Spectroscopy (ATMOS) Experiment: Deployment on the ATLAS space shuttle missions, Geophys. Res. Lett., 23(17), 2333–2336, doi:10.1029/96GL01569.
- Gunson, M. R., C. B. Farmer, R. H. Norton, R. Zander, C. P. Rinsland, J. H. Shaw, and B.-C. Gao (1990), Measurements of CH4, N2O, CO, H2O, and O3 in the middle atmosphere by the Atmospheric Trace Molecule Spectroscopy experiment on Spacelab 3, J. Geophys. Res., 95(D9), 13867, doi:10.1029/JD095iD09p13867.
- Hao, W. M., and D. E. Ward (1993), Methane production from global biomass burning, J. Geophys. Res., 98(D11), 20657, doi:10.1029/93JD01908.
- Harrison, J. J., N. D. C. Allen, and P. F. Bernath (2010), Infrared absorption cross sections for ethane (C_2H_6) in the 3 μm region, J. Quant. Spectrosc. Radiat. Transf., 111(3), 357–363, doi:10.1016/j.jqsrt.2009.09.010.
- Harrison, J. J., N. D. C. Allen, and P. F. Bernath (2012), Infrared absorption cross sections for methanol, J. Quant. Spectrosc. Radiat. Transf., 113(17), 2189–2196, doi:10.1016/j.jqsrt.2012.07.021.
- Hase, F., J. W. Hannigan, M. T. Coffey, A. Goldman, M. Höpfner, N. B. Jones, C. P. Rinsland, and S. W. Wood (2004), Intercomparison of retrieval codes used for the analysis of high-resolution, ground-based FTIR measurements, J. Quant. Spectrosc. Radiat. Transf., 87(1), 25–52, doi:10.1016/j.jqsrt.2003.12.008.
- Hase, F., P. Demoulin, A. J. Sauval, G. C. Toon, P. F. Bernath, A. Goldman, J. W. Hannigan, and C. P. Rinsland (2006), An empirical line-by-line model for the infrared solar transmittance spectrum from 700 to 5000 cm^{-1}, J. Quant. Spectrosc. Radiat. Transf., 102(Article), 450–463, doi:10.1016/j.jqsrt.2006.02.026.
- Heikes, B. G. et al. (2002), Atmospheric methanol budget and ocean implication, Global Biogeochem. Cycles, 16(4), 1133, doi:10.1029/2002GB001895.
- Henne, S., M. Furger, and A. H. Prévôt (2005), Climatology of Mountain Venting–Induced Elevated Moisture Layers in the Lee of the Alps, J. Appl. Meteorol., 44(5), 620–633, doi:10.1175/JAM2217.1.
- Henne, S., M. Furger, S. Nyeki, M. Steinbacher, B. Neininger, S. F. J. de Wekker, J. Dommen, N. Spichtinger, A. Stohl, and A. S. H. Prévôt (2004), Quantification of topographic venting of boundary layer air to the free troposphere, Atmos. Chem. Phys., 4(2), 497–509, doi:10.5194/acp-4-497-2004.
- Holton, J. R., P. H. Haynes, M. E. McIntyre, A. R. Douglass, R. B. Rood, and L. Pfister (1995), Stratosphere-troposphere exchange, Rev. Geophys., 33(4), 403, doi:10.1029/95RG02097.

- Hough, A. M. (1991), Development of a two-dimensional global tropospheric model: Model chemistry, J. Geophys. Res., 96(D4), 7325, doi:10.1029/90JD01327.
- Huang, X., and Y. L. Yung (2004), A Common Misunderstanding about the Voigt Line Profile, J. Atmos. Sci., 61(13), 1630–1632, doi:10.1175/1520-0469(2004)061<1630:ACMATV>2.0.CO;2.
- Intergovernmental Panel on Climate Change, IPCC (2013) Climate Change 2013: The Physical Science Basis. Contribution of Working Group I to the Fifth Assessment Report of the Intergovernmental Panel on Climate Change [Stocker, T.F., D. Qin, G.-K. Plattner, M. Tignor, S.K. Allen, J. Boschung, A. Nauels, Y. Xia, V. Bex and P.M. Midgley (eds.)]. Cambridge University Press, Cambridge, United Kingdom and New York, NY, USA, 1535 pp, doi:10.1017/CBO9781107415324.
- Ito, A. (2010), Evaluation of the impacts of defoliation by tropical cyclones on a Japanese forest's carbon budget using flux data and a process-based model, J. Geophys. Res., 115(G4), doi:10.1029/2010JG001314.
- Jacob, D. J. (1999), Introduction to atmospheric chemistry, Princeton University Press, Princeton.
- Jacob, D. J. (2002), Atmospheric budget of acetone, J. Geophys. Res., 107(D10), doi:10.1029/2001JD000694.
- Jacob, D. J. (2005), Global budget of methanol: Constraints from atmospheric observations, J. Geophys. Res., 110(D8), D08303, doi:10.1029/2004JD005172.
- Jacob, D. J. (2007), Lectures on inverse modelling, p. 25, University of Harvard, Harvard.
- Jiménez, E., M. Gilles, and A. Ravishankara (2003), Kinetics of the reactions of the hydroxyl radical with CH_3OH and C_2H_5OH between 235 and 360 K, J. Photochem. Photobiol. A Chem., 157(2-3), 237–245, doi:10.1016/S1010-6030(03)00073-X.
- Johnston, H. (1971), Reduction of Stratospheric Ozone by Nitrogen Oxide Catalysts from Supersonic Transport Exhaust, Science, 173(3996), 517–522, doi:10.1126/science.173.3996.517.
- Kaiser, E. W., I. M. Lorkovic, and T. J. Wallington (1990), Pressure dependence of the ethene yield from the reaction ethyl radical + oxygen, J. Phys. Chem., 94(8), 3352–3354, doi:10.1021/j100371a030.
- Kaplan, J. O. (2002), Wetlands at the Last Glacial Maximum: Distribution and methane emissions, Geophys. Res. Lett., 29(6), 1079, doi:10.1029/2001GL013366.
- Karl, T., A. Guenther, C. Spirig, A. Hansel, and R. Fall (2003), Seasonal variation of biogenic VOC emissions above a mixed hardwood forest in northern Michigan, Geophys. Res. Lett., 30(23), 2186, doi:10.1029/2003GL018432.
- Khalil, M. a. K., and R. a. Rasmussen (1983), Sources, sinks, and seasonal cycles of atmospheric methane, J. Geophys. Res., 88(C9), 5131, doi:10.1029/JC088iC09p05131.
- Kirschke, S. et al. (2013), Three decades of global methane sources and sinks, Nat. Geosci., 6(10), 813–823, doi:10.1038/ngeo1955.
- Krol, M., and J. Lelieveld (2003), Can the variability in tropospheric OH be deduced from measurements of 1,1,1-trichloroethane (methyl chloroform)?, J. Geophys. Res., 108(D3), doi:10.1029/2002JD002423.
- Kulawik, S. S. et al. (2015), Consistent evaluation of GOSAT, SCIAMACHY, CarbonTracker, and MACC through comparisons to TCCON, Atmos. Meas. Tech. Discuss., 8(6), 6217–6277, doi:10.5194/amtd-8-6217-2015.

- Kurylo, M. J. (1991), Network for the detection of stratospheric change, in Remote sensing of atmospheric chemistry, edited by J. L. McElroy and R. J. McNeal, pp. 168–174, Society of Photo-Optical Instrumentation Engineers, Bellingham, WA, United States, Orlando, FL.
- Kuze, A., H. Suto, M. Nakajima, and T. Hamazaki (2009), Thermal and near infrared sensor for carbon observation Fourier-transform spectrometer on the Greenhouse Gases Observing Satellite for greenhouse gases monitoring, Appl. Opt., 48(35), 6716, doi:10.1364/AO.48.006716.
- Laffineur, Q., M. Aubinet, N. Schoon, C. Amelynck, J.-F. Müller, J. Dewulf, H. Van Langenhove, K. Steppe, and B. Heinesch (2012), Abiotic and biotic control of methanol exchanges in a temperate mixed forest, Atmos. Chem. Phys., 12(1), 577–590, doi:10.5194/acp-12-577-2012.
- Langerock, B., M. De Mazière, F. Hendrick, C. Vigouroux, F. Desmet, B. Dils, and S. Niemeijer (2015), Description of algorithms for co-locating and comparing gridded model data with remote-sensing observations, Geosci. Model Dev., 8(3), 911–921, doi:10.5194/gmd-8-911-2015.
- Lattanzi, F., C. di Lauro, and J. Vander Auwera (2011), Toward the understanding of the high resolution infrared spectrum of C_2H_6 near 3.3µm, J. Mol. Spectrosc., 267(1-2), 71–79, doi:10.1016/j.jms.2011.02.003.
- Legreid, G., D. Folini, J. Staehelin, J. Balzani Lööv, M. Steinbacher, and S. Reimann (2008), Measurements of organic trace gases including oxygenated volatile organic compounds at the high alpine site Jungfraujoch (Switzerland): Seasonal variation and source allocations, J. Geophys. Res. Atmos., 113(D5), doi:10.1029/2007JD008653.
- Lelieveld, J. (2002), Stability of tropospheric hydroxyl chemistry, J. Geophys. Res., 107(D23), 4715, doi:10.1029/2002JD002272.
- Liu, H., D. J. Jacob, I. Bey, and R. M. Yantosca (2001), Constraints from 210 Pb and 7 Be on wet deposition and transport in a global three-dimensional chemical tracer model driven by assimilated meteorological fields, J. Geophys. Res. Atmos., 106(D11), 12109–12128, doi:10.1029/2000JD900839.
- Logan, J. A., M. J. Prather, S. C. Wofsy, and M. B. McElroy (1981), Tropospheric chemistry: A global perspective, J. Geophys. Res., 86(C8), 7210, doi:10.1029/JC086iC08p07210.
- Madronich, S., and J. G. Calvert (1990), Permutation reactions of organic peroxy radicals in the troposphere, J. Geophys. Res. Atmos., 95(D5), 5697–5715, doi:10.1029/JD095iD05p05697.
- Mahieu, E. et al. (2014), Spectrometric monitoring of atmospheric carbon tetrafluoride (CF_4) above the Jungfraujoch station since 1989: evidence of continued increase but at a slowing rate, Atmos. Meas. Tech., 7(1), 333–344, doi:10.5194/amt-7-333-2014.
- Mahieu, E., R. Zander, L. Delbouille, P. Demoulin, G. Roland, and C. Servais (1997), Observed trends in total vertical column abundances of atmospheric gases from IR solar spectra recorded at the Jungfraujoch, J. Atmos. Chem., 28(1-3), 227–243.
- Mahieu, E., W. Bader, and B. Franco (2015), Recent results derived from regular ground-based FTIR at the Jungfraujoch and other NDACC stations, in ACE Science Team Meeting, p. 24, Waterloo, ON, Canada.
- Malbrouck, R. (1977), Spectroscopie à très haute résolution par transformée de Fourier: Application à l'étude du spectre solaire., University of Liège.
- Mao, J. et al. (2010), Chemistry of hydrogen oxide radicals (HOx) in the Arctic troposphere in spring, Atmos. Chem. Phys., 10(13), 5823–5838, doi:10.5194/acp-10-5823-2010.

- McClatchey, R. A., W. S. Benedict, S. A. Clough, D. E. Burch, R. F. Calfee, K. Fox, L. S. Rothman, and J. S. Garing (1973), AFCRL atmospheric absorption line parameters compilation., AFCRL-TR-73-0096, 434, 78 pp.
- Mégie, G. (1989), Ozone. L'équilibre rompu, Presses du CNRS.
- Meier, A., G. C. Toon, C. P. Rinsland, A. Goldman, and F. Hase (2004), Spectroscopic Atlas of Atmospheric Microwindows in the Middle Infra-Red, Kiruna, Sweden.
- Migeotte, M., and L. Neven (1950), Détection du monoxide de carbone dans l'atmosphère terrestre à 3580 mètres d'altitude, Physica, 16, 423.
- Miller, J. A., S. J. Klippenstein, and S. H. Robertson (2000), A theoretical analysis of the reaction between ethyl and molecular oxygen, Proc. Combust. Inst., 28(2), 1479–1486, doi:10.1016/S0082-0784(00)80544-5.
- Millet, D. B. et al. (2006), Formaldehyde distribution over North America: Implications for satellite retrievals of formaldehyde columns and isoprene emission, J. Geophys. Res. Atmos., 111(D24), D24S02, doi:10.1029/2005JD006853.
- Millet, D. B. et al. (2008), New constraints on terrestrial and oceanic sources of atmospheric methanol, Atmos. Chem. Phys., 8(23), 6887–6905, doi:10.5194/acp-8-6887-2008.
- Molina, M. J., and F. S. Rowland (1974), Stratospheric sink for chlorofluoromethanes: chlorine atom catalyzed destruction of ozone, Nature, 249(5460), 810–812, doi:10.1038/249810a0.
- Montzka, S. A., M. Krol, E. Dlugokencky, B. Hall, P. Jockel, and J. Lelieveld (2011), Small Interannual Variability of Global Atmospheric Hydroxyl, Science, 331(6013), 67–69, doi:10.1126/science.1197640.
- Müller, J.-F., and G. Brasseur (1995), IMAGES: A three-dimensional chemical transport model of the global troposphere, J. Geophys. Res., 100(D8), 16445, doi:10.1029/94JD03254.
- Müller, J.-F., and G. Brasseur (1999), Sources of upper tropospheric HO X : A three-dimensional study, J. Geophys. Res., 104(D1), 1705, doi:10.1029/1998JD100005.
- Murgatroyd, R. J., and F. Singleton (1961), Possible meridional circulations in the stratosphere and mesosphere, Q. J. R. Meteorol. Soc., 87(372), 125–135, doi:10.1002/qj.49708737202.
- Nielsen, A. H., and M. Migeotte (1952), Abundance and vertical distribution of telluric methane from measurements at 3580 meters elevation, Annu. Rev. Astron. Phys., 15, 134.
- Nisbet, E. G., E. J. Dlugokencky, and P. Bousquet (2014), Methane on the rise-again., Science, 343(6170), 493–5, doi:10.1126/science.1247828.
- Notholt, J., G. C. Toon, R. Lehmann, B. Sen, and J.-F. Blavier (1997), Comparison of Arctic and Antarctic trace gas column abundances from ground-based Fourier transform infrared spectrometry, J. Geophys. Res., 102(D11), 12863, doi:10.1029/97JD00358.
- Nyeki, S. et al. (2000), Convective boundary layer evolution to 4 km a.s.l over High-Alpine terrain: airborne Lidar observations in the Alps, Geophys. Res. Lett., 27(5), 689–692.
- Park, R. J., D. J. Jacob, B. D. Field, R. M. Yantosca, and M. Chin (2004), Natural and transboundary pollution influences on sulfate-nitrate-ammonium aerosols in the United States: Implications for policy, J. Geophys. Res., 109(D15), doi:10.1029/2003JD004473.
- Park, R., D. Jacob, N. Kumar, and R. Yantosca (2006), Regional visibility statistics in the United States: Natural and transboundary pollution influences, and implications for the Regional Haze Rule, Atmos. Environ., 40(28), 5405–5423, doi:10.1016/j.atmosenv.2006.04.059.

- Parrella, J. P., D. J. Jacob, Q. Liang, Y. Zhang, L. J. Mickley, B. Miller, M. J. Evans, X. Yang, J. A. Pyle, N. Theys, M. Van Roozendael. (2012), Tropospheric bromine chemistry: implications for present and pre-industrial ozone and mercury, Atmos. Chem. Phys., 12(15), 6723–6740, doi:10.5194/acp-12-6723-2012.
- Paton-Walsh, C., N. M. Deutscher, D. W. T. Griffith, B. W. Forgan, S. R. Wilson, N. B. Jones, and D. P. Edwards (2010), Trace gas emissions from savanna fires in northern Australia, J. Geophys. Res., 115(D16), doi:10.1029/2009JD013309.
- Paton-Walsh, C., S. R. Wilson, N. B. Jones, and D. W. T. Griffith (2008), Measurement of methanol emissions from Australian wildfires by ground-based solar Fourier transform spectroscopy, Geophys. Res. Lett., 35(8), L08810, doi:10.1029/2007GL032951.
- Pickett-Heaps, C. A., D. J. Jacob, K. J. Wecht, E. A. Kort, S. C. Wofsy, G. S. Diskin, D. E. J. Worthy, J. O. Kaplan, I. Bey, and J. Drevet (2011), Magnitude and seasonality of wetland methane emissions from the Hudson Bay Lowlands (Canada), Atmos. Chem. Phys., 11(8), 3773–3779, doi:10.5194/acp-11-3773-2011.
- Pine, A. S., and C. P. Rinsland (1999), The role of torsional hot bands in modeling atmospheric ethane, J. Quant. Spectrosc. Radiat. Transf., 62(4), 445–458.
- Pine, A. S., and W. J. Lafferty (1981), Torsional splittings and assignments of the Doppler-limited spectrum of ethane in the CH stretching region., J. Res. Natl. Bur. Stand. (1934)., 87(3), 237–256.
- Pison, I., B. Ringeval, P. Bousquet, C. Prigent, and F. Papa (2013), Stable atmospheric methane in the 2000s: key-role of emissions from natural wetlands, Atmos. Chem. Phys., 13(23), 11609–11623, doi:10.5194/acp-13-11609-2013.
- Plumb, R. A. (2002), Stratospheric Transport., J. Meteorol. Soc. Japan, 80(4B), 793–809, doi:10.2151/jmsj.80.793.
- Pougatchev, N. S., B. J. Connor, and C. P. Rinsland (1995), Infrared measurements of the ozone vertical distribution above Kitt Peak, J. Geophys. Res., 100(D8), 16689, doi:10.1029/95JD01296.
- Pozzer, a., J. Pollmann, D. Taraborrelli, P. Jöckel, D. Helmig, P. Tans, J. Hueber, and J. Lelieveld (2010), Observed and simulated global distribution and budget of atmospheric C2-C5 alkanes, Atmos. Chem. Phys., 10(9), 4403–4422, doi:10.5194/acp-10-4403-2010.
- Prather, M. J., and J. Hsu (2010), Coupling of Nitrous Oxide and Methane by Global Atmospheric Chemistry, Science, 330(6006), 952–954, doi:10.1126/science.1196285.
- Prather, M. J., C. D. Holmes, and J. Hsu (2012), Reactive greenhouse gas scenarios: Systematic exploration of uncertainties and the role of atmospheric chemistry, Geophys. Res. Lett., 39(9), n/a–n/a, doi:10.1029/2012GL051440.
- Razavi, a., F. Karagulian, L. Clarisse, D. Hurtmans, P. F. Coheur, C. Clerbaux, J. F. Müller, and T. Stavrakou (2011), Global distributions of methanol and formic acid retrieved for the first time from the IASI/MetOp thermal infrared sounder, Atmos. Chem. Phys., 11(2), 857–872, doi:10.5194/acp-11-857-2011.
- Reimann, S. (2004), Halogenated greenhouse gases at the Swiss High Alpine Site of Jungfraujoch (3580 m a.s.l): Continuous measurements and their use for regional European source allocation, J. Geophys. Res., 109(D5), doi:10.1029/2003JD003923.
- Rigby, M. et al. (2008), Renewed growth of atmospheric methane, Geophys. Res. Lett., 35(22), L22805, doi:10.1029/2008GL036037.

- Ringeval, B., N. de Noblet-Ducoudré, P. Ciais, P. Bousquet, C. Prigent, F. Papa, and W. B. Rossow (2010), An attempt to quantify the impact of changes in wetland extent on methane emissions on the seasonal and interannual time scales, Global Biogeochem. Cycles, 24(2), doi:10.1029/2008GB003354.
- Rinsland, C. P. (2005), Atmospheric Chemistry Experiment (ACE) measurements of elevated Southern Hemisphere upper tropospheric CO, C2H6, HCN, and C2H2 mixing ratios from biomass burning emissions and long-range transport, Geophys. Res. Lett., 32(20), doi:10.1029/2005GL024214.
- Rinsland, C. P., A. Goldman, F. J. Murcray, T. M. Stephen, N. S Pougatchev, J. Fishman, S. J. David, R. D. Blatherwick, P. C. Novelli, N. B. Jones, B. J. Connor (1999), Infrared solar spectroscopic measurements of free tropospheric CO, C2H6, and HCN above Mauna Loa, Hawaii: Seasonal variations and evidence for enhanced emissions from the Southeast Asian tropical fires of 1997–1998, J. Geophys. Res., 104(D15), 18667, doi:10.1029/1999JD900366.
- Rinsland, C. P., A. Goldman, J. W. Elkins, L. S. Chiou, J. W. Hannigan, S. W. Wood, E. Mahieu, and R. Zander (2006), Long-term trend of at northern mid-latitudes: Comparison between ground-based infrared solar and surface sampling measurements, J. Quant. Spectrosc. Radiat. Transf., 97(3), 457–466, doi:10.1016/j.jqsrt.2005.07.002.
- Rinsland, C. P., A. Meier, D. W. T. Griffith, and L. S. Chiou (2001), Ground-based measurements of tropospheric CO, C2H6, and HCN from Australia at 34 degrees S latitude during 1997-1998, J. Geophys. Res., 106(D18), 20913–20924.
- Rinsland, C. P., E. Mahieu, L. Chiou, and H. Herbin (2009), First ground-based infrared solar absorption measurements of free tropospheric methanol (CH3OH): Multidecade infrared time series from Kitt Peak (31.9°N 111.6°W): Trend, seasonal cycle, and comparison with previous measurements, J. Geophys. Res., 114(D4), D04309, doi:10.1029/2008JD011003.
- Rinsland, C. P., E. Mahieu, P. Demoulin, R. Zander, C. Servais, and J.-M. Hartmann (2012), Decrease of the carbon tetrachloride (CCl_4) loading above Jungfraujoch, based on high resolution infrared solar spectra recorded between 1999 and 2011, J. Quant. Spectrosc. Radiat. Transf., 113(11), 1322–1329, doi:10.1016/j.jqsrt.2012.02.016.
- Rinsland, C. P., E. Mahieu, R. Zander, P. Demoulin, J. Forrer, and B. Buchmann (2000), Free tropospheric CO, C_2H_6, and HCN above central Europe: Recent measurements from the Jungfraujoch station including the detection of elevated columns during 1998, J. Geophys. Res., 105(D19), 24235, doi:10.1029/2000JD900371.
- Rinsland, C. P., N. B. Jones, B. J. Connor, J. A. Logan, N. S. Pougatchev, A. Goldman, F. J. Murcray, T. M. Stephen, A. S. Pine, R. Zander, E., Mahieu, P. Demoulin (1998), Northern and southern hemisphere ground-based infrared spectroscopic measurements of tropospheric carbon monoxide and ethane, J. Geophys. Res., 103(D21), 28197–28217, doi:10.1029/98JD02515.
- Rinsland, C. P., N. B. Jones, B. J. Connor, S. W. Wood, A. Goldman, T. M. Stephen, F. J. Murcray, L. S. Chiou, R. Zander, and E. Mahieu (2002), Multiyear infrared solar spectroscopic measurements of HCN, CO , C_2H_6, and C_2H_2 tropospheric columns above Lauder , New Zealand (45 °S latitude), 107, 1–12.
- Roberts, J. M., R. L. Tanner, L. Newman, V. C. Bowersox, J. W. Bottenheim, K. G. Anlauf, K. A. Brice, D. D. Parrish, F. C. Fehsenfeld, M. P. Buhr, J. F. Meagher, E. M. Bailey (1995), Relationships between PAN and ozone at sites in eastern North America, J. Geophys. Res., 100(D11), 22821, doi:10.1029/95JD01221.

- Rodgers, C. (2000), Inverse methods for atmospheric sounding, vol. 2 of Series on Atmospheric, Oceanic and Planetary Physics.
- Rodgers, C. D. (1976), Retrieval of atmospheric temperature and composition from remote measurements of thermal radiation, Rev. Geophys., 14(4), 609, doi:10.1029/RG014i004p00609.
- Rodgers, C. D. (1990), Characterization and error analysis of profiles retrieved from remote sounding measurements, J. Geophys. Res., 95(D5), 5587.
- Rodgers, C. D. (2003), Intercomparison of remote sounding instruments, J. Geophys. Res., 108(D3), doi:10.1029/2002JD002299.
- Roland, G. (1965), Spectroscopie par transformée de Fourier, University of Liège.
- Rothman, L. S. et al. (1987), The HITRAN database: 1986 edition, Appl. Opt., 26(19), 4058–4097, doi:10.1364/AO.26.004058.
- Rothman, L. S. et al. (2003), The HITRAN molecular spectroscopic database: edition of 2000 including updates through 2001, J. Quant. Spectrosc. Radiat. Transf., 82(1-4), 5–44, doi:10.1016/S0022-4073(03)00146-8.
- Rothman, L. S. et al. (2005), The HITRAN 2004 molecular spectroscopic database, J. Quant. Spectrosc. Radiat. Transf., 96(2), 139–204, doi:10.1016/j.jqsrt.2004.10.008.
- Rothman, L. S. et al. (2009), The HITRAN 2008 molecular spectroscopic database, J. Quant. Spectrosc. Radiat. Transf., 110(9-10), 533–572, doi:10.1016/j.jqsrt.2009.02.013.
- Rothman, L. S. et al. (2013), The HITRAN2012 molecular spectroscopic database, J. Quant. Spectrosc. Radiat. Transf., 130, 4–50, doi:10.1016/j.jqsrt.2013.07.002.
- Rudolph, J. (1995), The tropospheric distribution and budget of ethane, J. Geophys. Res., 100(D6), 11369, doi:10.1029/95JD00693.
- Sanderson, M. G. (1996), Biomass of termites and their emissions of methane and carbon dioxide: A global database, Global Biogeochem. Cycles, 10(4), 543–557, doi:10.1029/96GB01893.
- Schade, G. W., and A. H. Goldstein (2001), Fluxes of oxygenated volatile organic compounds from a ponderosa pine plantation, J. Geophys. Res. Atmos., 106(D3), 3111–3123, doi:10.1029/2000JD900592.
- Schade, G. W., and A. H. Goldstein (2006), Seasonal measurements of acetone and methanol: Abundances and implications for atmospheric budgets, Global Biogeochem. Cycles, 20(1), GB1011, doi:10.1029/2005GB002566.
- Schmidt, U., D. H. Ehhalt, U. Schmidt, R. Zander, P. Demoulin, and C. P. Rinsland (1991), Seasonal cycle and secular trend of the total and tropospheric column abundance of ethane above the Jungfraujoch, J. Geophys. Res., 96(D3), 4985, doi:10.1029/90JD02229.
- Schneider, U., T. Fuchs, A. Meyer-Christoffer, and B. Rudolf (2008), Global precipitation analysis products of the GPCC, Offenbach am Main, Germany.
- Schneising, O., J. P. Burrows, R. R. Dickerson, M. Buchwitz, M. Reuter, and H. Bovensmann (2014), Remote sensing of fugitive methane emissions from oil and gas production in North American tight geologic formations: Remote sensing of fugitive methane emissions from oil and gas production, Earth's Futur., doi:10.1002/2014EF000265.

- Sepúlveda, E., M. Schneider, F. Hase, O. E. García, a. Gomez-Pelaez, S. Dohe, T. Blumenstock, and J. C. Guerra (2012), Long-term validation of tropospheric column-averaged CH4 mole fractions obtained by mid-infrared ground-based FTIR spectrometry, Atmos. Meas. Tech., 5(6), 1425–1441, doi:10.5194/amt-5-1425-2012.
- Shine, K. P., R. G. Derwent, D. J. Wuebbles, and J.-J. Morcrette (1990), Chapter 2. Radiative forcing of climate. Contribution of Working Group I to the First Assessment Report of the Intergovernmental Panel on Climate Change, IPCC, 28.
- Simpson, I. J., F. S. Rowland, S. Meinardi, and D. R. Blake (2006), Influence of biomass burning during recent fluctuations in the slow growth of global tropospheric methane, Geophys. Res. Lett., 33(22), doi:10.1029/2006GL027330.
- Simpson, I. J., M. P. Sulbaek Andersen, S. Meinardi, L. Bruhwiler, N. J. Blake, D. Helmig, F. S. Rowland, and D. R. Blake (2012), Long-term decline of global atmospheric ethane concentrations and implications for methane., Nature, 488(7412), 490–4, doi:10.1038/nature11342.
- Singh, H. B., and P. L. Hanst (1981), Peroxyacetyl nitrate (PAN) in the unpolluted atmosphere: An important reservoir for nitrogen oxides, Geophys. Res. Lett., 8(8), 941–944, doi:10.1029/GL008i008p00941.
- Singh, H. B., D. O'Hara, D. Herlth, W. Sachse, D. R. Blake, J. D. Bradshaw, M. Kanakidou, and P. J. Crutzen (1994), Acetone in the atmosphere: Distribution, sources, and sinks, J. Geophys. Res. Atmos., 99(D1), 1805–1819, doi:10.1029/93JD00764.
- Singh, H. B., W. H. Brune, J. H. Crawford, D. J. Jacob, and P. B. Russell (2006), Overview of the summer 2004 Intercontinental Chemical Transport Experiment–North America (INTEX-A), J. Geophys. Res. Atmos., 111(D24), D24S01, doi:10.1029/2006JD007905.
- Singh, H., Y. Chen, A. Staudt, D. Jacob, D. Blake, B. Heikes, and J. Snow (2001), Evidence from the Pacific troposphere for large global sources of oxygenated organic compounds, Nature, 410(6832), 1078–1081, doi:10.1038/35074067.
- Solomon, S., K. H. Rosenlof, R. W. Portmann, J. S. Daniel, S. M. Davis, T. J. Sanford, and G.-K. Plattner (2010), Contributions of Stratospheric Water Vapor to Decadal Changes in the Rate of Global Warming, Science, 327(5970), 1219–1223, doi:10.1126/science.1182488.
- Spahni, R. et al. (2011), Constraining global methane emissions and uptake by ecosystems, Biogeosciences, 8(6), 1643–1665, doi:10.5194/bg-8-1643-2011.
- Stavrakou, T. et al. (2011), First space-based derivation of the global atmospheric methanol emission fluxes, Atmos. Chem. Phys., 11(10), 4873–4898, doi:10.5194/acp-11-4873-2011.
- Stocker, T. F., D. Qin, G.-K. Plattner, M. Tignor, S. K. Allen, J. Boschung, A. Nauels, Y. Xia, V. Bex, and P. M. Midgley (2013), The Physical Science Basis. Contribution of Working Group I to the Fifth Assessment Report of the Intergovernmental Panel on Climate Change, Cambridge, United Kingdom and New York, NY, USA.
- Stolarski, R. S., and R. J. Cicerone (1974), Stratospheric chlorine: a possible sink for ozone, Can. J. Chem., 52(8), 1610–1615, doi:10.1139/v74-233.
- Strahan, S. E., L. D. Oman, A. R. Douglass, and L. Coy (2015), Modulation of Antarctic vortex composition by the quasi-biennial oscillation, Geophys. Res. Lett., 42(10), 4216–4223, doi:10.1002/2015GL063759.

- Sudo, K. (2002), CHASER: A global chemical model of the troposphere 1. Model description, J. Geophys. Res., 107(D17), doi:10.1029/2001JD001113.
- Sudo, K., and H. Akimoto (2007), Global source attribution of tropospheric ozone: Long-range transport from various source regions, J. Geophys. Res., 112(D12), doi:10.1029/2006JD007992.
- Suntharalingam, P. (2004), Improved quantification of Chinese carbon fluxes using CO 2 /CO correlations in Asian outflow, J. Geophys. Res., 109(D18), D18S18, doi:10.1029/2003JD004362.
- Sussmann, R., and K. Schäfer (1997), Infrared spectroscopy of tropospheric trace gases: combined analysis of horizontal and vertical column abundances, Appl. Opt., 36(3), 735, doi:10.1364/AO.36.000735.
- Sussmann, R., F. Forster, M. Rettinger, and N. Jones (2011), Strategy for high-accuracy-and-precision retrieval of atmospheric methane from the mid-infrared FTIR network, Atmos. Meas. Tech., 4(9), 1943–1964, doi:10.5194/amt-4-1943-2011.
- Sussmann, R., F. Forster, M. Rettinger, and P. Bousquet (2012), Renewed methane increase for five years (2007–2011) observed by solar FTIR spectrometry, Atmos. Chem. Phys., 12(11), 4885–4891, doi:10.5194/acp-12-4885-2012.
- Sussmann, R., T. Borsdorff, and F. Karlsruhe (2007), Technical Note: Interference errors in infrared remote sounding of the atmosphere, 3537–3557.
- Sussmann, R., T. Borsdorff, M. Rettinger, C. Camy-Peyret, P. Demoulin, P. Duchatelet, E. Mahieu, and C. Servais (2009), Technical Note: Harmonized retrieval of column-integrated atmospheric water vapor from the FTIR network first examples for long-term records and station trends, Atmos. Chem. Phys., 9(22), 8987–8999, doi:10.5194/acp-9-8987-2009.
- Swanson, A. L. (2003), Seasonal variations of C_2–C_4 non-methane hydrocarbons and C_1–C_4 alkyl nitrates at the Summit research station in Greenland, J. Geophys. Res., 108(D2), doi:10.1029/2001JD001445.
- Takemura, T. (2005), Simulation of climate response to aerosol direct and indirect effects with aerosol transport-radiation model, J. Geophys. Res., 110(D2), doi:10.1029/2004JD005029.
- Tie, X., A. Guenther, and E. Holland (2003), Biogenic methanol and its impacts on tropospheric oxidants, Geophys. Res. Lett., 30(17), 1881, doi:10.1029/2003GL017167.
- Tikhonov, A. (1963), On the solution of incorrectly stated problems and a method of regularization, Dokl. Acad. Nauk SSSR, 151, 501–504.
- Toon, G. C. (1991), The JPL MkIV interferometer, Opt. Photonics News, 2(10), 19, doi:10.1364/OPN.2.10.000019.
- Turner, A. J., D. J. Jacob, K. J. Wecht, J. D. Maasakkers, E. Lundgren, A. E. Andrews, S. C. Biraud, H. Boesch, K. W. Bowman, N. M. Deutscher, M. K. Dubey, D. W. T. Griffith, F. Hase, A. Kuze, J. Notholt, H. Ohyama, R. Parker, V. H. Payne, R. Sussmann, C. Sweeney, V. A. Velazco, T. Warneke, P. O. Wennberg, D. Wunch (2015), Estimating global and North American methane emissions with high spatial resolution using GOSAT satellite data, Atmos. Chem. Phys., 15(12), 7049–7069, doi:10.5194/acp-15-7049-2015.
- Turner, J., S. R. Colwell, G. J. Marshall, T. A. Lachlan-Cope, A. M. Carleton, P. D. Jones, V. Lagun, P. A. Reid, and S. Iagovkina (2004), The SCAR READER Project: Toward a High-Quality Database of Mean Antarctic Meteorological Observations, J. Clim., 17(14), 2890–2898, doi:10.1175/1520-0442(2004)017<2890:TSRPTA>2.0.CO;2.

- Tyndall, G. S., R. A. Cox, C. Granier, R. Lesclaux, G. K. Moortgat, M. J. Pilling, A. R. Ravishankara, and T. J. Wallington (2001), Atmospheric chemistry of small organic peroxy radicals, J. Geophys. Res. Atmos., 106(D11), 12157–12182, doi:10.1029/2000JD900746.
- United Nations (2011), The Cancun Agreements: Outcome of the work of the Ad Hoc Working Group on Long-term Cooperative Action under the Convention, in Conference of the Parties on its sixteenth session (COP 16), edited by Framework Convention on Climate Change, p. 31, United Nations, Cancun, Mexico.
- van der Werf, G. R., J. T. Randerson, L. Giglio, G. J. Collatz, M. Mu, P. S. Kasibhatla, D. C. Morton, R. S. DeFries, Y. Jin, and T. T. van Leeuwen (2010), Global fire emissions and the contribution of deforestation, savanna, forest, agricultural, and peat fires (1997–2009), Atmos. Chem. Phys., 10(23), 11707–11735, doi:10.5194/acp-10-11707-2010.
- van Donkelaar, A., R. V. Martin, A. N. Pasch, J. J. Szykman, L. Zhang, Y. X. Wang, and D. Chen (2012), Improving the Accuracy of Daily Satellite-Derived Ground-Level Fine Aerosol Concentration Estimates for North America, Environ. Sci. Technol., 46(21), 11971–11978, doi:10.1021/es3025319.
- van Donkelaar, A., R. V. Martin, R. J. D. Spurr, E. Drury, L. A. Remer, R. C. Levy, and J. Wang (2013), Optimal estimation for global ground-level fine particulate matter concentrations, J. Geophys. Res. Atmos., 118(11), 5621–5636, doi:10.1002/jgrd.50479.
- van het Bolscher, M., J. Pereira, A. Spessa, S. Dalsoren, T. van Nojie, and S. Szopa (2008), REanalysis of the TROpospheric chemical composition over the past 40 years, A long-term global modeling study of tropospheric chemistry funded under the 5th EU framework programme, Hamburg, Germany.
- Viatte, C., K. Strong, K. A. Walker, and J. R. Drummond (2014), Five years of CO, HCN, C_2H_6, C_2H_2, CH_3OH, HCOOH and H_2CO total columns measured in the Canadian high Arctic, Atmos. Meas. Tech., 7(6), 1547–1570, doi:10.5194/amt-7-1547-2014.
- Vigouroux, C. et al. (2009), Ground-based FTIR and MAX-DOAS observations of formaldehyde at Réunion Island and comparisons with satellite and model data, Atmos. Chem. Phys., 9(24), 9523–9544, doi:10.5194/acp-9-9523-2009.
- Vigouroux, C. et al. (2012), FTIR time-series of biomass burning products (HCN, C_2H_6, C_2H_2, CH_3OH, and HCOOH) at Reunion Island (21 °S, 55 °E) and comparisons with model data, Atmos. Chem. Phys., 12(21), 10367–10385, doi:10.5194/acp-12-10367-2012.
- Vinciguerra, T., S. Yao, J. Dadzie, A. Chittams, T. Deskins, S. Ehrman, and R. R. Dickerson (2015), Regional air quality impacts of hydraulic fracturing and shale natural gas activity: Evidence from ambient VOC observations, Atmos. Environ., 110, 144–150, doi:10.1016/j.atmosenv.2015.03.056.
- von Kuhlmann, R., M. G. Lawrence, P. J. Crutzen, and P. J. Rasch (2003), A model for studies of tropospheric ozone and nonmethane hydrocarbons: Model evaluation of ozone-related species, J. Geophys. Res. Atmos., 108(D23), 4729, doi:10.1029/2002JD003348.
- Wallace, J. M., and P. V. Hobbs (2006), Atmospheric Science: An introductory survey, Elsevier -., edited by R. Dmowska, D. Hartmann, and Rossby T., Amsterdam Boston : Elsevier Academic Press, Amsterdam Boston.
- Walter, B. P., M. Heimann, and E. Matthews (2001), Modeling modern methane emissions from natural wetlands: 1. Model description and results, J. Geophys. Res., 106(D24), 34189, doi:10.1029/2001JD900165.

- Wang, J. S., J. a. Logan, M. B. McElroy, B. N. Duncan, I. a. Megretskaia, and R. M. Yantosca (2004), A 3-D model analysis of the slowdown and interannual variability in the methane growth rate from 1988 to 1997, Global Biogeochem. Cycles, 18(3), doi:10.1029/2003GB002180.
- Wang, Y. X. (2004), A nested grid formulation for chemical transport over Asia: Applications to CO, J. Geophys. Res., 109(D22), D22307, doi:10.1029/2004JD005237.
- Warneke, C., T. Karl, H. Judmaier, A. Hansel, A. Jordan, W. Lindinger, and P. J. Crutzen (1999), Acetone, methanol, and other partially oxidized volatile organic emissions from dead plant matter by abiological processes: Significance for atmospheric HO x chemistry, Global Biogeochem. Cycles, 13(1), 9–17, doi:10.1029/98GB02428.
- Watanabe, S. et al. (2011), MIROC-ESM 2010: model description and basic results of CMIP5-20c3m experiments, Geosci. Model Dev., 4(4), 845–872, doi:10.5194/gmd-4-845-2011.
- Wecht, K. J., D. J. Jacob, M. P. Sulprizio, G. W. Santoni, S. C. Wofsy, R. Parker, H. Bösch, and J. Worden (2014), Spatially resolving methane emissions in California: constraints from the CalNex aircraft campaign and from present (GOSAT, TES) and future (TROPOMI, geostationary) satellite observations, Atmos. Chem. Phys. Discuss., 14(3), 4119–4148, doi:10.5194/acpd-14-4119-2014.
- Wells, K. C. et al. (2012), Tropospheric methanol observations from space: retrieval evaluation and constraints on the seasonality of biogenic emissions, Atmos. Chem. Phys., 12(13), 5897–5912, doi:10.5194/acp-12-5897-2012.
- Whaley, C. (2014), Improvements to our Understanding of Toronto-Area Atmospheric Composition, University of Toronto.
- Wiacek, A., J. R. Taylor, K. Strong, R. Saari, T. E. Kerzenmacher, N. B. Jones, and D. W. T. Griffith (2007), Ground-Based Solar Absorption FTIR Spectroscopy: Characterization of Retrievals and First Results from a Novel Optical Design Instrument at a New NDACC Complementary Station, J. Atmos. Ocean. Technol., 24(3), 432–448, doi:10.1175/JTECH1962.1.
- Wingenter, O. W., B. C. Sive, N. J. Blake, D. R. Blake, and F. S. Rowland (2005), Atomic chlorine concentrations derived from ethane and hydroxyl measurements over the equatorial Pacific Ocean: Implication for dimethyl sulfide and bromine monoxide, J. Geophys. Res., 110(D20), doi:10.1029/2005JD005875.
- Wofsy, S. C., M. B. McElroy, and Y. L. Yung (1975), The chemistry of atmospheric bromine, Geophys. Res. Lett., 2(6), 215–218, doi:10.1029/GL002i006p00215.
- World Meteorological Organization (1985), Atmospheric Ozone 1985: Assessment of our understanding of the processes Controlling Its Present Distribution and Change, in Global Ozone Research and Monitoring Project Report, edited by R. T. et al. Watson, Geneva, Switzerland.
- World Meteorological Organization (2014a) Scientific Assessment of Ozone Depletion: 2014, World Meteorological Organization, Global Ozone Research and Monitoring Project—Report No. 55, 416 pp., Geneva, Switzerland.
- World Meteorological Organization (2014b), Greenhouse Gas Bulletin N°10, Geneva, Switzerland.
- Xiao, Y., J. A. Logan, D. J. Jacob, R. C. Hudman, R. Yantosca, and D. R. Blake (2008), Global budget of ethane and regional constraints on U.S. sources, J. Geophys. Res., 113(D21), doi:10.1029/2007JD009415.

- Xu, L.-H., R. M. Lees, P. Wang, L. R. Brown, I. Kleiner, and J. W. C. Johns (2004), New assignments, line intensities, and HITRAN database for CH3OH at 10μm, J. Mol. Spectrosc., 228(2), 453–470, doi:10.1016/j.jms.2004.05.017.
- Yevich, R., and J. A. Logan (2003), An assessment of biofuel use and burning of agricultural waste in the developing world, Global Biogeochem. Cycles, 17(4), doi:10.1029/2002GB001952.
- Zander, R. (1975), Presence of hydrogen fluoride in the upper stratosphere, Comptes rendus des séances l'Académie des Sci. Série B Sci. Phys., 12, 213.
- Zander, R., E. Mahieu, P. Demoulin, P. Duchatelet, G. Roland, C. Servais, M. De Mazière, S. Reimann, and Zander, R., P. Demoulin, D. H. Ehhalt, and U. Schmidt (1989), Secular increase of the vertical column abundance of methane derived from IR solar spectra recorded at the Jungfraujoch station, J. Geophys. Res., 94(D8), 11029, doi:10.1029/JD094iD08p11029.
- Zellweger, C., J. Forrer, P. Hofer, S. Nyeki, B. Schwarzenbach, E. Weingartner, M. Ammann, and U. Baltensperger (2003), Partitioning of reactive nitrogen (NOy) and dependence on meteorological conditions in the lower free troposphere, Atmos. Chem. Phys., 3(3), 779–796, doi:10.5194/acp-3-779-2003.
- Zeng, G., S. W. Wood, O. Morgenstern, N. B. Jones, J. Robinson, and D. Smale (2012), Trends and variations in CO, C2H6, and HCN in the Southern Hemisphere point to the declining anthropogenic emissions of CO and C2H6, Atmos. Chem. Phys., 12(16), 7543–7555, doi:10.5194/acp-12-7543-2012.
- Zhang, L., D. J. Jacob, E. M. Knipping, N. Kumar, J. W. Munger, C. C. Carouge, A. van Donkelaar, Y. X. Wang, and D. Chen (2012), Nitrogen deposition to the United States: distribution, sources, and processes, Atmos. Chem. Phys., 12(10), 4539–4554, doi:10.5194/acp-12-4539-2012.
- Zhang, L., D. J. Jacob, N. V. Downey, D. A. Wood, D. Blewitt, C. C. Carouge, A. van Donkelaar, D. B. A. Jones, L. T. Murray, and Y. Wang (2011), Improved estimate of the policy-relevant background ozone in the United States using the GEOS-Chem global model with 1/2° × 2/3° horizontal resolution over North America, Atmos. Environ., 45(37), 6769–6776, doi:10.1016/j.atmosenv.2011.07.054.
- Zhao, Y. (2002), Spectroscopic measurements of tropospheric CO, C2H6, C2H2, and HCN in northern Japan, J. Geophys. Res., 107(D18), doi:10.1029/2001JD000748.

Internet references

- Annan, K. (2003), The Montreal Protocol, ozone hole.
  Available from: http://www.theozonehole.com/montreal.htm
  (Accessed 28 October 2015)
- United Nations Framework Convention on Climate Change, UNFCC (1997), Article 2,
  Available from:
  http://unfccc.int/essential_background/convention/status_of_ratification/items/2631.php
  (Accessed 28 October 2015)
- Grindelwald Tourismus (2015), The Jungfraujoch - "Top of Europe," Alpensicht. Available from: http://www.alpensicht.com/English/Switzerland-Hotspots/switzerland_hot_spots_jungfraujoch.htm
  (Accessed 24 October 2015)
- NOAA/ESRL (2015), NCEP reanalysis, NOAA/ESRL/PSD.
  Available from:
  http://www.esrl.noaa.gov/psd/thredds/catalog/Datasets/ncep.reanalysis.derived/tropopause/catalog.html (Accessed 13 March 2015)
- NASA Astrobiology Institute's Virtual Planetary Laboratory (2015), Carbon dioxide, Mol. database. Available from: http://vpl.astro.washington.edu/spectra/co2.htm
  (Accessed 20 October 2015)
- Toon, G. C., B. Sen, and A. Kleinboehl (2015), Derivation of pseudo-lines from laboratory cross-sections, JPL
  Available from: http://mark4sun.jpl.nasa.gov/data/spec/Pseudo/Readme
  (Accessed 14 October 2015)
- UC Davis ChemWiki (2015), Selection rules and transition moment integral,
  Available from:
  http://chemwiki.ucdavis.edu/Physical_Chemistry/Spectroscopy/Fundamentals/Selection_rules_and_transition_moment_integral
  (Accessed 26 October 2015)

Appendix A – List of molecules

Formula	Molecule name	Formula	Molecule name
Ar	Argon	C_2H_5OOH	Ethyl hydroperoxide
BrO_x	Bromine oxides	CH_3OOH	Methyl hydroperoxyde
CCl_2F_2	CFC−12	CO	Carbon monoxide
CCl_3F	CFC−11	CO_2	Carbon dioxide
C_5H_8	Isoprene	HF	Hydrochloric acid
C_4H_{10}	Butane	HCl	Hydrofluoric acid
C_3H_8	Propane	HDO	Heavy water
C_3H_6	Propene	HgCdTe	Mercury−Cadmium−Tellurium (MCT)
C_2H_6	Ethane	H_2O_2	Hydrogen peroxide
C_2H_5	Ethyl radical	H_2O	Water vapour
C_2H_4	Ethylene	HO_X	Hydrogen oxide radicals
CH_3	Methyl radical	HO_2	Hydroxyl radicals
CH_4	Methane	InSb	Indium−Antimonide
$CHClF_2$	HCFC−22	KBr	Potassium bromide
CHF_3	HFC−23	N_2	Nitrogen
CH_3Cl	Methyl chloride	N_2O	Nitrous oxide
CH_3CHO	Acetaldehyde	NO_x	Nitrogen oxides
CH_3COO_2	Peroxyacetyl radical	NO_2	Nitrogen dioxide
$CH_3C(O)O$	Acetate	NO	Nitrogen monoxide
$CHCOO_2NO_2$	PAN	O_3	Ozone
C_3H_6O	Acetone	$O_3(668)$ $O_3(686)$ $O_3(676)$ $O_3(667)$	Ozone isotopologues
$C_2H_5O_2$	Ethylperoxy radical	O_2	Oxygen
CH_3O_2	Methylperoxy radical	O_x	Oxides
CH_4O	Methanol	HO	Hydroxyl radical
CH_2O	Formaldehyde	PbS	Lead−Sulphide
CH_3OH	Methanol	PbS	Sulphur hexafluoride
CH_2OH	Hydroxymethyl radical		

Appendix B – List of acronyms

ABL – Atmospheric Boundary Layer
ACE – Atmospheric Chemistry Experiment
ACE-FTS – Atmospheric Chemistry Experiment–Fourier Transform Spectrometer
AGAGE – Advanced Global Atmospheric Gases Experiment
AGCM – Atmospheric Global Circulation Model
ATLAS – Atmospheric Laboratory for Applications and Science
ATMOS – Atmospheric Trace Molecule Spectroscopy
CFC – Chlorofluorocarbons
CHASER – Chemical AGCM for Study of atmospheric Environment and Radiative forcing
CICERO – Center for International Climate and Environmental Research Oslo
CMDL – Climate Monitoring and Diagnostics Laboratory
CTM – Chemical Transport Model
DOFS – Degree of Freedom for Signal
DPGS – Double–Pass Grating Spectrometer
EAP – Effective Apodisation Parameter
ECMWF – European Centre for Medium–Range Weather Forecasts
EDGAR – Emission Database for Global Atmospheric Research
EMEP – European Monitoring and Evaluation Programme
ENVISAT – European ENVIronmental SATellite
FTIR – Fourier Transform InfraRed spectrometer
FTS – Fourier Transform Spectrometer
GAW – Global Atmosphere Watch
GC – Gas Chromatography
GCM – Global Circulation Model
GEOS – Goddard Earth Observing System
GIRPAS – Groupe Infrarouge de l'Atmosphère Physique et Solaire
GMAO – Global Modeling Assimilation Office
GOSAT – Greenhouse Gases Observing Satellite
GWP – Global Warming Potential
HALOE – Halogen Occultation Experiment
HCFC – Hydrochlorofluorocarbon
HFC – Hydrofluorocarbons
HIRS – High-Resolution Infrared Sounder
HITRAN – HIgh-resolution TRANsmission molecular absorption database
IASI – Infrared Atmospheric Sounding Interferometer
ILC – Inter-Layer Correlation
IMAGES – Intermediate Model of the Annual and Global Evolution of Species
IPCC – International Panel for Climate Change
IR – InfraRed
IRWG – Infrared Working Group

ISSJ – International Scientific Station of the Jungfraujoch
ITCZ – InterTropical Convergence Zone
JAMSTEC – Japan Agency for Marine–Earth Science and Technology
JAXA – Japan Aerospace Exploration Agency
LT – Lower Tropospheric Layer
MACC – Monitoring Atmospheric Composition & Change
MCT – Mercury-Cadmium-Tellurium
MIPAS – Michelson Interferometer for Passive Atmospheric Sounding
MIROC-ESM – Model for Interdisciplinary Research on Climate-Earth System Model
MkIV interferometer – MkIV Fourier Transform Infrared
MLS – Microwave Limb Sounder
MOZART – Model for Ozone and Related Tracers
MS – Mass Spectrometry
MSU – Microwave Sounding Unit
MW – Micro-Window
NCAR – National Center for Atmospheric Research
NCEP – National Centers for Environmental Prediction
NDACC – Network for Detection of Atmospheric Composition Change
NDSC – Network for the Detection of Stratospheric Change
NIES – National Institute for Environmental Studies
NMV – Normal Modes of Vibration
NMVOC – Non-Methane Volatile Organic Compound
NOAA – National Oceanic and Atmospheric Administration
OEM – Optimal Estimation Method
OPD – Optical Path Difference
PAN – Peroxyacetyl Nitrate
PEM – Pacific Exploratory Mission
PNNL – Pacific North West National Laboratory
RETRO – REanalysis of the TROpospheric chemical composition
RF – Radiative Forcing
RMS – Root Mean Square
SL-3 – Spacelab 3
SNR – Signal-to-Noise Ratio
SPRINTARS – Spectral Radiation-Transport Model for Aerosol Species
SSU – Stratospheric Sounding Unit
STE – Stratospheric-Tropospheric Exchange
SZA – Solar Zenith Angle
TES – Tropospheric Emission Spectrometer
TIME – Thermosphere Ionosphere Mesosphere Electrodynamics
TIROS – Television Infrared Observation Satellite
TIVOS – Television Operational Vertical Sounder
UARS – Upper Atmosphere Research Satellite

UPAR − UARS Reference Atmosphere Project
UTLS – Upper Troposphere-Lower Stratosphere
VISIT − Vegetation Integrative SImulator for Trace
VOC − Volatile Organic Compounds
WACCM − Whole Atmosphere Community Climate Model
WMO − World Meteorological Organization
ZPD − Zero optical Path Difference